An Imaging Fourier Transform Spectrometer (IFTS) for Climate Observations

GURPREET SINGH

A THESIS SUBMITTED TO THE FACULTY OF GRADUATE STUDIES

IN PARTIAL FULFILLMENT OF THE REQUIREMENTS FOR THE

DEGREE OF

MASTER OF SCIENCE

GRADUATE PROGRAM IN EARTH AND SPACE SCIENCE

YORK UNIVERSITY

TORONTO, ONTARIO,

NOVEMBER 2018

ABSTRACT

Climate change is an ongoing global phenomenon having a greater impact at higher latitudes. The instrument development reported herein is aimed at demonstrating the feasibility of using an Imaging Fourier Transform Spectrometer (IFTS) to measure carbon dioxide (CO_2), and methane (CH_4) mixing ratios at high latitudes using oxygen A-band measurements as a surface pressure reference. It is proposed that this be done by measuring the near-infrared spectrum of backscattered sunlight from a satellite platform. The goal is to have continuous measurements of the evolution of these gases from the permafrost over the arctic summer. An open breadboard IFTS with two channels centred at 762 nm for O_2A band and 1600 nm for CO_2 and CH_4 has been designed and constructed. Each channel has a separate detector which has a focal array that consists of 320x256 pixels. The active area of the detector would give a large field of view and provides a high spatial resolution from orbital altitudes. Both detectors are thermo-electrically cooled with InGaAs wafers and are read out through a USB 2.0 interface to transfer images into the data collection computer's memory. The core of the instrument is a commercial-off-the-shelf (COTS) component which is a modified Michelson interferometer. This feature of the project links the scientific and commercial research communities and works towards the goal of "easily accessible space". N-BK7 focusing lenses are used for maximum transmission in the visible and NIR region. A simple three-layer control architecture is adopted where commands are sent by the user to a microcontroller which coordinates the operation of the interferometer and data collection and images are saved in the non-volatile disk memory of the data storage computers.

This thesis details the optical design, instrumental setup, and development criteria for the IFTS. Progress in the development of a software package to control and acquire data is also discussed. The instrument is being developed to achieve the Technology Readiness Level 4 standard which covers the breadboard validation of a space system in a laboratory environment. Hardware specifications and software algorithms of the instrument are presented. Results from an external Helium-Neon (HeNe) laser and a broadband light source limited by spectral bandpass filters are presented. Finally, recommendations and future improvements to this research and development program are listed.

This research project will support efforts by Environment and Climate Change Canada, the Canadian Space Agency, and ABB Inc. in developing a satellite implementation of the technology.

ACKNOWLEDGEMENTS

I would like to thank Professor Tom McElroy for allowing me to work on this project under his supervision. His guidance and direction provided me with unparalleled support to reach the goal of my Masters in the most fun and exciting way. I am grateful to my committee members, Dr. Christopher McLinden and Professor Anantharaman Kumarakrishnan to help me identify the directions of my work and keeping me on track. I would also like to extend my gratitude to David Barton for helping me to understand the complexities of hands-on work and developing electronics and software for flight-ready instruments. I appreciate the collaboration with Greg Blair in the development of the software to control the cameras and to develop the database format. I am grateful to Dr. Rehan Siddiqui and Zahra Vaziri for their on-going support throughout the span of the project. I am also thankful to our colleagues at ABB Inc. in providing me with the benefit of their experience and knowledge. Finally, I am obliged to my family and friends who kept me inspired and motivated.

This work is funded by the Laboratory for Atmospheric Remote Sounding from Space (LARSS) at York University (LARSS). LARSS was supported by York University, the Natural Sciences and Engineering Research Council of Canada (NSERC), the Canadian Foundation for Innovation (CFI), Environment and Climate Change Canada, ABB Inc. and the Canadian Space Agency (CSA).

Table of Contents

LIST OF TABLES

LIST OF FIGURES

LIST OF ACRONYMS

ABB	ASEA Brown Boveri (Inc.)
ACE-FTS	Atmospheric Chemistry Experiment – Fourier Transform Spectrometer
ACU	ABB control unit
IPCC - AR5	Intergovernmental Panel on Climate Change - Fifth assessment report
AW	Acquisition window
BCE	Before Common Era
CAM1600	Camera connected to CH_4 and CO_2 channel
CAM1600PC	The computer connected to CH_4, and CO_2 channel.
CAM762	Camera connected to O_2 channel
CAM762PC	The computer connected to O_2 channel
CAS	Control and Acquisition Software
CE	Common Era
COTS	Commercial-Off-The-Shelf
CPC	Control PC
CSA	Canadian Space Agency
DFB	Distributed Feedback
FFT	Fast Fourier transform
FPGA	Field Programmable Gate Array
FR	Digital Fringe signal from ABB control unit
FR90	Digital DePhase signal from ABB control unit
FRA	Fringe Analog
FTS	Fourier Transform Spectrometer
GHG	Greenhouse gas
GWP	Global Warming Potential
HeNe	Helium-Neon
MCT	Mercury Cadmium Telluride (HgCdTe)
IDF	Instrument Data File
IDFS	Instrument Data File Set
IFTS	Imaging Fourier Transform Spectrometer

ILS	Instrument Line Shape
IRIS	Infrared Radiation Interferometer Spectrometer
InGaAs	Indium Gallium Arsenide
IPCC	Intergovernmental Panel on Climate Change
IR	Infrared
LARSS	Laboratory for Atmospheric Remote Sounding from Space
MPD	Maximum Path Difference
OPD	Optical Path Difference
SD	Scan Direction signal from ABB control unit
SWIR	Shortwave Infrared
SNR	Signal to Noise Ratio
SRS	Software Requirements Specification
SW	Sampling Window signal from ABB control unit
TA	Turn Around signal from ABB control unit
TANSO-FTS	Thermal and Near Infrared Sensor – Fourier Transform Spectrometer
TIR	Thermal Infrared
TEC	Thermo-electric cooled
TRL	Technology Readiness Level
TT&C	Telemetry, tracking, and command
Vis	Visible
ZPD	Zero-path-difference signal from ABB control box.

LIST OF SYMBOLS

C	number of particles per unit volume [m^{-3}]
l	absorption path length [m]
σ ($\tilde{\nu}$)	absorption cross-section [m^2]
$\tilde{\nu}_0$	line centre at zero pressure [cm^{-1}]
δ_L	line position shift parameter
$\Delta\tilde{\nu}_L$	line width parameter [cm^{-1}]
T	Temperature [K]
T_0	reference temperature = 296 K
p	pressure [Pa]
p_0	reference pressure = 1 atm
p_s	the partial pressure of the gas which absorbs the radiation at wavenumber $\tilde{\nu}$ [Pa]
m	mass of molecule [atomic mass unit]
c	the speed of light in vacuum [m s^{-1}]
$\tilde{\nu}$	observed resonance wavenumber of the molecule [cm^{-1}]
$\tilde{\nu}_0$	resonance wavenumber of the molecule at rest [cm^{-1}]
X_o	OPD [cm]
σ_0	wave number [cm^{-1}]
$S_0(\sigma_0)$	interferogram
$\Delta\nu$	frequency resolution [s^{-1}]
Δt	time difference between first and last wavefront interacting with the interferometer during a single scan [s]
f	focal length [m]
r	the radial distance of an off-axis pixel from the centre pixel [m]
(x_d, y_d)	coordinates of position of the centre of the pixel
θ	off-axis angle
ppmv	parts per million by volume
ppm	parts per million
ppb	parts per billion
ppbv	parts per billion by volume

CHAPTER 1

1.0. INTRODUCTION

The fifth assessment report (AR5) of the Intergovernmental Panel on Climate Change (IPCC) states that the warming of the zonal mean surface temperature at higher latitudes exceeds the global average temperature change [1]. This poses a great problem, as it leads to a positive feedback loop in which the melting of Arctic permafrost, which acts as an envelope to trap greenhouse gases such as carbon dioxide (CO_2) and methane (CH_4), leads to further warming and greenhouse gas release [2] [3]. An observing method is needed to document the evolution of greenhouse gases from the permafrost to quantify the impact the melting will have on the global climate system.

Interferometers are widely used in many scientific laboratories to measure the concentrations of constituents in a given sample. The performance of these instruments is highly dependent on environmental effects [4] [5]. Thus, the use of such instruments to measure atmospheric concentration is complicated and challenging [4] [6]. The Laboratory for Atmospheric Remote Sounding from Space (LARSS) at York University is developing an Imaging Fourier Transform Spectrometer (IFTS) for climate observations by atmospheric remote sounding. The York IFTS is designed to demonstrate the possibility of making high-spatial-resolution measurements of CO_2 and CH_4 over the Arctic. The goal of this project is to develop an IFTS system which can measure backscattered radiation in a laboratory environment and develop design elements that will make it operable in the space environment. The current work has achieved Technology Readiness Levels 4 (TRL4), breadboard validation of the space system in the laboratory

environment [7]. The flight version of the IFTS will be a nadir-viewing instrument that will make measurements in two spectral bands. One is at 1.6 μm for measuring CO_2 and CH_4. This channel has a spectral range of 5990 cm^{-1} to 6450 cm^{-1}. The second spectral band is at 762 nm for measuring the O_2 A-band with a spectral range of 13060 cm^{-1} to 13168 cm^{-1}. Both channels will make observations with a 0.50 cm^{-1} spectral sampling FWHM.

A commercial-off-the-shelf (COTS) modulator purchased from ABB Inc. of Quebec City is the core of the instrument [8]. It is a modified Michelson interferometer which uses a voice coil motor drive together with a flexure pivot to convert linear to rotary motion. An optical path difference (OPD) of 2 cm is achieved by splitting and reflecting roughly equal portions of the input beam from 50 mm corner cubes secured to the moving element of the modulator. A metrology laser with known wavelength, injected into the instrument provides precise knowledge of the optical path difference and is used to determine and control the scan speed of the mirror motion. An onboard white-light source is used to sense the zero-path difference (ZPD) of the scan. Two InGaAs imaging detectors are used to record interferograms. Various optical elements including focusing lenses, interference filters, and a dichroic beam splitter are incorporated in the instrument design. Acquisition software was developed to sample the data at a controlled rate and save it to disk memory. Transformation software is also developed to convert interferograms into spectra.

This thesis details the optical design, instrumental setup, and development criteria of the instrument along with some spectra acquired in the controlled laboratory environment. Progress in the development of a software package to control data acquisition is also discussed. This research project will support efforts by the federal Department of Environment and

Climate Change Canada, the Canadian Space Agency and ABB, Inc. in developing a satellite instrument for the proposed Aim-North space mission [9].

1.1. Measurements of CO_2 and CH_4 over the Arctic

The Arctic is typically defined to be north of 66^0N and is one of the most remote expanses on Earth. It is isolated from almost all major population centres and is one of the most poorly understood regions in the world with relatively few scientific measurements [10]. It includes parts of Canada, Alaska, Greenland, Iceland, Russia, and several European countries. It experiences amplified effects of global temperature change due to surface albedo change, changes in water vapour amount, possible changes in Arctic Ocean currents, and other effects. It is also important to monitor greenhouse gases (GHGs) in the atmosphere above the Arctic to understand and quantify their sources [11]. Satellites are a critical resource for monitoring and evaluating arctic climate changes since performing in situ measurements in harsh environments is costly [12]. Monitoring the entire Earth using multiple satellites to make measurements using remote sensing is also relatively easy, accurate, reliable, and consistent. There is an urgent need to develop scientific instruments that can be flown in space over the Arctic to provide atmospheric information to quantify these atmospheric issues.

1.2. Research motivation

This research is motivated by interesting challenges arising from designing and developing an imaging spectrometer for a payload. The nature of designing such a system involves careful inspection of intimate interactions of very many different factors including spectral range, spatial resolution, sensitivity requirements, detectors, an optical system, bandwidth, and other

components [13]. Due to various requirements such as computational capability, lock-and-stare mechanism, size and mass constraints, an FTS is considered the best system for an aircraft, whereas pushbroom grating, and filter wheel instruments are often considered better options for satellites, and planetary rovers respectively [13]. There is a need to establish the requirements and a solution to develop the best imaging instrument for arctic monitoring of GHGs. The proposed IFTS:

- has a high optical efficiency,
- has a high signal-to-noise ratio (SNR),
- works with large 2-D spatial images,
- has many spectral bins (high resolution),
- works over a wide range of wavelength regions,
- has temperature-controlled detectors,
- accepts entire input flux on all detector elements,
- has a controllable length of the scan,
- takes a series of contiguous snapshots, and
- is simple to operate.

The needs of experimentalists and what technology can offer always includes trade-offs. Comparing with the era of the Atmospheric Chemistry Experiment – Fourier Transform Spectrometer (ACE-FTS) (refer to section 2.8.1.1) which is the heritage instrument for York IFTS - computer technology has improved tremendously. This has allowed for a drastically increased data rate to accommodate data from imaging spectrometers. It is an excellent time to exploit

this technology to make higher performance instruments. The Michelson interferometer can be converted into an imaging spectrometer by simply adding an array of detectors at the focal plane. In the past few decades, a substantial improvement has been made in the performance of visible and IR detectors in both sensitivity and in the available number and small size of spatial elements. These technical improvements are one of the major reasons for an increased interest in imaging spectroscopy. This study can be considered a useful example of the development of criteria, requirements, and designs.

1.3. Research objectives

This section outlines the major objectives for this study. The final developed product is not an exact representation of a flight design but rather carries the same functional elements (modulator, optical filter, imaging detector, control system and processing and storage unit).

- The primary goal of the project is to develop a breadboard instrument which exist in a more "open" instrument architecture on which ideas for improvements can be tested easily and rapidly.
- To characterize the ABB modulator and to understand its components and operation.
- To demonstrate the readiness to measure CO_2 and CH_4.
- To simulate and develop the optical elements of the IFTS as per the scientific and technical requirements.
- To develop an architecture which defines the interfaces between hardware components which together constitute the entire system.
- To develop an operations algorithm around which the control and data acquisition is wrapped to illustrate the interactions of each subsystem amongst themselves.
- To analyze the system performance under various constraints such as different interference filters and imaging lenses that define channels and to optimize trade-offs.

- To sample input light sources with known features to produce interferograms and spectra to calibrate the instrument and allow an instrument physical model to be verified (This is important information for the development and optimization of a flight model IFTS).

1.4. Thesis layout

Chapter 1 establishes the motivation and goals of the research documented in this thesis.

Chapter 2 reviews the theoretical background of the project, describing atmospheric Greenhouse Gases (GHGs) and their impact on Earth's climate. In this chapter, the two most important GHGs after water vapour - carbon dioxide and methane - are discussed. It also describes their history and trends along with global cycles, which in turn, relates to their effects on climate change.. In addition, the importance of the constant and known mixing ratio of molecular oxygen in the atmosphere which allows remote sounding to retrieve information about atmospheric pressure and temperature is presented. It also covers the theoretical and mathematical framework for an interferometer and the challenges of implementing it as an "imaging" type spectrometer. In addition, it contains the heritage information regarding the use of interferometry in various fields. Design and development procedures for the Atmospheric Chemistry Experiment – Fourier Transform Spectrometer (ACE-FTS) and Thermal and Near Infrared Sensor – Fourier Transform Spectrometer (TANSO-FTS) payloads are detailed. The performance of an FTS is contrasted to that of dispersive and Fabry Perot spectrometers.

Chapter 3 contains the preliminary design and budgeting description for the York-IFTS. Instrument components including the modulator, focusing lens, detector, and electronics components are described. Major components in the structure of the modulator, such as the

actuator which produces the relative optical path difference between the two light beams in the interferometer, and the corner cubes are also discussed. An introduction of the experimental method and operations concept describing the interaction of various subsystems of the instrument are outlined. It discusses the path of the input light from the scene and its propagation through various optical elements. The operation of the metrology subsystem to produce accurate measurement sampling of the images collected, is also detailed. It covers the components and workings of control electronics. The ABB control unit (ACU) which houses electronic modules that provide power to the optomechanical assembly and signals to monitor the interferometer status is discussed. The input and output signals through the entire electronics pathway are also summarized and their role in controlling the acquisition of data is described.

Chapter 4 discusses the Control and Acquisition Software (CAS) which provides a framework to regulate the scan of the York IFTS instrument and to produce data products in a form suitable for analysis and archiving. The first half of the chapter is dedicated to giving a detailed description of the high-level requirements for the CAS. The IEEE guidelines listed in ISO/IEC/29148 [14] are closely followed to frame the requirements. The second half of the chapter provides several different architectural views of the aspects of the system. It also defines the performance constraints, the significance of functional requirements and their impacts, the coding layers, and performance issues. A structural model is outlined which describes the design in implementation terminology (e.g. computers, files, records), the software components, and hierarchy of control.

Chapter 5 is dedicated to the results of observation of monochromatic input light from a Helium-Neon laser, and a broadband white light source. Interferograms and transformed spectra are presented.

Lastly, chapter 6 summarizes the findings of the project and discusses the various avenues for future work. It outlines the outstanding challenges and potential directions to improve the performance of the instrument and to achieve a higher TRL.

CHAPTER 2

2.0. BACKGROUND AND THEORY

Earth's atmosphere contains many radiatively active molecules that selectively absorb incoming solar radiation in different spectral regions. In the far-, mid-, and near-infrared (NIR) wavelength range, these molecules have specific rotational and vibrational modes which select the frequencies of the radiation absorbed. This chapter expands on concepts related to the research and development of the IFTS. The general structure of the Earth's atmosphere is discussed along with the role of the most important greenhouse gases specifically water vapour, carbon dioxide (CO_2) and methane (CH_4). The role of remote-sounding measurements of the oxygen A-band (O_2-A band) is described. The intrinsic properties of these greenhouse gases and their impact on climate change are outlined. In addition, the methods and techniques used to detect their concentration in the atmosphere are presented. The principles of Fourier transform spectroscopy and its advantages over other techniques is also discussed.

2.1. Greenhouse gases

Greenhouse gases such as carbon dioxide and methane are essential to sustain a habitable temperature for the planet. In the absence of these gases, it is estimated that the average surface temperature on the Earth would be about -18 ^{o}C rather than the present value of +15^{o}C [15]. While water vapour is the most significant radiatively active gas, its concentration in the atmosphere is mostly controlled by temperature, which, in turn, is driven by the other greenhouse gases. One of the greatest, current environmental concerns is the release of Greenhouse Gases (GHGs) into the atmosphere. An unprecedented increase in GHG emissions

occurred after the industrialization of nations. Figure 1 shows changes in the atmospheric greenhouse gas concentrations of carbon dioxide and methane over the last 10,000 years, measured using ice and fern data [16].

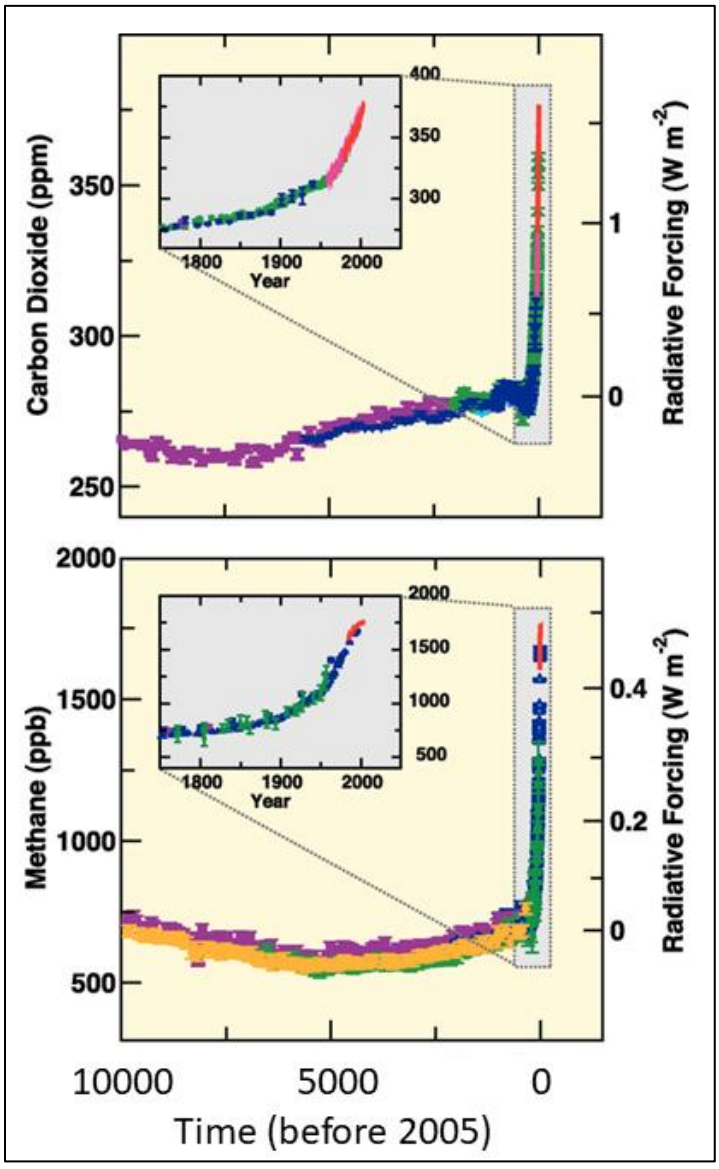

Figure 1: Changes in atmospheric CH_4 and CO_2 over the last 10,000 years [16]

A major cause of the increase of GHGs, like CH_4 and CO_2, is anthropogenic. This has consequently affected the energy balance of the climate system by absorbing the thermal

radiation emitted from the Earth causing radiation to be trapped as heat within the Earth's atmosphere. The trapping of heat causes the warming of Earth. The impact of the increase in GHGs is evident from the changing climate around the world. On the global scale, between 1850 and 2012, the Earth's surface temperature has increased by 0.85 (+/- 0.20) ^{o} C and the mean sea level has risen by 0.19 (+/- 0.02) m between 1901 and 2010 due to the melting of glaciers and ice sheets [17].

2.1.1. Atmospheric carbon dioxide (CO_2)

As a part of the global biogeochemical cycle, carbon is exchanged among the Earth's soil, rocks, oceans and within the biosphere [18]. The concentration of carbon dioxide in the atmosphere is at the centre of climate change theory and policy. The scientific consensus is that the release of carbon dioxide and other greenhouse gases should be limited if humans want to reduce their effect on the climate [21].

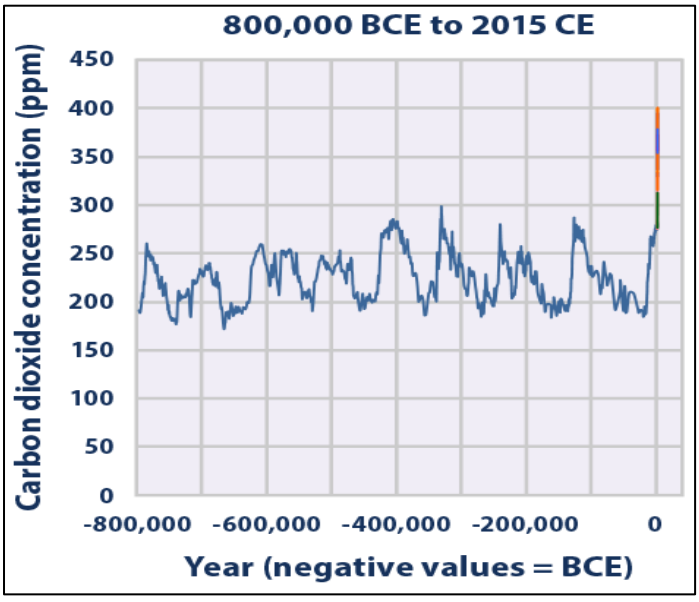

Figure 2: Global atmospheric concentration of carbon dioxide over time. [25]

Figure 2 shows the global atmospheric concentration of carbon dioxide over time for the past 800, 000 years up until May 2015, measured from a variety of ice core studies and recent air monitoring sites around the world [26]. Over this period, CO_2 has varied largely between 280 and 180 ppmv i.e., a change of only 100 ppmv. If Earth's geological history is divided into the glacial period (colder times) and interglacial times (warmer times), the rate of increase of atmospheric CO_2 from interglacial to glacial periods appears to be quite small. The recent rate of increase is unprecedented. Since the beginning of the industrial era, the mixing ratio of carbon dioxide has increased substantially, from an annual average of 280 ppmv in the late 1700s to 401 ppmv in 2015, with an increase of 100 ppmv just in the past 57 years alone. [22]. It has broke the 400-ppmv threshold, considered to be the highest level in the last three million years [24].

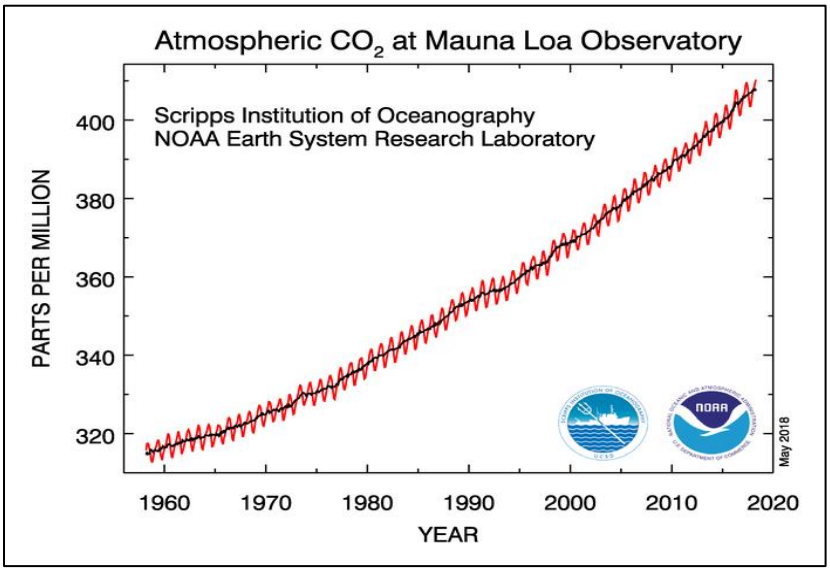

Figure 3: Monthly mean atmospheric carbon dioxide at Mauna Loa Observatory, Hawaii [26].

Figure 3 illustrates the rapid increase in the carbon dioxide trend with red colour, measured as the mole fraction in dry air at Mauna Loa from March 1958 to May 2018. The red curve shows

frequently taken data, the black smoothed curve plots the seasonally corrected data. Mauna Lao provides a good background measurement to monitor the global signal of atmospheric CO_2 because of its elevation and location away from industrial centres.

2.1.1.1. Carbon dioxide as a greenhouse gas

Since pre-industrial times, the increases in atmospheric CO_2 has been responsible for a radiative forcing of +1.66 ± 0.17 W m^{-2} [21]. This has disrupted the global carbon cycle and has led to planetary warming. Oceanic and terrestrial sinks take up some of the CO_2 emitted by fossil fuels and land-use change (e.g. deforestation) while the residual represents the atmospheric accumulation of CO_2.

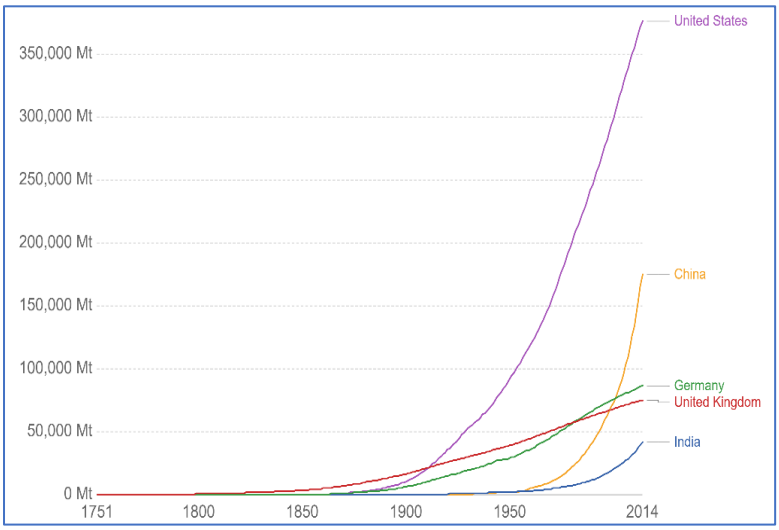

Figure 4: Cumulative carbon dioxide (CO_2) emissions measured in million tones since 1751 [27] [28]

Figure 4 displays cumulative CO_2 emissions from 1750 to 2014 for major emitting countries. During the industrial revolution, the UK was the first country to release CO_2 in large amounts. Other European countries and the US followed shortly thereafter and became the largest producers over most of this period. In the last few decades, China's rapid growth in emissions

have made it the world's second-largest cumulative emitter but still at less than half of the US total.

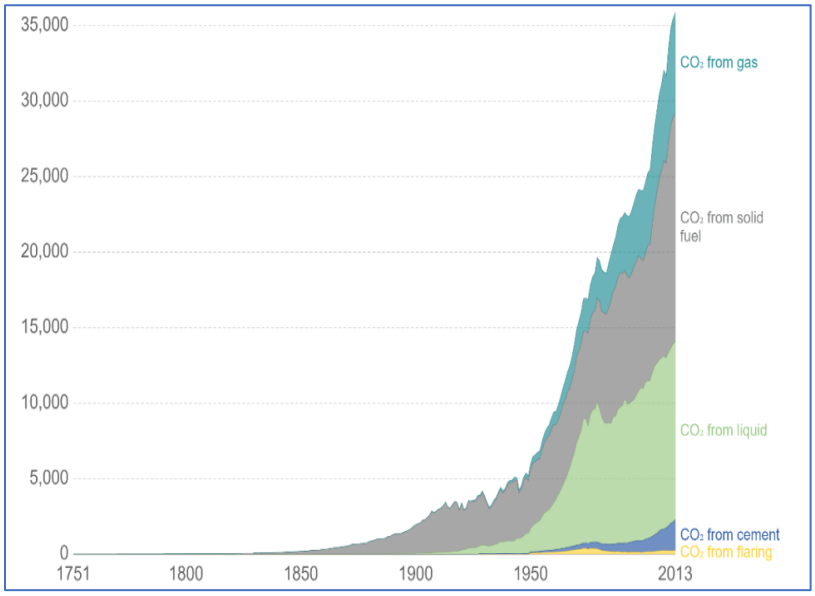

Figure 5: Annual CO_2 emissions in million tonnes from solid fuel, liquid, gas, cement production and gas flaring. [29] [30]

Figure 5 shows that a wide range of fuel types are associated with energy and industrial CO_2 emissions. During the early 1700s, coal-fired power at an industrial-scale emerged in Europe and North America [29] [30]. By the late 1800s, emissions from oil and gas production became significant. After that, a century passed before cement production and flaring started emitting large-scale amounts of CO_2. Solid and liquid fuels still dominate today with gasoline production being the leading source.

Of all the GHGs, CO_2 gets the most attention because of its long lifetime in the Earth's atmosphere. Natural processes to remove that remove emitted CO_2 from the atmosphere vary widely in time from 5 years (fast cycling processes) to hundreds or thousands of years (absorption through land vegetation, soils and cycling into the deep ocean). It is estimated that

even if humans stop emitting CO_2 now, it would still take several hundred years before the majority of it would be removed from the atmosphere [17].

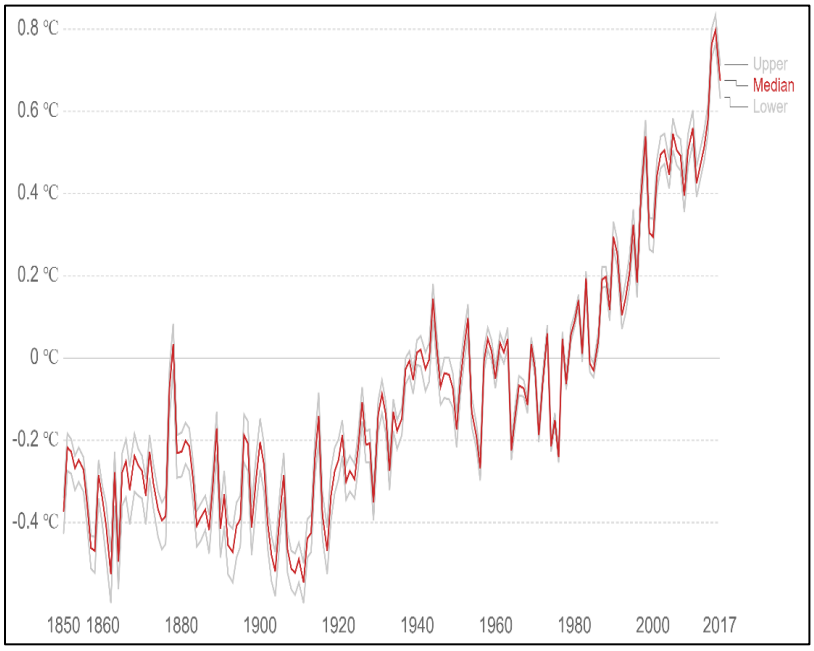

Figure 6: The global average land-sea temperature anomaly relative to the 1961 - 1990 average temperature in °C. The red line represents median average temperature change, and the grey lines represent the upper and lower 95% confidence intervals. [33] [34].

Global warming and climate change have a range of potential ecological and physical impacts on planet Earth. Figure 6 shows the global average temperature anomaly from the 1961 to 1990 average. The x-axis represents the time span from 1850 – 2017 and y-axis represents the global average temperature change from 1961 – 1990 baseline temperature. The average annual temperature trend is shown by the red line whereas the upper and lower confidence levels are shown in light grey. The temperature has risen sharply by approximately 0.8 degrees over the last few decades and was about 0.4 degrees colder in 1850. This suggests a global temperature increase of 1.2 degrees since pre-industrial times. Due to the global temperature

increase, a limiting average warming target of 2 ^{o}C above pre-industrial temperatures has been set by the UN members [32].

2.1.2. Atmospheric methane (CH_4)

Methane is the most abundant organic chemical [35] and the second most important anthropogenic greenhouse gas in the Earth's atmosphere [17]. It is the third most abundant GHG in the atmosphere after water vapour and CO_2, which makes it the most abundant reactive trace gas in the troposphere. Its reactivity plays an important role in both tropospheric and stratospheric chemistry. Its oxidation by the hydroxyl radical (OH) in the troposphere produces formaldehyde (CH_2O), carbon monoxide (CO), and, with sufficient nitrogen oxides (NO_x), leads to ozone (O_3) production.

2.1.2.1. CH_4 as a greenhouse gas

In 1948, the first unambiguous detection of methane in Earth's atmosphere was done by observing its infrared absorption bands in the solar spectrum [36]. In 2005, the global average amount in the atmosphere was measured at 1,774.62 ± 1.22 ppb [16]. The global warming potential (GWP) provides the global warming effect of GHG emissions relative to CO_2 over a set period. CH_4 has a GWP of at least 34 times larger than CO_2 over 100 years [17]. Since pre-industrial times, increases in atmospheric CH_4 concentrations have contributed to a radiative forcing of +0.48 ± 0.05 W m^{-2} [23].

Methanogenic micro-organisms produce methane in large amounts during respiration. In wetlands and irrigated rice paddies they are responsible for anaerobic decomposition [37]. Methane is also produced by decomposition in landfills, enteric fermentation in ruminants

(animals), and termites. Processes such as biomass burning, coal mining or processing, natural gas production and consumption all act as abiogenic sources of methane. In an urban environment, pipe leaks in city infrastructure and individual homes release a significant amount of CH_4 all year round [38].

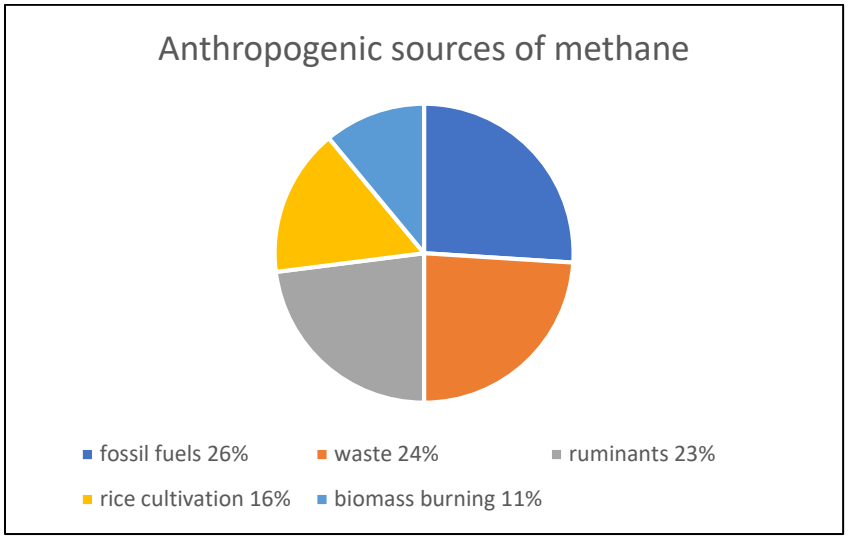

Figure 7: Contribution of anthropogenic sources of methane [39]. Data from IPCC 1995 [40]

Figure 7 shows the contribution of individual anthropogenic sources of methane. The largest emissions are from fossil fuels followed by waste, ruminants, rice cultivation and biomass burning.

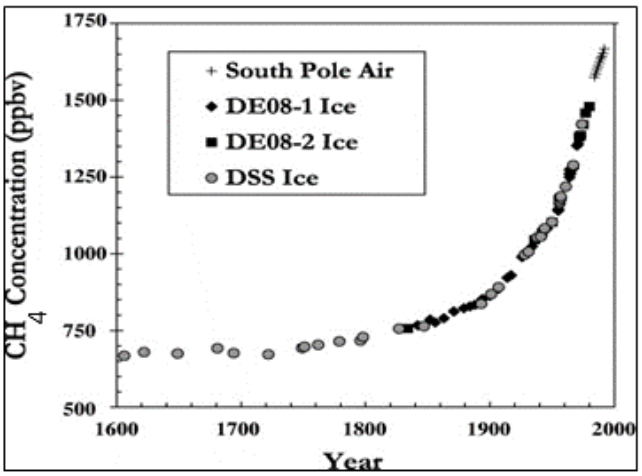

Figure 8: This figure illustrates the increase in atmospheric methane from pre-industrial times to the present using ice core and atmospheric records [50].

Figure 8 shows observations of methane concentrations from ice core and ground-based polar stations. The methane levels have increased to more than double that of pre-industrial times and continue to increase [39] [41] [42] [43] [44] [45]. The majority of the increase in emissions is believed to be caused by anthropogenic sources [46] [47] [48] [49].

Due to limited transport to the stratosphere, some amount of CH_4 is also lost from the troposphere. Soils and agricultural fields also act as methane sinks [51]. With an increase in the use of nitrogen fertilizers and land use change, the uptake of methane by soils has decreased [52] [53]. Carbon dioxide has been the centre of concern for anthropogenic climate change because of its rapid increase in the atmosphere. The climate system has a faster response to methane, with its short residence time in the atmosphere as compared to CO_2 with its much longer residence time [54]. A continuous record of the atmospheric concentration of methane can be derived from air bubbles trapped in polar ice [55] [56] [57] [58] [59] [60] [61] [62] [63]. Figure 9 shows atmospheric CH_4 and temperature since 420,000 years BP [64] covering four glacial-interglacial cycles. Year 0 BP corresponds to 1950 AD.

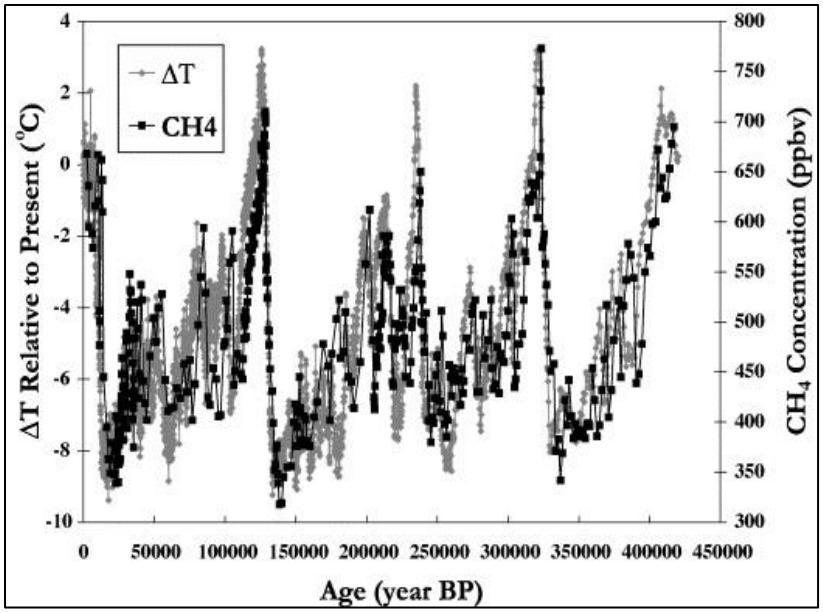

Figure 9: Atmospheric temperature and methane concentration (volume mixing ratio) derived from Vostok ice core records from 420, 000 years BP to present [65].

Figure 8 and 9 suggests that present-day CH_4 levels are unprecedented as compared to anytime in history. Glacial-interglacial periods show a variability of 320 – 350 ppbv to 650 – 780 ppbv [65] which corresponds to a source increase of about 50 – 60 $TgCH_4$/year [66] [67]. This is less than half of the present-day concentrations which are greater than 1700 ppbv [16]. A second clear observation from Figure 9 is the phase correlation between CH_4 records and atmospheric temperature records [68] [69] [70] [71]. Methane oxidation is also an important source of water vapour in the stratosphere.

2.2. The Arctic

The Arctic often has extensive snow coverage between eight to nine months of the year. The surface albedo at specific sites changes dramatically with the occurrence of snow and influences the energy balance of the site. The positive feedback between surface temperature,

surface albedo, and ice content has proved the Arctic to be one of the most sensitive regions on Earth [73] [74] [75] [76] [77] [78].

Permafrost is defined as ground that has remained frozen for two or more consecutive years and is at least 3 feet thick [79]. It covers about 15 million km^2 of land surface which constitutes about 24% of land in the Northern hemisphere [80]. Varying amounts of ice binds the rock, soil, and sediments contained in the permafrost. The positive feedback between permafrost thaw and the release of greenhouse gases such as CO_2 and CH_4 has accelerated climate change in the region [81] [82]. About 4 million km^2 of permafrost is predicted to be lost through thawing for every 1 ^oC increase in temperature [83]. There are about 1300 Pg (1 Pg = 10^{15} grams) of organic carbon is contained in the permafrost-affected landscapes of the northern regions out of which about 800 Pg is perennially frozen in the permafrost [84]. This accounts for about 50% of the estimated global below-ground organic carbon reserves [85]. Most seasonally unfrozen wetlands act as methane sources which influence the atmosphere above the Arctic by introducing 3 – 9 % of net land-produced CH_4 (15 – 50 Tg) per year [86].

The currently frozen carbon is expected to undergo microbial decomposition due to the predicted thawing of permafrost [87]. The decomposition is slowed down due to anoxic conditions in the water-saturated soils but at the same time enables the formation of CO_2 and CH_4 [88]. A variable amount of CH_4 produced because of thawing is oxidized to CO_2 when passing through oxic soils or sediments [89]. The Arctic permafrost soils have already shown an enhanced thawing due to temperature rise over the last decades [90]. This has caused problems for the Arctic ecosystem which includes the release of GHGs (CO_2 and CH_4), increased outflow of meltwater in rivers and other water bodies causing erosion of peat layers above

frozen soils. This further results in the leaching of Dissolved Organic Carbon (DOC) which is bound up in ice particles [91]. The erosion mechanism of coastlines and submerged permafrost is not expected to be sufficient to release much CH_4 out of gas hydrates to have any influence over Radiative Forcing (RF) [92]. Thawing is predicted to increase precipitation and temperature which is likely to extend Arctic wetlands [93]. If the carbon reservoirs are further de-stabilized because of the predicted climate change, it will imply a global-scale feedback [94] [95]. Northern wetlands will convert from a GHG sink to a source even with relatively low CH_4 fluxes [96] [97] [98]. Assessing the climate change targets of COP21 [99], it is estimated that the permafrost area would be reduced by over 40% if the climate is stabilized at 2 ^oC above pre-industrial levels, however, this loss would be reduced by about 2 million km^2 if a 1.5 ^oC stabilization is achieved.

Considering the sensitivity of the Arctic, there is an urgent need to develop scientific instruments that can be flown in space over the Arctic to monitor the GHGs in the atmosphere and to quantify their sources and sinks. Satellites provide a better-quality global observation of Earth as compared to surface observations. They eliminate the data sparse coverage of the polar caps and provide a comprehensive set of data.

2.3. O_2 – A band

The O_2-A absorption band centred at 762 nm was first used in the 1960s to measure cloud top height or apparent surface pressure [101]. There are two major reasons for the preference of O_2-A band: firstly, the distribution of O_2 is well known throughout the atmosphere, and

secondly, there are no other contaminating species such as water vapour within the same spectral region to affect its optical depth and path length.

The oxygen molecule does not have a permanent electric dipole due to its symmetry, but unpaired orbital electrons give rise to a permanent magnetic dipole moment resulting in the radiative activity of the molecule. The strength of magnetic transitions is typically orders of magnitude less than the electric dipole transitions [103]. But in the atmosphere, the great abundance of oxygen molecules relative to other molecules compensates for these weak transitions. This results in a large atmospheric absorption.

2.4. Absorption spectroscopy

All atoms and molecules absorb and emit radiation because of transitions between energy states. The Lambert [105] and Beer [106] law given in equation 2.1 can be used to describe the attenuation of light by a gas:

$$\frac{dI(\tilde{\nu})}{dl} = -\sigma(\tilde{\nu})I(\tilde{\nu})C \tag{2.1}$$

where

C = number of particles per unit volume [m^{-3}]

l = absorption path length [m]

$\sigma(\tilde{\nu})$= absorption cross-section [m^2]

All information about the sample is incorporated in the absorption cross-section, making it a complex and a particularly interesting variable.

Various factors such as, the population of energy states, and the path length of the sample affect the intensity of the spectral lines [104]. The wavenumber dependence of a spectral feature near the line position defines the spectral line shape. The lines resolved by a spectrometer are not infinitely narrow but have a finite width due to various mechanisms as discussed in Appendix I.

2.5. Fourier transform spectroscopy basics

An optical interferometer is an instrument that utilizes the interference of light waves and displays fringes produced by a change in path length [118]. Fourier transform spectrometers rely on the same principle as optical interferometers, such as the Michelson interferometer.

The York IFTS is a modified Michelson interferometer which consists of a beam splitter, two perpendicular mirrors and a photodetector as shown in Figure 10.

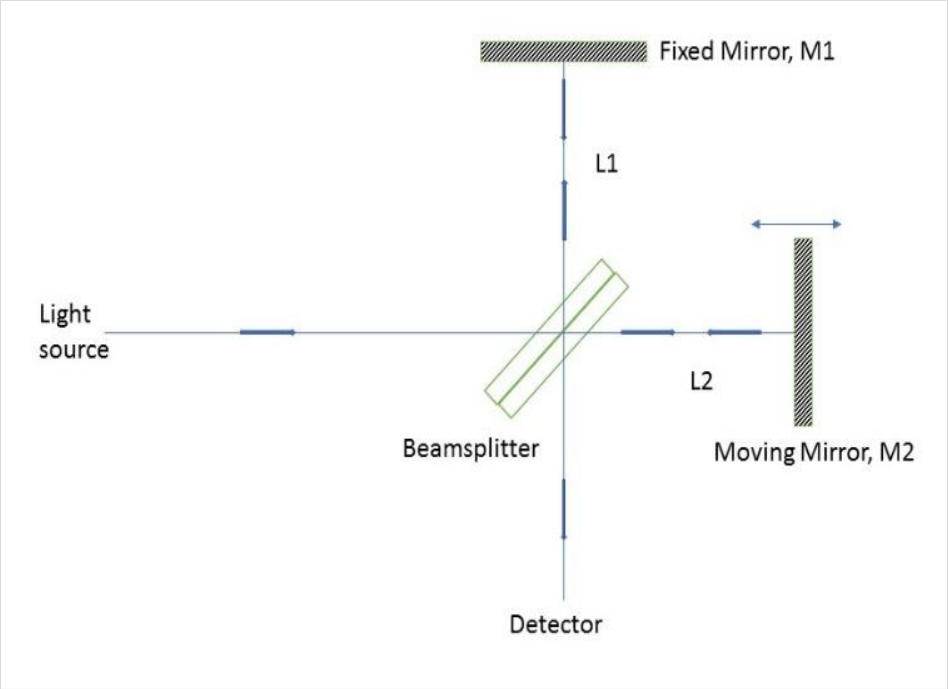

Figure 10: Schematic of a two-plane mirror Michelson interferometer [119]

Light from the source travels in a straight line (optical axis) and interacts with a beam splitter at an angle of 45^{o}. The beam splitter splits the amplitude of the light into two approximately equal parts. One-half of the light is transmitted and the other half is reflected. The latter beam is then reflected at the mirror M1 and the former is reflected at the mirror M2 to recombine again at the beam splitter. This recombined signal is then detected at a photodetector.

When the moving mirror (M2) is at initial zero position, the path L1 travelled by the reflected light equals the path L2 travelled by the transmitted light. Both light beams will have travelled the same distance from the splitting point to again recombining at the beam splitter. Therefore, both light contributions are in-phase and interfere constructively. At this moment, the intensity recorded by the detector is at a maximum. As the mirror M2 moves from the initial zero position, the L1 starts to change and introduces a non-zero optical path difference (OPD). As a result, a phase difference between the two light beams is introduced and the intensity recorded on the detector starts to decrease. The optical path difference experienced by the beam is double the mirror's displacement since the OPD accounts for the extra distance travelled to and from the moving mirror. With continuing displacement of M2, in the case of monochromatic radiation, the detector measures a sinusoidally-varying intensity which is a function of the displacement of M2 with a period of $\lambda/2$. This signal is referred to as an interferogram, which is basically the autocorrelation function of the observed light. Figure 11 shows the wavefronts of a monochromatic source being propagated through an interferogram.

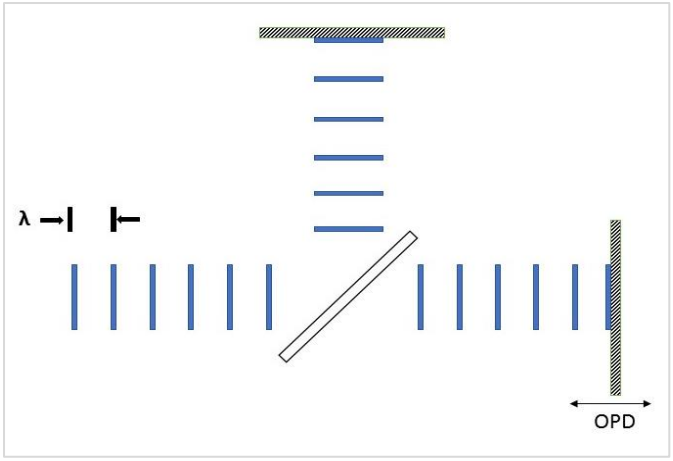

Figure 11: Monochromatic waves at zero OPD [119]

The Fourier transformation of the interferogram is the spectrum of the incoming light as a function of wavenumber (or 1/wavelength). The data can also be acquired as a function of time as mirror moves during the scan as opposed to mirror position. Doing the Fourier transform on such an interferogram will produce a spectrum as a function of frequency. For a monochromatic source, the interferogram produced is a sine wave whereas, for a polychromatic incoming beam which consists of two or more wavelengths, the interferogram produced has a more complex behaviour as a function of path difference.

Figure 12 shows the interferogram of a monochromatic source centred at 1000 cm^{-1} which is a pure sine plot and Figure 13 shows the transformed spectrum.

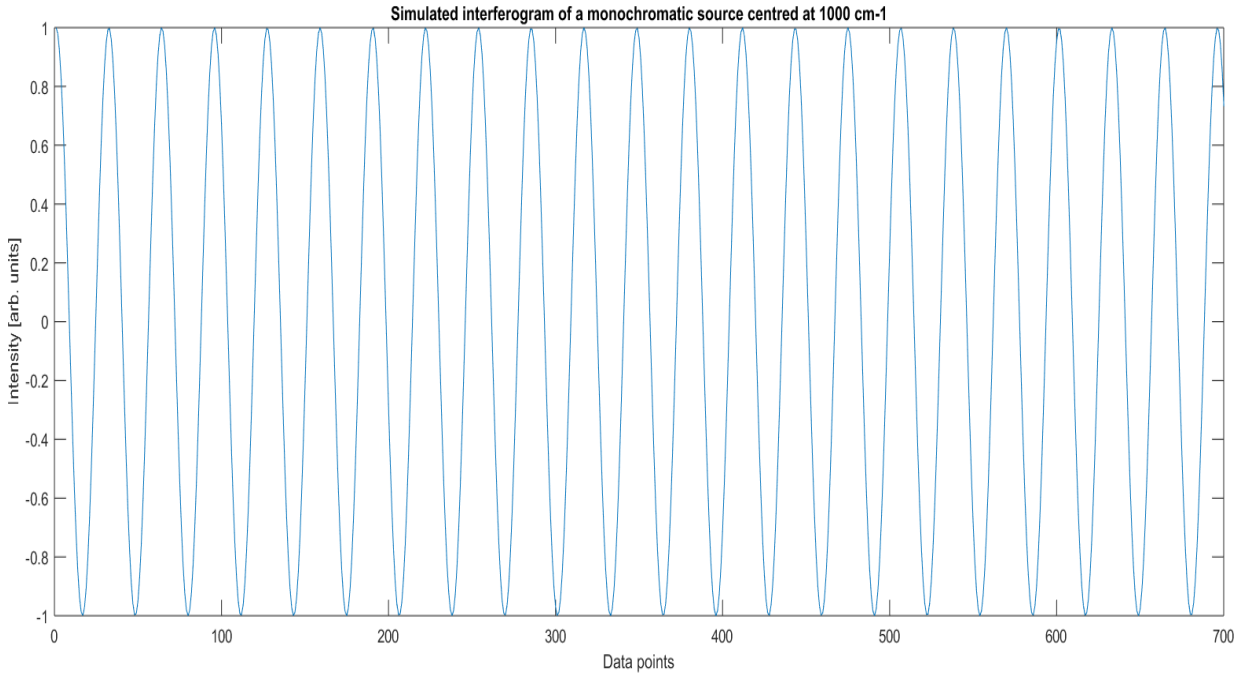

Figure 12: Simulated interferogram of a monochromatic source centred at 1000 cm^{-1}. The sinusoidal function is a result of the monochromatic behaviour of the input light.

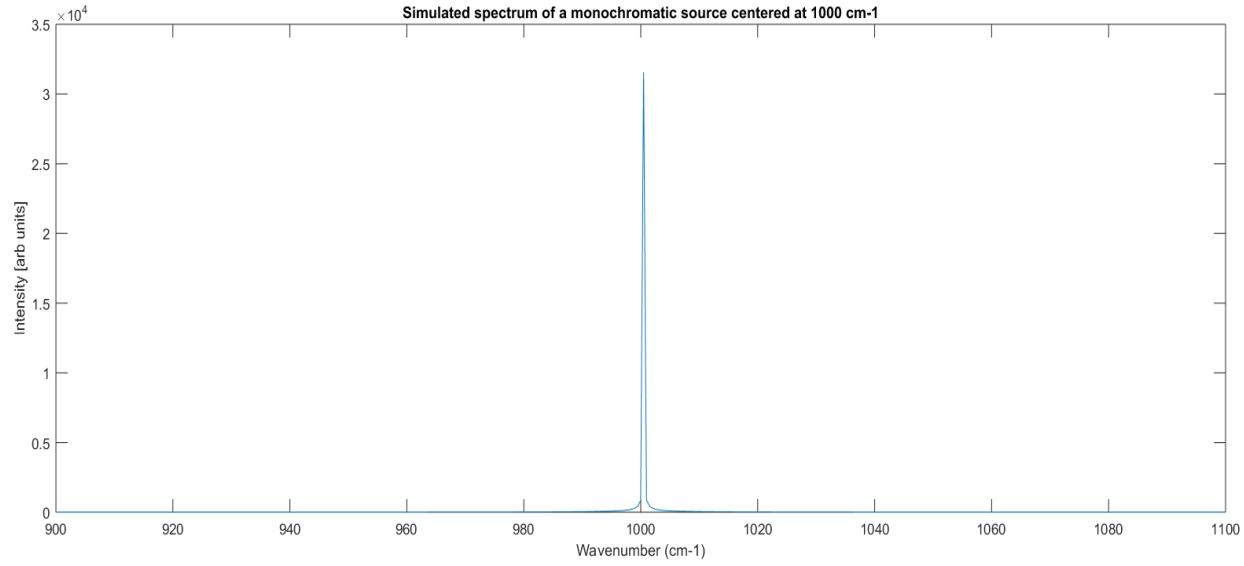

Figure 13: Simulated spectrum of a monochromatic source centred at 1000 cm^{-1}.

If this interferogram had been of infinite length, then the transform of it would have produced a delta function. But in real life, the interferograms are of finite length as dictated by the

maximum optical path difference. Given this, the line shape derived from a finite interferogram is degraded by the "instrument" function and has a width as shown in Figure 13. In mathematical terms, the limited spectral resolution of the final spectrum is caused by the convolution of the original line shape with a function that depends on the properties of the instrument and the sampling technique.

The quantitative overview of the Fourier transform spectroscopy is discussed in Appendix II.

2.6. Instrument response of Fourier transform spectrometer

Spectrometers suffer from real-world deviations from ideal performance which need to be considered during the design and development process. These deviations can arise from different sub-sections of the instrument, for example, the optical, electronics or detector subsystems [124]. The following sections 2.6.1 to 2.6.2 provide a review of artefacts contributed by real instruments.

2.6.1. Duality

Two major dualities exploited by an interferometer are time-frequency and angle-space. The former is at the centre of the basic principle of an interferometer's operation whereas the later is an inherent property of an imaging interferometer.

2.6.1.1. Time-frequency duality

A Fourier transform spectrometer produces the spectrum of light by measuring the changing interference pattern in the time domain. Henceforth, the time-frequency duality used by an interferometer is illustrated by equation 2.11 in Appendix II where data are acquired in the

spatial domain (or optical path difference domain) and is related to the spectral (wavenumber) domain. Due to this relationship, any distortion of the signal in one domain affects the observed measurement in the other domain. The greatest of all is the effect of limited observation time (or optical path difference) which determines the maximum resolution of an interferometer.

Equation 2.11 in Appendix II describes the integration of an interferogram overall X from -∞ to +∞ to obtain the true spectrum of the source. This is not feasible in real-life measurements. The optical path difference induced by the mechanical displacement of the mirror in an interferometer is limited by its maximum ΔX_{max}. The maximum mechanical path difference introduces a maximum optical path difference which is referred as MOPD or $\Delta X_{o,\,max.}$ This limits the equation 2.12 within integration limits of +/- $\Delta X_{o,\,max.}$

2.6.1.2. Angle-space duality

In addition to the time-frequency duality, angle-space duality is also important to understand the behaviour of Fourier transform spectrometers. It defines the relationship between the position of the detector element with the angles of light propagation in the interferometer. In most cases, this detector element acts as the field stop of the optical system.

In most of spectrometers, the optical system can generally be divided into three basic components: source, a dispersive element, and detector [125]. The optical domains of an interferometer are shown in Figure 14 where the numbers 1, 2, and 3 identify the source, modulator, and detector respectively.

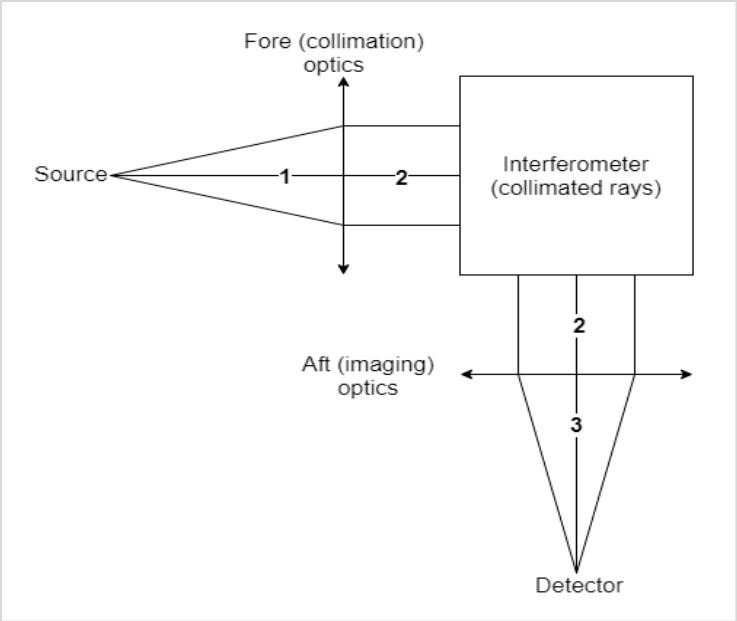

Figure 14: Basic optical components in a Fourier transform spectrometer. Identifiers 1, 2, and 3 represent the source, modulator, and detector [125]

Light rays coming from a source at infinity are collimated for an interferometer using fore-optics. Collimating optics can range from a simple lens or mirror for an optical bench spectrometer to a complex telescope system used for astronomy. After modulation of this light by the interferometer, it is focused onto the detector plane using aft (imaging) optics.

Each image plane point corresponds to a specific angle in the optical domain of the interferometer. Figure 15 illustrates the relationship between space and angle for an ideal paraxial optical system of focal length f:

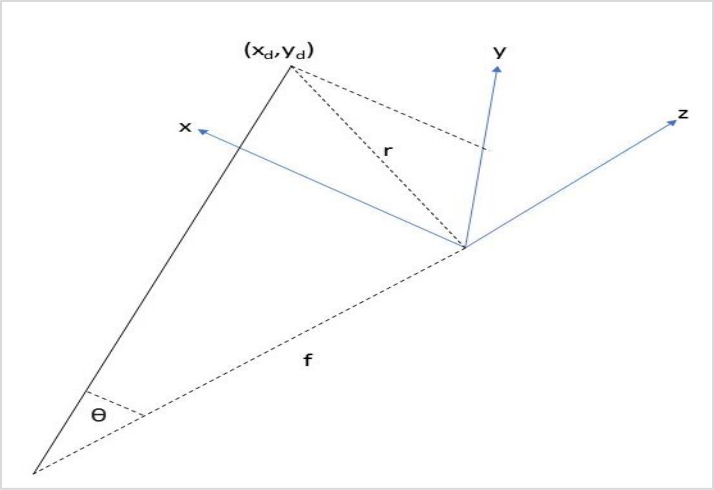

Figure 15: Angle-space relationship for the optical domain of an interferometer.

where,

f = focal length

z = 0 defines the image (detector) plane.

r = radial distance of an off-axis pixel from the centre pixel and

(x_d, y_d) defines the position of the centre of the pixel.

Θ = off-axis angle

The image plane is normal to the propagation of the optical axis; from Figure 15 above:

$$\theta = \arctan(r/f) \tag{2.22}$$

where,

$$r = \sqrt{x_d^2 + y_d^2} \tag{2.23}$$

Therefore, each pixel on the detector array corresponds to a certain off-axis angle which can be used to define the source of incoming light beam in spatial terms.

2.6.2. Optical effects

This section discusses the effects arising from various optical components and from their interaction in an imaging FTS. They are crucial for the optical system design.

2.6.2.1. Effects of optical misalignment

Optical alignment plays a crucial role in Fourier transform spectrometers. Misalignments of optical components can affect the spectral response and resolution of the instrument depending upon the instrument design and optical layout. Misalignment can be classified into two types: static and dynamic which results in relative shearing or tilting of the wavefront. Misalignment of one of the retro-reflectors gives rise to static misalignment whereas irregular displacement of the moving mirror produces dynamic misalignments. Tilting occurs when the angle between the beams coming from the two arms of the interferometer are mismatched and shearing occurs due to a spatial displacement perpendicular to the beam axis. Both tilt and shear can be treated in similar ways [126] [127]. The tilt and shear effects the collinearity of the retro-reflection from each mirror and creates a moiré pattern instead of fringes [126]. The use of corner cubes as retroreflectors, as opposed to plane mirrors, makes the interferometer immune to tilt errors but does not reduce the sensitivity to beam shear. ACE-FTS achieved compensation for both tilt and shear by using a double pass optical layout [128] [129] [130]. Since the York IFTS uses a single pass optical layout, it is expected to be sensitive to shear but this study does not explore this subject other than to note that the system is producing an acceptable modulation efficiency.

2.6.2.2. Effect of imaging optics

In an ideal case scenario, the relationship with a displacement of the mirror and resultant optical path difference on the principal optical axis can be described as equation 2.24:

$$\Delta X_o = 2\,\Delta X_m \tag{2.24}$$

where,

ΔX_m = maximum mechanical displacement of the mirror

ΔX_o = maximum optical path difference (OPD) of a plane wave parallel to the optical axis

This discusses the geometrical response of using imaging optics and how they can be exploited as angle-space duality to define the relationship between the position of detector element with the angles of light propagation in the interferometer. Figure 16, and 17 show the effect of input light propagation from an off-axis source.

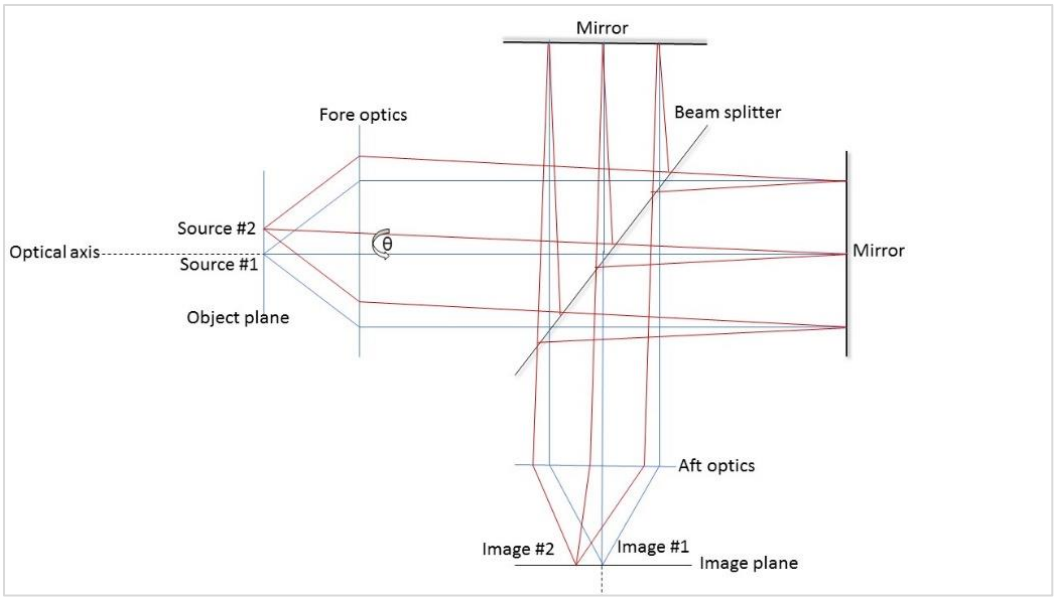

Figure 16: A schematic view of Fourier transform spectrometer with an on-axis and an off-axis source. Later leading to a propagation at an angle Θ through interferometer domain. Image #1 and image#2 are formed by source #1 and source #2 respectively.

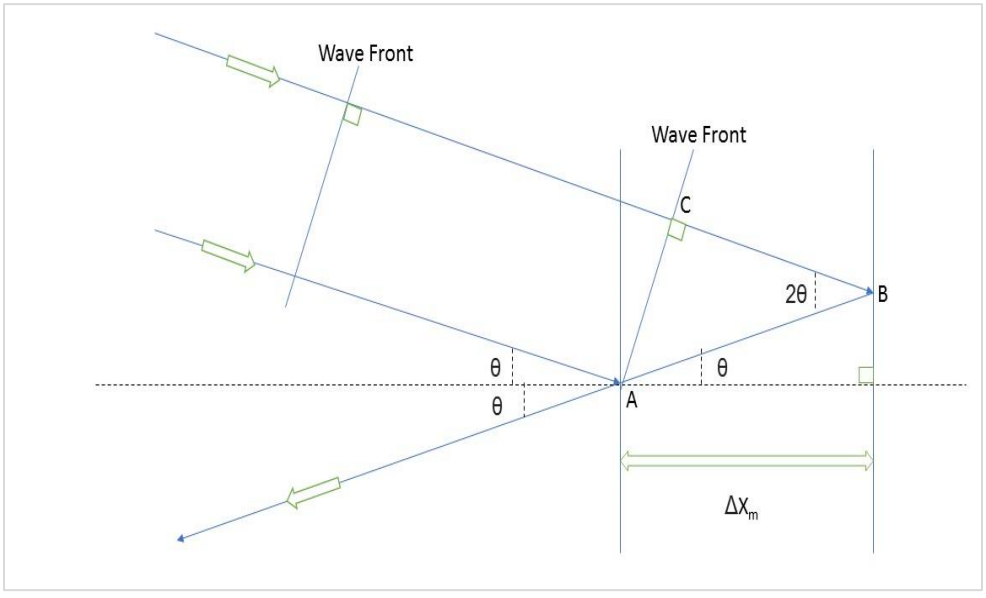

Figure 17: Propagation of input light from an off-axis source.

From Figure 17, the (OPD) of an off-axis plane wave travelling at an off-axis angle θ is given by:

OPD = AB+BC = ($\Delta X_m/\cos\theta$) + ($\Delta X_m \cos 2\theta /\cos\theta$) (since BC = AB. cos2θ) (2.25)

$$= \frac{\Delta X_m}{\cos\theta}(1 + \cos 2\theta) \quad (2.26)$$

$$= \frac{\Delta X_m}{\cos\theta}(1 + 2\cos^2\theta - 1) \quad (2.27)$$

$= 2\Delta X_m \cos\theta$ or $\Delta X_o \cos\theta$ (2.28)

Therefore, a beam travelling at an angle θ experiences an optical path difference of factor cos θ of the beam travelling parallel to the optical axis. Henceforth, X_0 is a function of off-axis angle θ.

$$S(\sigma, \theta) = \int_0^\infty I\, exp(-i2\pi\sigma\, X_0 \cos\theta)\, d\sigma, \quad (2.29)$$

or,

$$S(\sigma, \theta) = \int_0^\infty I\, exp(-i2\pi\, X_0\, \sigma \cos\theta)\, d\sigma \quad (2.30)$$

which shows that the spectra recorded at an optical path difference of X_0 correspond to the wavenumber $\sigma\cos\theta$, where σ is the wavenumber recorded at the centre (on-axis) pixel. The wavenumber recorded at an off-axis pixel is a factor cos θ of the wavenumber recorded at the centre pixel.

Another effect of using imaging optics is the aberrations caused by the focusing lens. If aberrations such as spherical, coma, and astigmatism are combined, the angle-space relationship can only be solved using ray tracing numerical methods. The point spread function (PSF) for the focusing lens used in York IFTS is discussed in section 3.3.

2.7. Imaging FTS concept

When a Michelson interferometer is inserted into the collimated beam of a camera system, the result is an imaging Fourier Transform Spectrometer (IFTS). The scene intensity as input light is

modulated by the interferometer and recorded by the detector at each exposure. The light transmitted to the detector has all the wavelength components of the scene past by any band-limiting filter in the optical train, and, hence, results in the significant light-gathering capability of such a spectrometer. A series of broadband images of the different interference pattern is collected at each exposure and this data is known as the "interferogram cube" [131]. The cube has 2D spatial information from the images of the entire field of view captured at once and the third dimension is the OPD which provides the spectral information. This increases the efficiency as compared to a non-imaging system by eliminating the need to raster across a scene to produce the data cube. Each pixel on the detector records the variation of light intensity as a function of mirror position referred to as an interferogram and two orthogonal directions of the detector captures the 2D scene. In a spectrograph, a different wavelength element is observed at each step as opposed to in an IFTS, in which the whole incident bandpass is observed at once but at a different OPD at each step. The total number of frames per data cube is dictated by the maximum OPD and the Nyquist sampling requirement (refer to section 3.7.2). This number represents the spectral resolution elements for an IFTS. The volume of the cube for the same scene can be increased by increasing the OPD which results in a greater number of frames acquired. The Fourier Transform (FT) routine is performed on the interferogram acquired by each pixel in the field of view to recover the spectral information of the data cube [131].

The greatest disadvantage of an IFTS is the long time required to scan through the range of optical path differences. It makes observing fluctuating sources relatively difficult. Any significant variations in the intensity of the observed light within the spectral frequency of

interest translates as noise in the derived spectrum. This can also result in shifting of spectral features for a periodically fluctuating light source such as an AC modulated calibration source. This aspect of an IFTS can be converted into an advantage under certain circumstances. The broadening of a narrow spectral feature can be used as a measure of the degree of fluctuations of the source term. This provides information to distinguish transient or erratic spectral features. Another disadvantage is the requirement for a high degree of computational power to produce useful information from the acquired data.

2.8. Applications of imaging Fourier transform spectrometer

This section highlights the use of IFTS instruments in scientific fields. Shepherd et al. [94] provide a history of the development of field-widened Michelson interferometers in Canada. The use of FTS in astronomy is quite new and is still a developing technology. FTS has also been applied to measure emission and absorption line profiles in the Earth's atmosphere. Similar instruments have been an integral part of payloads for planetary exploration such as Mariner, Voyager, and recently on Cassini [134]. An FTS was also used at Kitt Peak's Mayall telescope during the 1970's and 1980's to provide exquisite spectra of late-type stars [135] [136]. A high-resolution FTS at the Canada-France-Hawaii Telescope (CFHT) was widely used on a large variety of Planetary and stellar programs [137] [138]. The CFHT was renamed to Bear after it was made able to work on the imaging mode in early 1990's [139]. It provided integral field spectra of a variety of objects such as planetary nebulae, massive star clusters and star-forming regions in a 24-arcsecond field of view [140].

2.8.1. Instruments in operation

FTS instruments have been part of many atmospheric missions over the past couple of decades. Infrared Radiation Interferometer Spectrometer (IRIS) was the earliest space-borne FTS instrument and was launched by NASA in the 1960s [141]. It covered a spectral range of 5 to 25 µm with a resolution of 5 cm^{-1} to measure the spectrum of IR radiation emitted to space by the Earth and its atmosphere. The second-generation FTS instruments provide ultra-high spectral resolution of about 0.5 cm^{-1} and vertical resolution of 1 to 2 km.

2.8.1.1. ACE-FTS

The Atmospheric Chemistry Experiment-Fourier Transform Spectrometer (ACE-FTS) is the primary instrument onboard the Canadian science satellite, SCISAT, spacecraft launched on August 12, 2003 [142]. The Infrared Fourier Transform Spectrometer (FTS) is a high-resolution (0.02 cm^{-1}) modified Michelson interferometer which covers a wide spectral range from 2.2. to 13.3 um, or 750 to 4400 cm^{-1}. Both detectors have the same circular Field of View (FOV) with an angular diameter of 6.25 mrad and are cooled to 80-100 K by using a passive radiator pointing towards cold, deep space as shown in Figure 18. It uses a pendulum design (scan mechanism mounted on a single pivot) with corner cubes acting as retro-reflectors and a Zinc Selenide (ZnSe) circular disc which acts as beam splitter and compensator as illustrated in Figure 19. ABB Inc. in Quebec City designed and manufactured the ACE-FTS instrument [143]. The high resolution and compact size are achieved by using a folded and double passed optical layout.

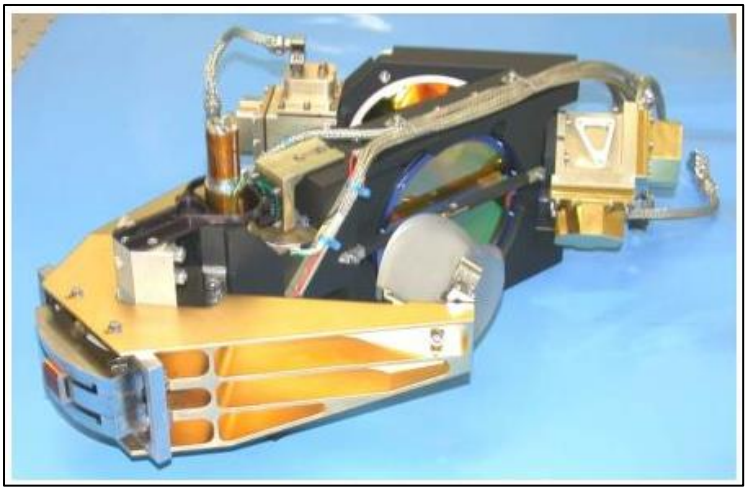

Figure 18: ACE FTS interferometer subsystem [143]

Figure 19: ACE FTS instrument package

ACE measures the chemical and dynamical processes that affect the distribution of ozone in the upper troposphere and stratosphere with emphasis on ozone in the Arctic region. It uses the solar occultation technique to make measurements in a highly inclined (74 degrees), low-Earth orbit (650 km) and covers tropical, mid-latitude, and polar regions [145]. It performs about 11,000 solar occultations per year [146] [147]. The spectra produced in solar occultation mode

are inverted to provide vertical profiles of temperature, pressure and the volume mixing ratios of a large number of trace gases [148] [149]. The vertical resolution achieved is 3 to 5 km. ACE FTS was designed for a two-year mission, but it has proved to be very reliable, with a lifetime of at least seven times greater than its original design requirement. Today, it is still operational with nearly full functionality.

2.8.1.2. TANSO GOSAT

The Thermal and Near Infrared Sensor – Fourier Transform Spectrometer (TANSO – FTS) is a carbon-observing sounder onboard the Japanese Greenhouse gases Observing Satellite (GOSAT) launched on January 23, 2009 [150] [151] [152]. It has three narrow spectral bands ranging from 0.758 – 0.775, 1.56 – 1.72, 1.92 – 2.08, and a wide spectral band from 5.56 to 14.3 µm with spectral sampling of 0.2 cm^{-1} [150] [151] [152]. A band centred at 1.6 µm and 2.0 µm provides column-averaged concentration information for X_{CO2} and X_{CH4} when coupled with measurements from the O_2–A band (0.76 um). The instrument schematic is shown in Figure 20.

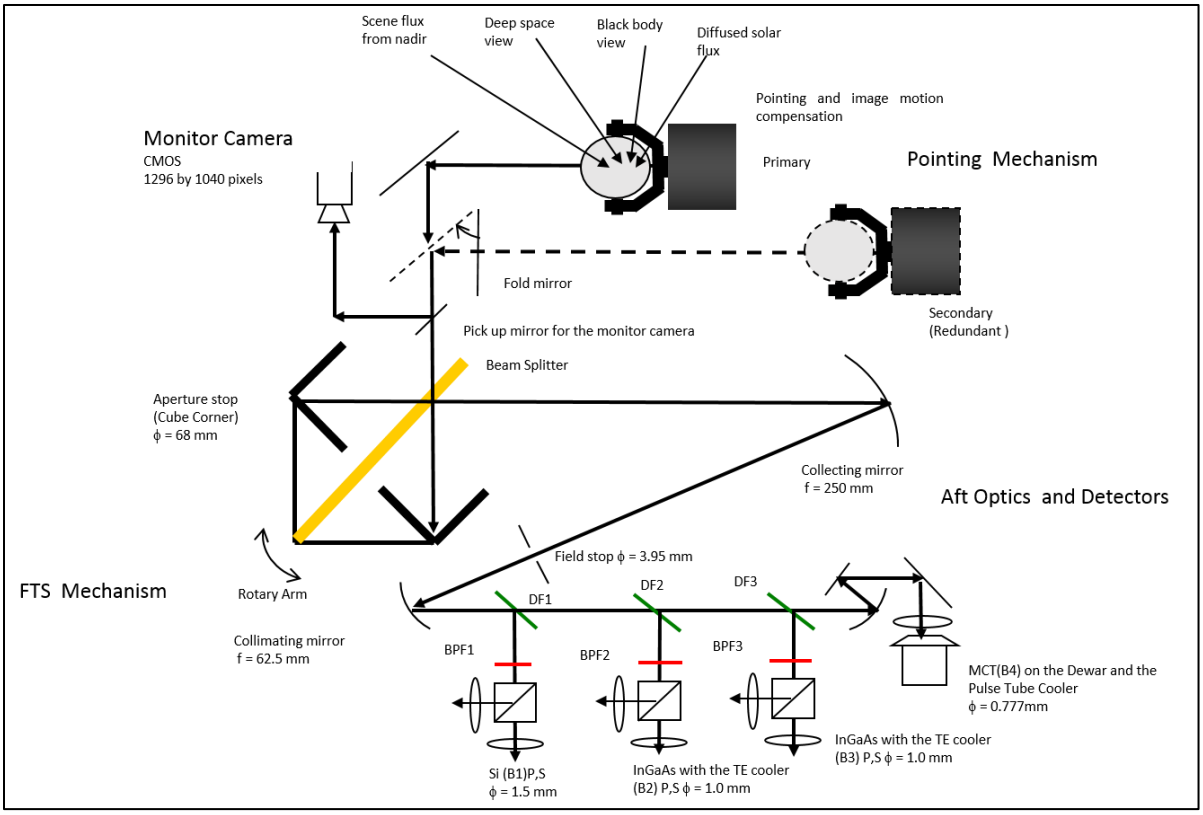

Figure 20: Schematic layout of the TANSO-FTS optical system [155]

TANSO is a double pendulum type interferometer with an optical path difference (OPD) of ±2.5 cm. A Zn-Se beam splitter is used along with two corner cubes mounted on the ends of the rotary arm. A double-sided interferogram is collected and phase corrected during data analysis [153]. One Si, two InGaAs, and one HgCdTe (mercury cadmium telluride, MCT) detectors are used to acquire the data [154]. Redundant thermo-electric-cooled (TEC) DFB lasers with tested lifetimes of 10 years are used in the sampling system. The Thermal Infrared (TIR) band is sampled at intervals of one full wavelength of 1310 nm, acquiring 38, 168 data points in one interferogram whereas Visible (Vis) and Shortwave Infrared (SWIR) bands are sampled at half-wavelengths acquiring 76, 366 sample points in one interferogram. A narrow bandpass filter is used along with mathematical processing to improve the signal-to-noise ratio.

The instrument is mounted on the Earth-facing plane of the satellite with the attitude control system operating in such a way that it is always pointing in the nadir direction. Along with this, a two-axis pointing system is used to point and compensate for image motion for cross–track (CT) and along–track (AT) directions. The CT stepper motor allows the instrument to look at the Earth's surface, deep space, a black body, and a diffuser. The motion of the pointing mechanism is synchronized with the FTS mechanism to lock and stare at the same spatial patch until the interferometer's scan ends. The rotary turn-around time for the FTS mechanism takes between 0.3 to 0.65 seconds during which the AT and CT motors are actuated and settled down.

Over the years in orbit, several irregularities have been found which disrupts the nominal operations of the instrument. ZPD shift due to loss of counts of fringes and micro-vibrations inducing a "rocking" behaviour of the FTS scanning arm are the major ones.

2.8.1.3. York-IFTS

York IFTS is designed using similar optomechanical technology as that of ACE-FTS and TANSO-FTS. It uses bigger detectors with more pixels which introduce complexity in the system which requires improved control of the moving mirror, more computational power, a better data handling system and stringent calibration methods. Table 1 shows a comparative analysis of ACE-FTS, TANSO-FTS, and York FTS. Chapter 3 discusses the attributes mentioned in Table 1 in more detail.

Table 1: Comparative analysis of ACE-FTS, TANSO-FTS, and York-IFTS

Name	ACE-FTS	TANSO-FTS	York IFTS
TRL	9	9	4
Launch date	August 12, 2003	January 23, 2009	N/A
Spacecraft	SCISAT - 1	GOSAT	N/A
Atmospheric chemicals	CH_4, CO_2, and many more	CH_4, CO_2, O_2 – A, H_2O	CH_4, CO_2, O_2 - A
Input aperture diameter	100 mm	68 mm	50 mm
Angular field of view (AFOV)	1.25 mrad	15.8 mrad	0.34 mrad
Wavelength range	2.2. to 13.3 um	0.758 – 0.775, 1.56 – 1.72, 1.92 – 2.08, 5.56 - 4.3 um	0.755 – 0.765, 1.550 – 1.640 um
Optical path difference	25 cm	5 cm	2 cm
Spectral resolution	0.02 cm^{-1}	0.2 cm^{-1}	0.5 cm^{-1}
Spatial resolution	4 km (vertical)	10.5 km	10.5 km
Scan time	2 seconds	4.0, 2.0, or 1.1 seconds	633 (at 100 Hz speed) or 65 seconds (at 500 Hz speed).
Detector elements (pixels)	1, 1	1, 1, 1, 1	320 X 256, 320 X 256

2.8.2. Advantages/disadvantages of IFTS

This section discusses the characteristics of three major kinds of spectrometers, dispersive, Fabry-Perot, and FTS (Michelson) and compares the advantages of each.

2.8.2.1. FTS v. dispersive and filter spectrometers

In a dispersive spectrometer, the spectrum is generated by optically dispersing the incoming radiation passing through a narrow slit into its wavelength or spectral components. Figure 21 shows a schematic of a dispersive spectrometer.

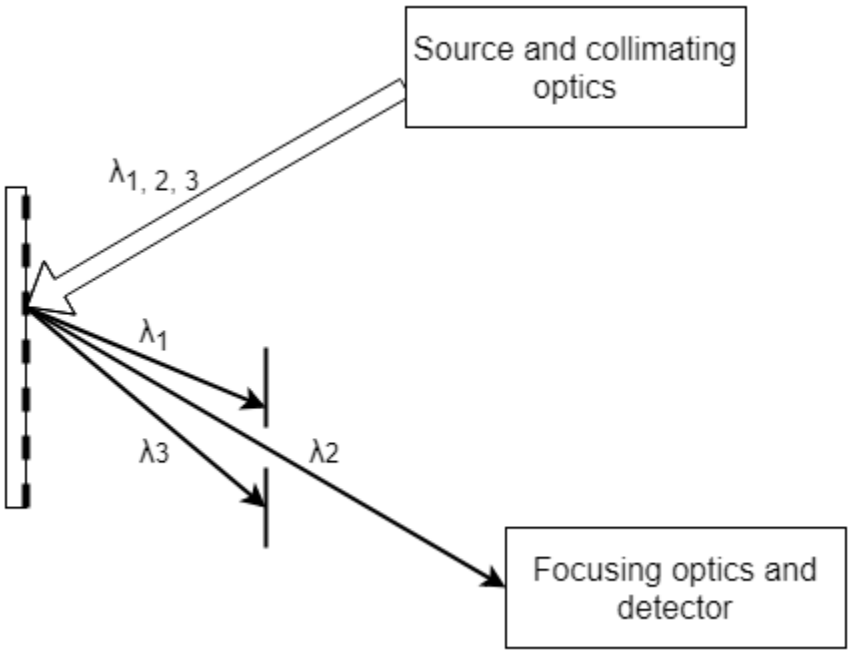

Figure 21: Illustrating the basic functionality of a dispersive spectrometer [156]

The light from the source passes through a narrow entrance slit and gets dispersed into constituent wavelengths upon interacting with a diffraction grating. Each wavelength gets directed into a unique angle and an output slit is used to select a particular wavelength which gets recorded by a detector.

The width of the slit is a trade-off for the spectral resolution, which means to get a higher spectral resolution a narrow slit is required. But this reduces the Signal to Noise Ratio (SNR) since less radiation is being detected. In an IFTS, the aperture can be large for the same resolving power and similar instrument size, providing a higher energy-gathering capability. This advantage is called the Jaquinot or throughput advantage [185]. Comparing with a similar-sized dispersive spectrometer and of the same resolving power, an FTS can provide more than ~60

times (20 x π) higher energy gathering capability [157]. This phenomenon is highly important if the radiation source is weak.

In an infrared detector, the dominant source of noise is generated within the detector itself [158]. In a dispersive spectrometer, the successive frequencies are recorded sequentially whereas FTS records all the frequencies simultaneously [159]. This improves the SNR of FTS by a factor of $N^{0.5}$ as compared to a dispersive spectrometer, where N is the number of spectral elements [158]. This superiority is known as Multiplex or Felgett advantage.

On the other hand, in an imaging detector with multiple pixels, the read-out time and integration time can increase the net time for the total scan. Therefore, for a nadir-looking instrument from space, an additional "lock-and-stare" system is required to point at the scene, at least for the duration of the total scan. In addition, it generates a tremendous amount of data since each spectral element in an interferogram is a multi-byte image. To save this data, relatively large disk spaces are required. Similarly, to process the generated data, a huge amount of computational capability is required since performing Fourier transform is quite intensive.

2.8.2.2. FTS v. Fabry Perot spectrometers

A Fabry Perot (FP) interferometer produces interference fringes by utilizing the multiple reflections between two closely spaced partially reflecting surfaces [160]. Figure 22 illustrates the operation of a Fabry-Perot spectrometer.

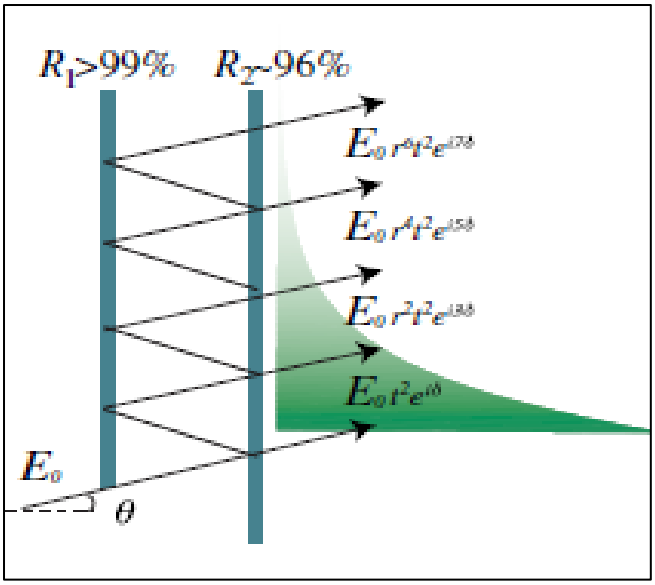

Figure 22: Illustrating basic operations of a Fabry Perot interferometer [161]

Two parallel plates coated with a high reflectivity material (R_1~99.9%) on their inner surfaces internally reflect the incident beam [161]. This results in multiple-beam interference within the cavity which is the reason why this interferometer is used for high-resolution spectral observations. The spectral pattern acquired on the detector (CCD) is achieved by spatially scanning the FP, which consists of varying the gap of the etalon in incremental steps throughout the entire spectral range [161].

The spectral space in which the wavelengths from a polychromatic source are distributed is called the free spectral range (FSR). Different spectral lines in an FSR may have different orders, making the interpretation of the spectrum complicated [158]. The generic design of an FP does not provide any wavelength multiplexing. Mechanical scanning is essential to cover a broad spectral range. In an FTS, the spectral resolution can be adjusted since it is dictated by the choice of maximum optical path difference, but this is not feasible since in a traditional FP which does not have any mechanism to change the optical path difference between the two

mirrors. The instrument response function of an FP has broad wings which can be undesirable when analyzing a rich spectrum. The wide spectral bandwidth in an FTS contributes to additional photon noise in a background-limited regime, which is the main disadvantage as compared to an FP. In an FP, the light beams have a common optical path leading to interference as opposed to an FTS, where the input light gets split by a beam splitter and has a non-common optical path structure. This makes an FTS more prone to environmental disturbances [184]. An FP also has a simpler optical design and can achieve high spectral resolving power with a compact design.

CHAPTER 3

3.0. YORK IFTS

This chapter describes the York IFTS instrument including the interaction amongst sub-systems and with the passive scene acting as the object plane. York IFTS is a passive remote sensing system. Its modular design is built for the near-infrared (NIR) wavelength region. A critical part of mission analysis and design is presented to understand and recognize the integration of the overall system. After the determination of appropriate subsystems for the established design, the resources and requirements are allocated to IFTS sub-systems.

3.1. Instrument package overview (Instrument operations concept)

The York IFTS is composed of an interferometer core along with fore-optics and aft-optics. The core [163] of the instrument, which was bought from ABB, Inc. is shown in Figure 23. The design of this instrument is based on a classical Michelson interferometer except that it uses two moving corner cube mirrors as opposed to one stationary and one moving plain mirror [163].

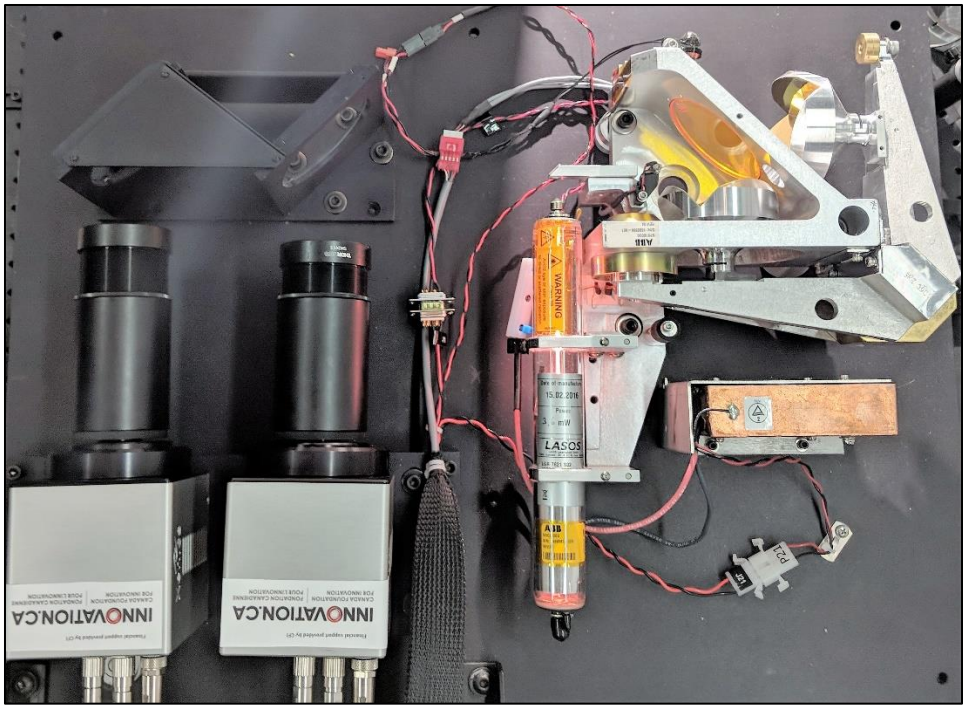

Figure 23: Opto-mechanical assembly of York IFTS

After passing through some optics, the science beam is input into the modulator where it hits the ZnSe (Zinc Selenide) beam splitter secured to the main body. The input beam encounters the beam splitter at an angle of 45 degrees to the direction of propagation. Like ACE-FTS [130] [143], a full disk of ZnSe (Zinc Selenide) is used as the beam splitter and compensator. The disc provides good flatness and precise mounting to the main body of the modulator. The beam splitter splits this light into two roughly equal amplitudes which then travel an equal distance at the rest position of the 'pendulum mirror assembly'. The retro-reflectors used are corner cubes which consist of three mutually perpendicular gold-plated mirrors making the total diameter of each corner cube 50 mm. The corner cube provides a geometrical advantage by passing the beam twice within itself, making reflected light exactly parallel to the incoming beam [126]. The retro-reflectors are moved continuously during a scan at a precisely controlled speed by varying

the voltage supply to a voice coil motor. This creates an optical path difference between the beams and produces an intensity modulation. The net physical movement of retro-reflectors is ±0.5 cm with respect to the rest position, creating a maximum optical path difference of 2 cm. The motion of a plane mirror with respect to a fixed mirror in travelling 1 cm gives a resolution of 0.5 cm^{-1}. If it travels the same distance on the other side, a double sided interferogram is produced. Because one corer cube moves in and one moves out, the path difference is 1 cm and the resolution is 1/ (2 * 1.0) = 0.5 cm^{-1}. The beams are combined again at the ZnSe beam splitter. The combined beam travels to a dichroic beam splitter which is installed at 45 degrees to the incoming beam and splits the fringes produced into two different detector channels. The beam in the vicinity of 762 nm spectral band is reflected in the normal to the incoming direction and the rest is transmitted through. The transmitted beam is reflected in the normal to incoming direction with a plane mirror also installed at 45 degrees to the incoming beam. These fringes in two channels are focused onto an InGaAs imaging detector by using an f/2 focusing lens. Table 2 outlines the design parameters.

Table 2: Design parameters of IFTS.

Type	Range with units
Spectral range (proposed)	Channel 1: 12315 cm^{-1} - 14044 cm^{-1} (100 nm) Channel 2: 5882 cm^{-1} - 6250 cm^{-1} (100 nm)
Spectral resolution	0.5 cm^{-1}
Focal plane array	320 X 256
Size of detector element (pitch)	30 µm X 30 µm

Figure 24 uses a boxes-and-lines diagram to identify the components, describes the control and the data flow between them, and states for each of them the functions to be performed, data

input, data output, and resource utilization. Rectangular boxes signify the physical subsystems while arrows connecting them show the interacting events between them.

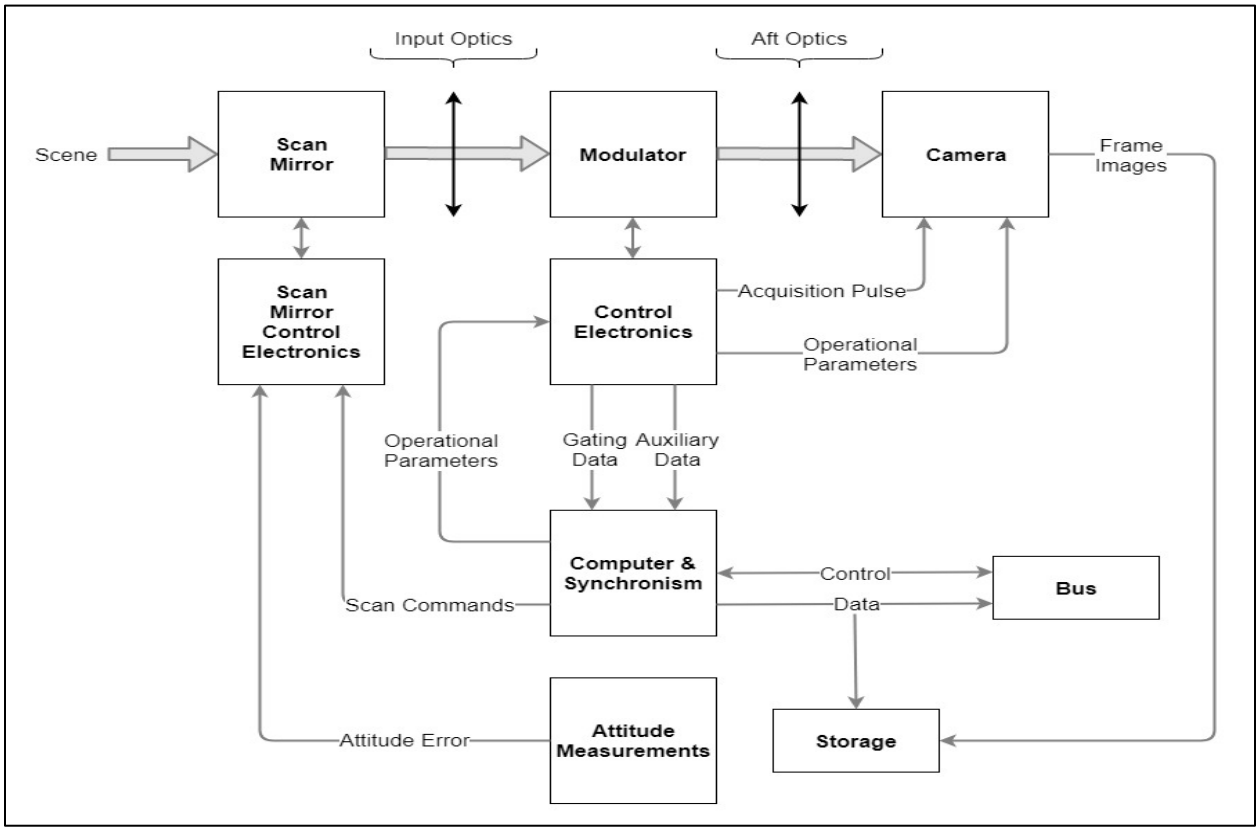

Figure 24: Operations concept for York IFTS

- The input scene is fed into the modulator through the scan mirror and input optics. The operation of the scanning mirror is outside the scope of this thesis.

- The control electronics consists of a microcontroller along with some electronic components used to send external triggers to the detectors. For the channel centred at 762 nm, the trigger is sent at every edge of the FR signal of the metrology signal (refer to section 3.6.1). For the 1600 nm channel, the trigger is sent at every positive edge of the FR signal. This way, a space sampled interferogram is generated, in which each data point is acquired at the same, constant increments in mirror position.

- The acquired images are saved on storage available onboard computers.

- The operational parameters at which the camera runs, such as the integration time and pixel window, and the operational parameters at which the modulator runs (speed, resolution) are user-controlled and are put in as a set of setup commands. These

commands are fed into the system using an individual computer and acts as the sole point of contact between the user and the IFTS.

- The camera acquires observational data in the form of raw sensor data (pixel values) which is stored in onboard memory after digitization whereas the data provided by the microcontroller to allow full interpretation and evaluation of observational data is considered auxiliary data.

3.2. ABB modulator

This section outlines the major components of the modulator including the actuator, metrology laser and its working, and white light source. Figure 25 shows a top view of the modulator.

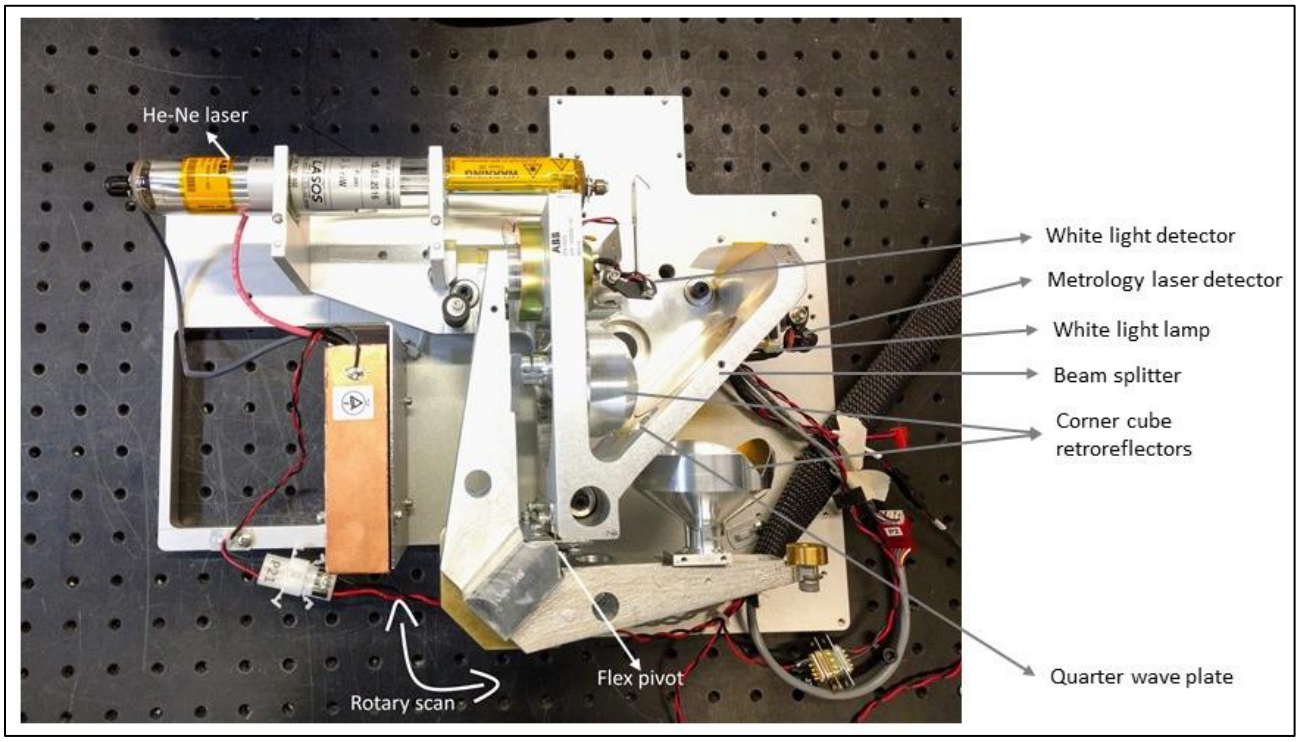

Figure 25: Snapshot of a modulator of York IFTS.

3.2.1. Actuator

An electromagnetic actuator, called a voice-coil motor, is used to precisely control the motion of the arm. The primary function of the actuator is to convert the electrical energy provided by the ACU into mechanical energy. A permanent magnet and a coil winding are used by the actuator to produce the force which is proportional to the current provided to the coil. Section 2.5 discusses the effect of maximum travel of net mirror movement on the spectral resolution of the system. Unlike modulators in ACE-FTS as discussed in section 2.8.1.1, and TANSO-FTS explained in section 2.8.1.2 in which the analog servo operates at few kHz, the York IFTS uses a digital servo implemented in an FPGA housed in the ACU. It is driven by a high-speed clock which also dictates the rate of metrology laser's fringe signal digitization. This metrology system supports the high integration time and low readout time of the imaging detector elements.

3.2.2. Metrology

To properly produce the interferogram cube an operation called "scanning through interference pattern" is followed [132]. This is achieved by precisely positioning the moving part of the interferometer to a predetermined interference position before recording each exposure. In an ideal interferogram cube, each exposure is acquired at an equidistant OPD for which a highly precise metrology system is required to control and derive the OPD scanning. The performance of the OPD scanning system directly dictates the performance of an IFTS instrument [133]. This presents a challenge for building a high-performance IFTS system.

The York IFTS uses a HeNe laser to provide a signal for position-feedback to the motion control board housed in the ACU. The output of this position sensor is a series of pulses where the distance travelled by the arm is directly proportional to the number of pulses. When the Michelson is scanned, the laser produces continuous a sinusoidal waveform which is used to determine the relative displacement of the moving mirrors. The frequency of the zero crossing of these pulses provides information about the speed at which the mirrors are moving. The arm can move in either direction in the reference frame of the beam splitter to produce a forward and backward scan. Additional optics are needed to determine the direction of travel. Figure 26 illustrates the optics used to determine the direction of the arm.

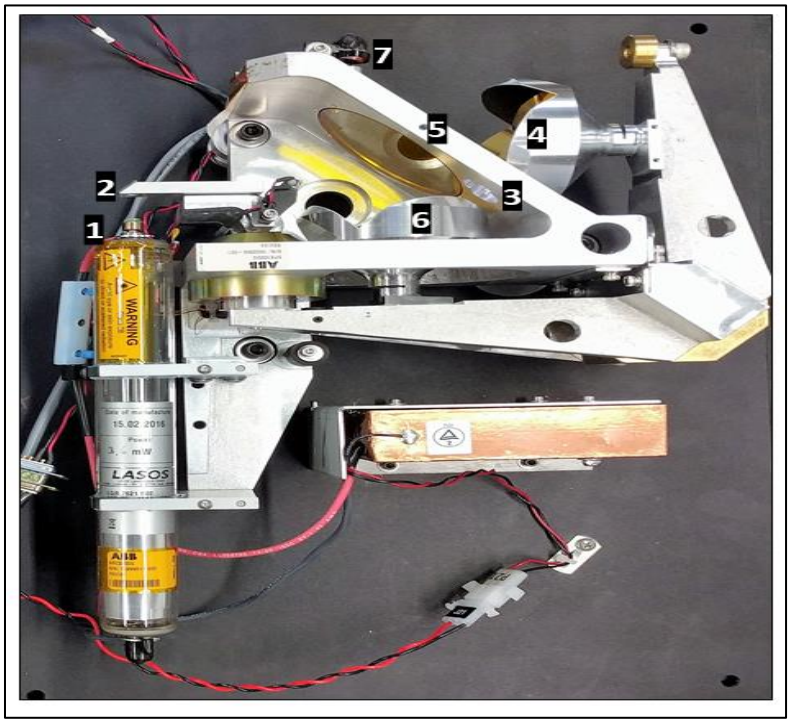

Figure 26: Illustration of optics used to determine the direction of the arm.

The cylindrical head of laser marked as “1” is rotated to 45 degrees with respect to the plane of the optical table. The linearly polarized beam emitted from this laser has two equal intensity

orthogonal polarizations one in the plane of the table and another perpendicular to it. The beam hits a plane mirror (“2”) at an incidence of 45 degrees before encountering a beam splitter which splits it into two equal parts, transmitted and reflected. The transmitted part passes through a lambda/4 retarder (a quarter wave plate, “3”) to become circularly polarized. Since the polarization axis of the incoming beam is at 45 degrees relative to the axis of the quarter wave plate, the circularly polarized light emerging out has a phase difference between the two orthogonal field components. The corner cubes (“4”, and “6”) reflect the light toward the beam splitter, which makes parts of both beams coming from corner cubes interfere at the detector (“7”). The detector is a two-channel encoder which acquires two interference patterns arising from the two phase components. Depending upon the direction of the arm, pattern 1 leads or lags pattern 2. Henceforth the direction is deduced using this phase information.

In addition to providing the motion attributes of the arm, another function of the HeNe laser position sensor is to acquire an equalled interval mirror position by providing a sampling clock signal. This clock signal is a set of repetitive digital pulses along the mirror displacement. These digital pulses are used to trigger the detectors in both channels and drive the control and acquisition software (CAS).

The metrology laser currently used is procured from Lasos Germany under the product number LGR7621S with the Doppler-broadened gain curve of 1.5 GHz, FWHM [167]. The laser is neither temperature nor current controlled and does not have any wavelength stabilizing feedback loop which results in mode-hoping of the output beam. Appendix III proves that the two consecutive modes are centred at 632.8 nm (15802.78 cm^{-1}), and 632.5 nm (15810.28 cm^{-1}) which are wider than the spectral resolution of the IFTS. Conclusively, lasers lasing at $(m+1)^{th}$

mode will be clearly differentiated by the interferometer. Mode hoping is predicted to cause abnormality in the space-sampling process and cause inconsistencies in the constant increments of mirror positioning. The accuracy of signals produced by the ACU is dependent on the consistency of power supplied by the laser detector used to produce the external triggers for the cameras.

Figure 27: Snapshot of the white light lamp.

Figure 27 shows the white light lamp with C-6 type Tungsten filament and an onboard detector which is used to detect the zero position of the arm motion. During the 'Power up' sequence of the instrument as discussed in section 4.2.1.3, the arm performs multiple scans at various speeds and resolutions. During these scans, the lamp turns on and registers the zero position of the arm motion in the built-in memory of the ACU. This registered position is required and is used to successfully create a double-sided interferogram.

3.2.3. Modulator arm vibration

Due to the generic structure of the modulator, it is extremely susceptible to any ground vibrations. Operating the modulator on a heavy optical table [165] shows significant noise in

the metrology signal near the speed of the moving arm quantified in the units of fringes per second. The behaviour persists at all different speeds i.e. 6000, 3001, 500, 200, 150, and 100 fringes per second. On the contrary, the signal shows a significantly quieter behaviour when the modulator is operated while being placed on an air isolated optical table. The contrast between both the results shows the sensitivity of the instrument to the ground vibrations. Also, at higher run speeds, the arm has better performance and does not show much noise. This behaviour is expected to arise from greater dynamic inertia in the arm at higher speeds. The unwanted secondary noise levels in the signal are characterized by analyzing the Fast Fourier Transform (FFT) of the metrology signal. Figure 28 and Figure 29 represents the arithmetic mean of 10 data samples of FFT data taken in both environments that is without an air isolation optical table and with the air isolation optical table.

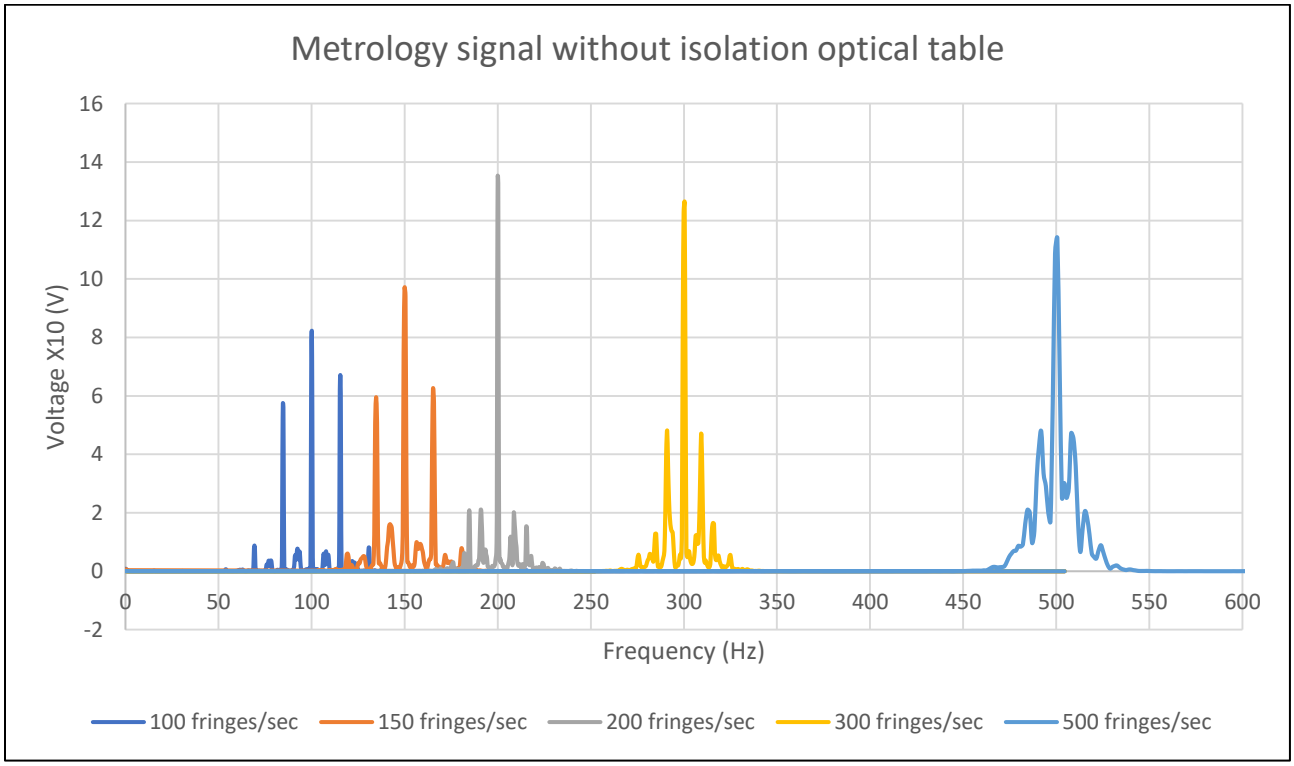

Figure 28: Metrology signal at different speeds without isolation

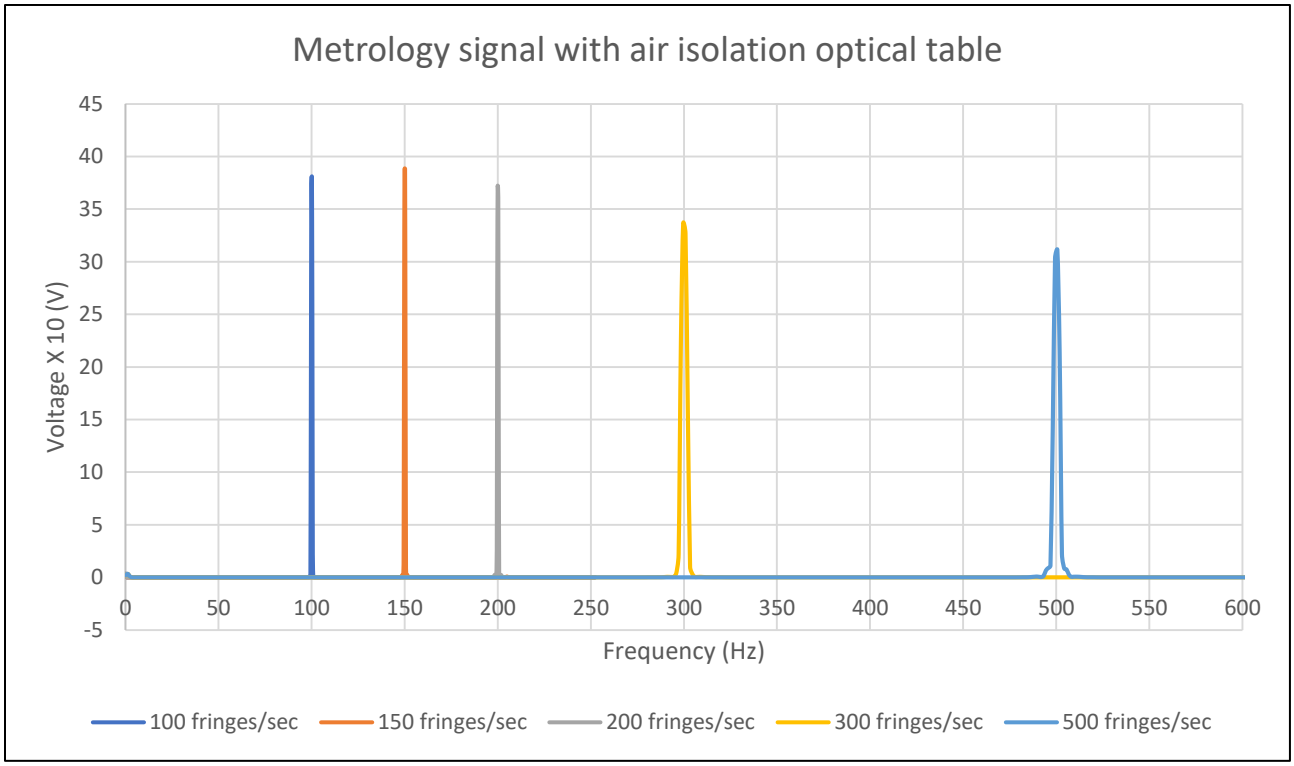

Figure 29: Metrology signal at different speeds with isolation

However, using an optical table that uses air for isolation does not align with the goal of developing design elements to make the payload space operable. Rather a passive isolator is required. Major requirements of the isolator include high damping capabilities to reduce the resonant response of the system, low stiffness and isolation in all six degrees of freedom (three translational and three rotational). According to the weight and performance requirements, the 100BM-10 model of benchtop vibration isolator platform by Minus-K [166] suits the experiment. The typical transmissivity curves are shown in Figure 30.

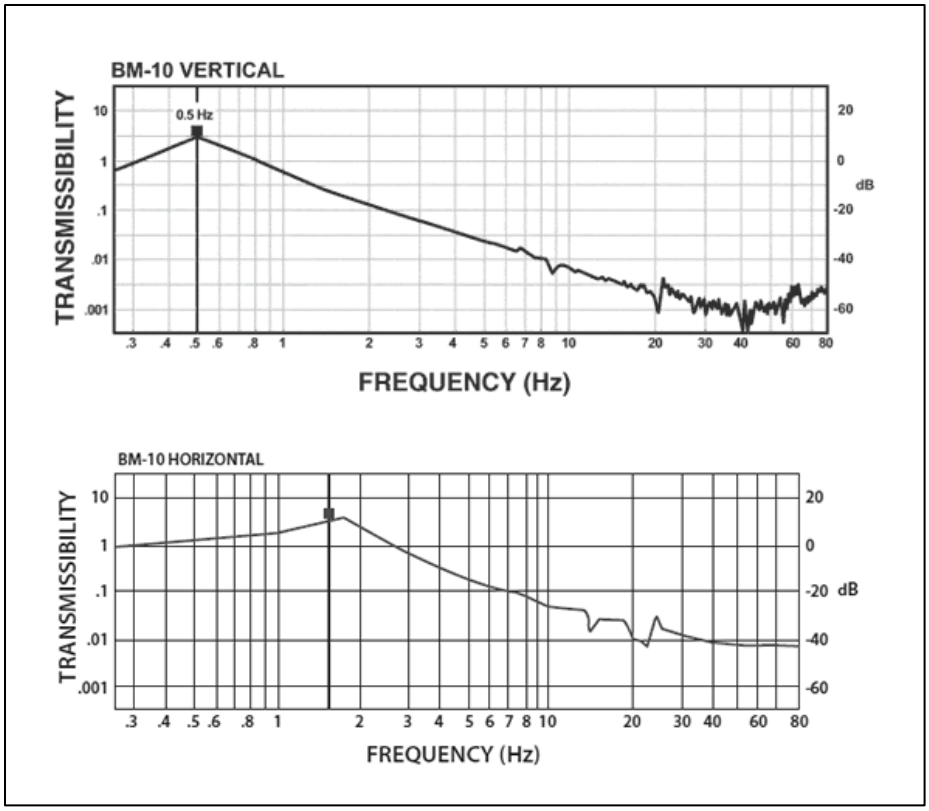

Figure 30: Typical transmissivity curve of Minus-K passive vibration isolator [119]

These curves show a vertical natural frequency of 0.5 Hz and horizontal natural frequency of 1.5 Hz. In addition, a very small transmission at low frequencies is to be expected. Figure 31 shows the arithmetic mean of 10 data samples of metrology signal FFT with the complete interferometer sitting on the isolator.

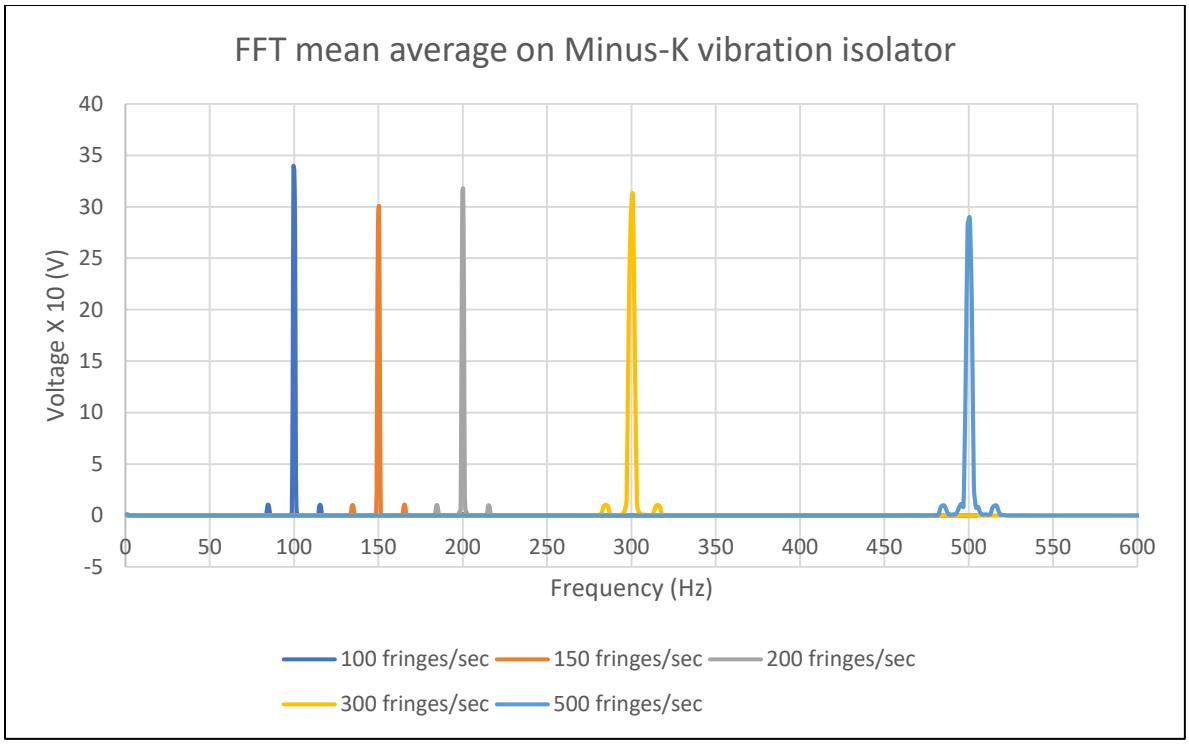

Figure 31: FFT mean average with Minus-K isolator.

The above plot demonstrates two noise peaks at an operational frequency of ±15 Hz. This is believed to arise due to the weight and structural design of the arm.

3.3. Focusing lens

The modulated light is collected on the photo-sensor with a focusing lens (f/2). A telecentric design is adopted in which the chief ray at each image field is parallel to the optical axis. The resolution and swath are dictated by focal length, pixel size and the number of elements in the detector.

The imaging detector used has a pixel pitch of 30 μm. This constraint sets a requirement of the focused spot size of 30 μm or better. Model AL-50100 of Thorlabs, Inc. was studied by simulating it in Zemax optical studio version 16.5 and complies with the requirements. The

aspheric lens is an f/2 system with a focal length of about 100 mm at the wavelength of 780 nm and a diameter of 50.0 mm is shown in Figure 32. The curved surface of the lens faces the object plane whereas the plane side is towards the side of the image plane.

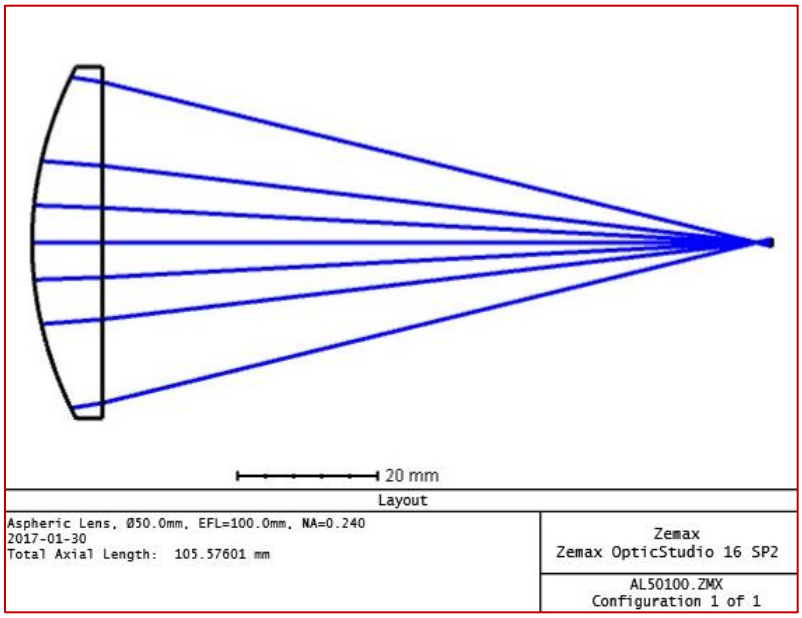

Figure 32: Illustrating the 2D simulation of the aspheric focusing lens.

Figure 33 shows the results of simulations on the lens with the primary wavelength of 0.762 µm and object being at infinity gives results of 1.959 µm of airy disk radius with an effective focal length measure of 99.9279 mm.

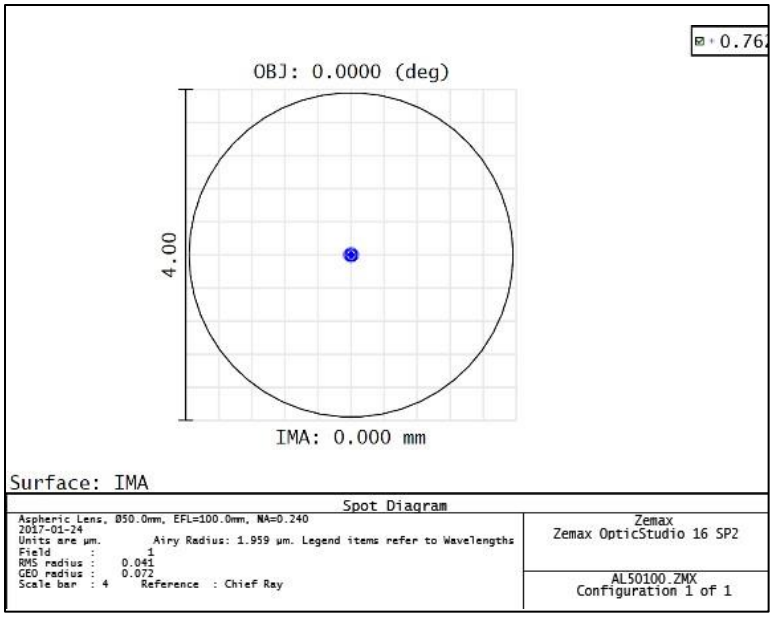

Figure 33: Spot diagram with a primary wavelength of 762 nm. The airy disk has a radius of 1.959 um.

Similarly, with 1.6 µm wavelength as primary and object at infinity, results in an airy disk of 4.207 µm with effective focal length of 102.236 mm.

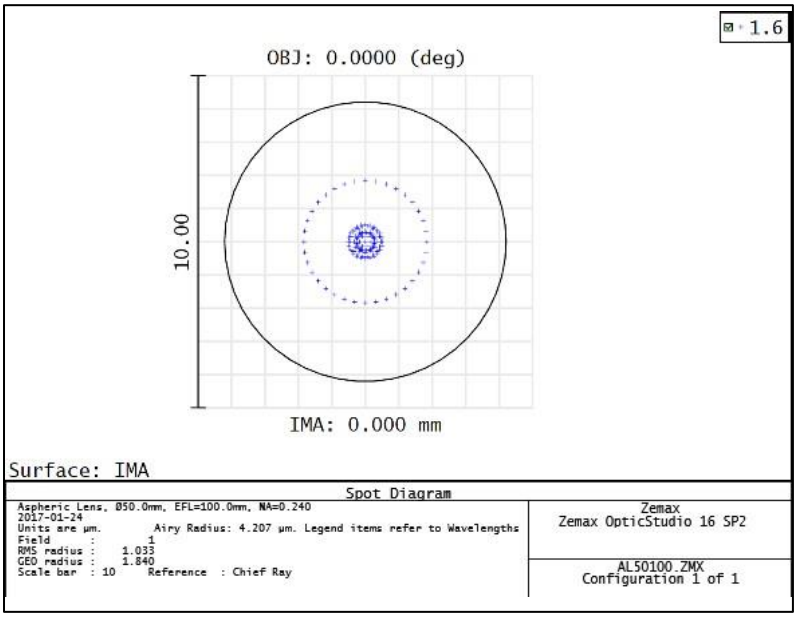

Figure 34: Spot diagram with a primary wavelength of 1600 nm. The airy disk has a radius of 4.207 um.

The airy disks produced in the Figure 33, and Figure 34 represents the focused spot produced by circular diffraction. The central and side lobs contain 84% an 16% of the total focused energy respectively [120]. Since the lens used is aspheric, it corrects for any spherical aberrations which are an inherent property of spherical lenses [169]. It prevents the incident light rays from focusing at different points when forming an image thereby reducing the blur.

3.4. Bandpass filter

The modulated beam is split by a dichroic filter. The split beams propagate in the direction of their respective detectors. The detectors have individual lenses equipped with a bandpass filter. The bandpass filter is an interference filter and defines the spectral window of each channel. The bandpass filter function selectively transmits a narrow range of wavelengths from the continuum source of radiation. Figure 35 shows the bandpass filter function for the O_2-A channel filter centred at 760 nm with a bandwidth of about 10 nm.

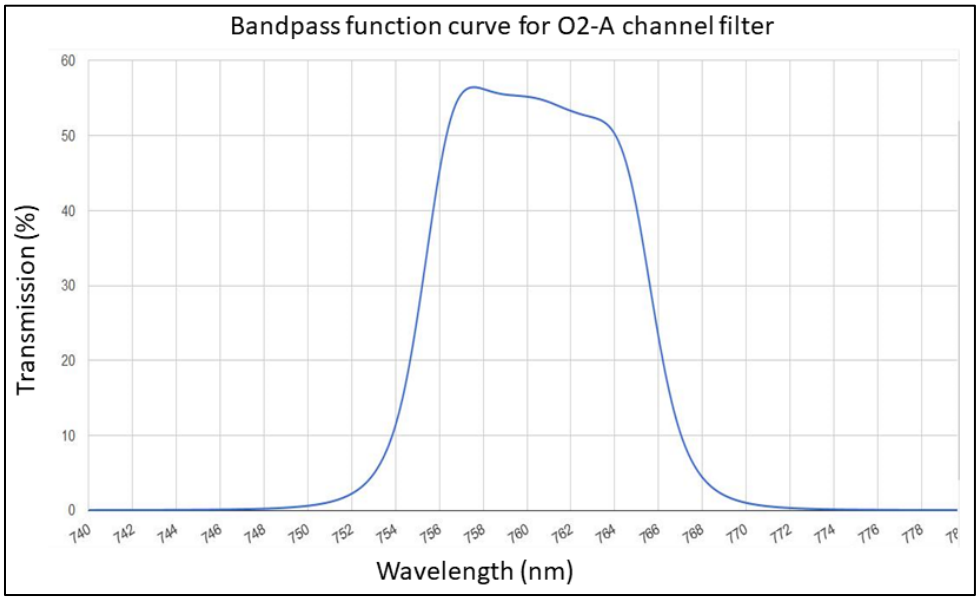

Figure 35: The bandpass filter function for the O2-A filter. It is centred at 760 nm with a bandwidth of about 10 nm.

Figure 36 shows the bandpass filter function for the CH_4 and CO_2 channel centred at 1575 nm with a bandwidth of about 75 nm.

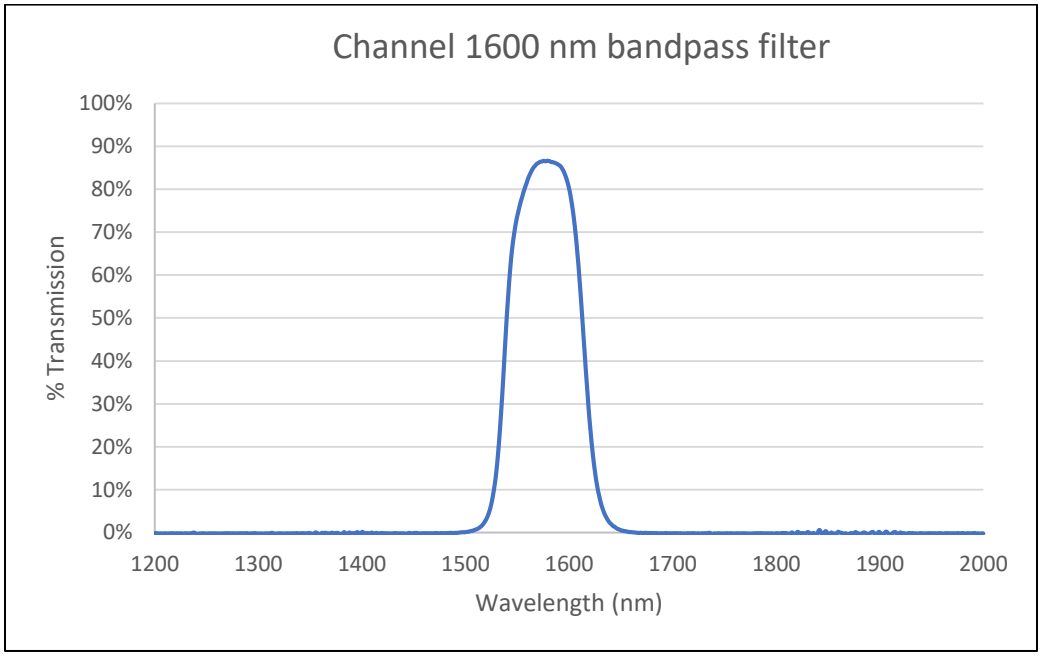

Figure 36: Bandpass filter function for the CH_4 and CO_2 channel filter. It is centred at 1575 nm with a bandwidth of about 75 nm.

3.5. Detector

The imaging sensor used is a large, multiplexed two-dimensional (2D) detector array. This Focal Plane Array (FPA) is the optical element that defines the spatial resolution, sensitivity and image quality of the York IFTS system. To define the requirements for selecting the detector, the overall mission requirements and science-driven constraints on the performance of the electro-optical system are considered. These requirements can be divided into four categories: sensitivity, spatial resolution, wavelength range, and temporal system [170].

The detector has individual light sensitive elements called pixels. These pixels are arranged in rows and columns, hence the 2D array. These pixels are formed on an Indium Gallium Arsenide (InGaAs) wafer. Various attributes of the sensor are listed in Table 3.

Table 3: Attributes of the detector.

Serial number	Attribute	Value
1.	Lens adapter	C-mount
2.	Pixel Pitch (square edge)	30 µm
3.	Number of pixels	320 X 256
4.	Size of active area	(320*30 µm) * (256*30 µm) = 9.6 mm X 7.68 mm = 73.7 mm^2
5.	Composition material	InGaAs
6.	Computer interface	USB 2.0
7.	Maximum frame rate	100 fps

The frame rate of the camera is limited by the USB 2.0 interface. With a different interface such as a camera link, a similar camera can reach 200 to 350 frames per second. The detector used in York IFTS is a customized Xenics Xeva which has a wide range of spectral responsivity as shown in Figure 37.

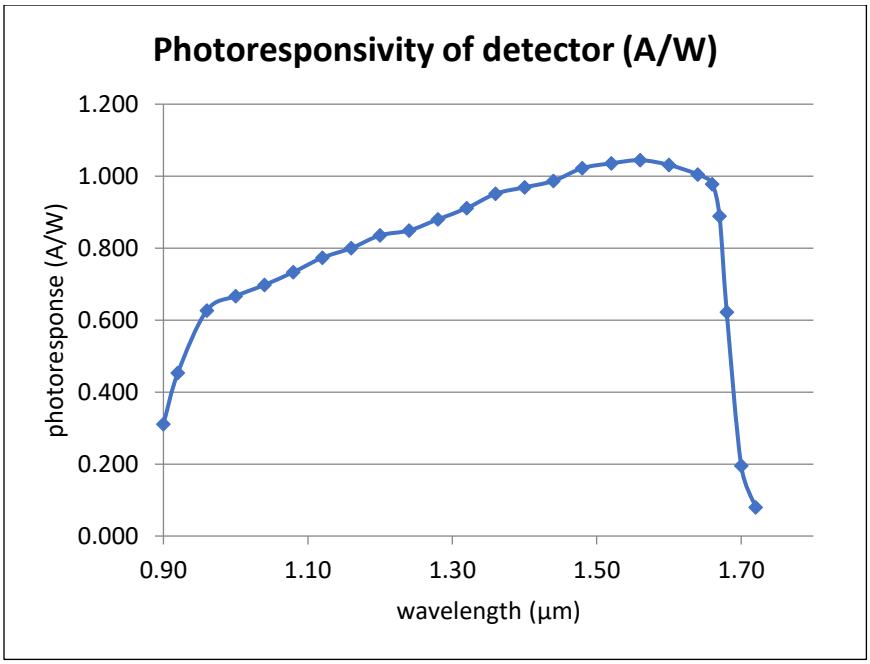

Figure 37: Photo responsivity of detector [186]

It has three connection ports for power, data-link, and an external trigger respectively. A wall-mount adapter type power supply is used to supply 12 V and a maximum of 5.42 A. A USB 2.0 connector is used as the data link between the camera and a computer. The camera can be run in continuous mode where each image is taken after a set time interval or in external trigger mode in which images are taken upon receiving of an electronic trigger pulse of voltage 4.5 – 5.5 V. For this project, the external trigger mode is used in which the triggers are sent as defined by the CAS. The images hence acquired are saved on a PC in a pre-set defined format by CAS as described in section 4.2.4.

It is observed that the camera drops some frames while capturing the images during the scan. Table 4 shows that the number of external triggers sent by the microcontroller is often greater than the net number of frames acquired, especially at higher external rate or frame rate. The frame drop introduces the missing data points in the interferogram. An algorithm was created

as a part of the control and acquisition software to find and flag the missing frames so that during post analysis, appropriate techniques can be applied to reconstruct the data.

Table 4: Frame drop table for operating detector at various speeds.

External trigger frequency	Triggers sent by uController	Number of images taken by the camera	Difference µController - Camera
100 Hz	65474	65473	1
200 Hz	65474	65439	35
300 Hz	65470	65416	54
400 Hz	65470	65411	59
500 Hz	65470	65408	62

As discussed in section 3.2.3, to make the modulator more immune to the physical vibrations coming from the ground and other sources, the arm should be run at higher speeds. In-turn to acquire the data at the same rate, the cameras need to increase their capture rate by the same factor.

3.6. System architecture

A block diagram depicting the framework to guide the development of the IFTS system is shown in Figure 38. After performing various trade studies, the following hardware architecture and interfaces were adopted. More components can be added later to increase redundancy in the system. The interconnections between the various subsystems and components are highlighted.

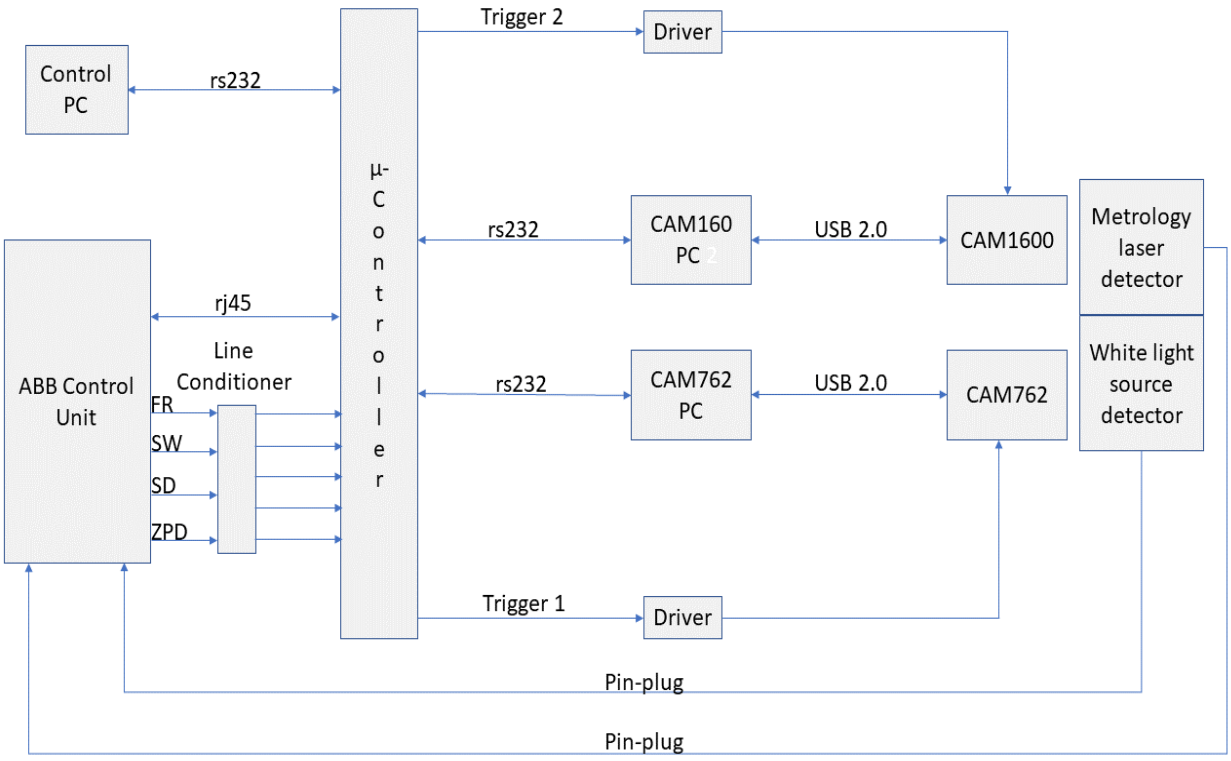

Figure 38: Payload hardware architecture and interfaces.

- The payload has two channels centred at around 762 nm and 1600 nm respectively. Each individual channel consists of a computer (CAM1600PC and CAM762 PC), a detector (CAM1600 and CAM762) and a trigger driver.

- A micro-controller on board acts as the payload master which is responsible for controlling all operations.

- A control computer (Control PC) acts as payload sub-master which is used to command the microcontroller and to control the operation of modulator arm i.e., speed and extent of motion of the modulator arm.

- The ABB Control Unit (ACU) provides power to the modulator components which includes the white light source, metrology laser, and the actuator.

- The signal from the white light source and metrology laser detector mounted on the modulator assembly are intercepted by ACU using a pin-plug connector.

- The microcontroller transmits and receives command signals and data via an RS232 interface. This includes talking to the Control PC and to both data channel computers.

- The voltage signals from the ACU to the microcontroller are connected via a BNC interface.

- The signals from the ACU are conditioned using a Schmitt trigger to stabilize the signal by suppressing any noise. A level shifter is used to bring the signal to voltage levels which are within the acceptance range of the microcontroller.

- The microcontroller and ACU interact over an Ethernet interface.

- Both data channel PCs are connected to their respective cameras using a USB 2.0 interface.

- The signal from the microcontroller is conditioned by a voltage driver to make it suitable to interface to the camera.

- The microcontroller acts as a communication link between the camera PCs and Control PCs.

List of hardware interfaces along with mass and power budget is given in Appendix IV, V, and VI.

3.6.1. ACU signals characterization

The ABB control unit houses electronic modules which provide power to the optomechanical assembly and signals for external detectors to monitor the interferometer state. The ACU outputs 5 digital and 2 analog signals i.e., 7 signals in total, through the BNC connectors connected to the back panel of the rack-mount box. These signals are named as Fringe analog (FRA), Dephase analog (FR90A), Fringe digital (FR), Dephase digital (FR90), Sampling Window (SW), Zero Path Difference (ZPD), and Scan Direction (SD). For the current development phase of the project, only 4 digital signals are used and FRA, FR90A, and FR90 are unconnected. Figure 39 shows the nature of these signals [175].

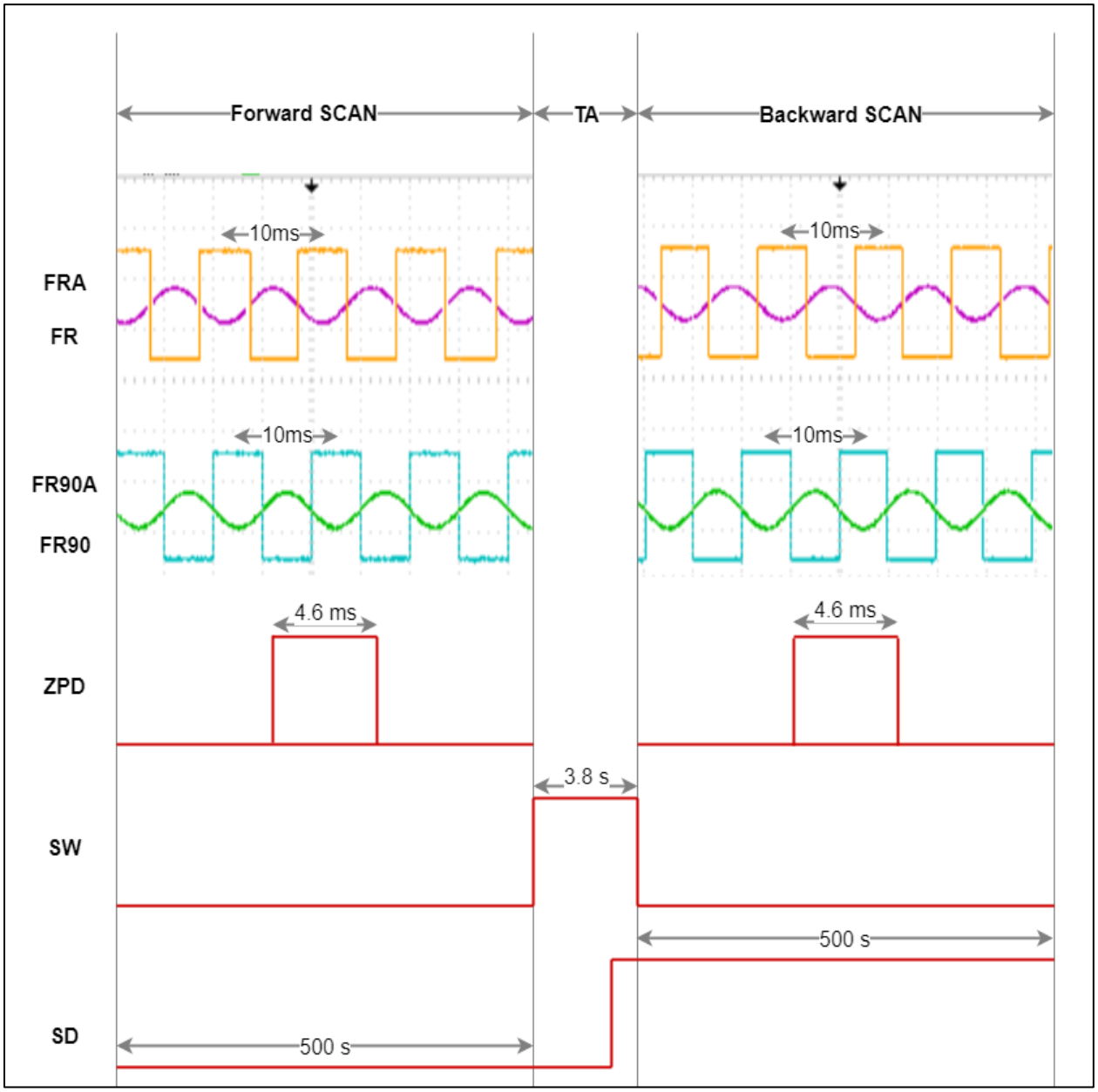

Figure 39: ABB Control Unit output signals.

- Fringe Analog (FRA) is the perfect sinusoidal signal produced by the metrology laser interacting with the modulator.

- The analog Dephase signal (also called FR90A) is produced in the same way as of the Fringe analog (FRA) except that one beam is travelling through a quarter wave plate. This induces a phase difference of ~pi/2 in the Dephase signal as compared to the Fringe

signal. In Figure 39, the fringe digital signal (FR) is shown in green and the dephase digital signal (FR90) is shown in teal.

- The digital Fringe and Dephase signals are just the digital conversion of their analog counterparts. The digital signals have a slope change at the mean value (DC level) of their analog signals.

- The Sampling Window (SW) signal is low during the motion of the arm and high during the turnaround. When the SW signal is low data can be acquired whereas when the SW signal is high, it means the arm is turning around and data cannot be acquired at that time.

- The Zero Path Difference (ZPD) signal corresponds to the central position in the motion of the arm. It is high when the arm is in the centre and low elsewhere.

- The Scan Direction (SD) signal is high during the motion of the arm in one direction and low in the other. The point of going from low SD to high SD does not lay exactly at the midpoint od the high period of the SW signal.

3.6.2. Microcontroller – Freescale

The microcontroller acts as the 'payload master'. It performs multiple functions such as allowing the user to interact with the ACU, intercepting ACU signals to produce auxiliary data, and producing external triggers for the detectors. Figure 40 shows a snapshot of the microcontroller used in York IFTS. It is commercially called the Freescale FRDM-K64F [176].

Figure 40: Snapshot of Freescale FRDM-K64F microcontroller [176]

The mini USB 2.0 interface is used to burn the program into the microcontroller and the onboard UART modules are used to communicate via an RS-232 interface with the control PC and both camera PCs. The optimized rate at which it performs the best simultaneously overall three lines is 57600 baud. The USB line is also used to input control commands to run the instrument in diagnostic mode. It has 256 KB of Random-Access Memory (RAM) which is populated with a scan report. It also has an RJ-45 connector which connects with the ACU. The pins on the latter interface accept the signals from ACU and produce external triggers for the camera. The triggers produced have a width of 20 µs.

3.7. Optical budgets

This section discusses the optical budget that complies with the high-level functional requirements and overall system configuration parameters. Detailed calculations of optical budget are listed in Appendix VII.

3.7.1. Angular field of view (AFOV) in degrees

The angular field of view is defined as the maximum angular size of the object as seen from entrance pupil of the IFTS. Figure 41 illustrates the AFOV with pixel diagonal “h” and focal length “f”.

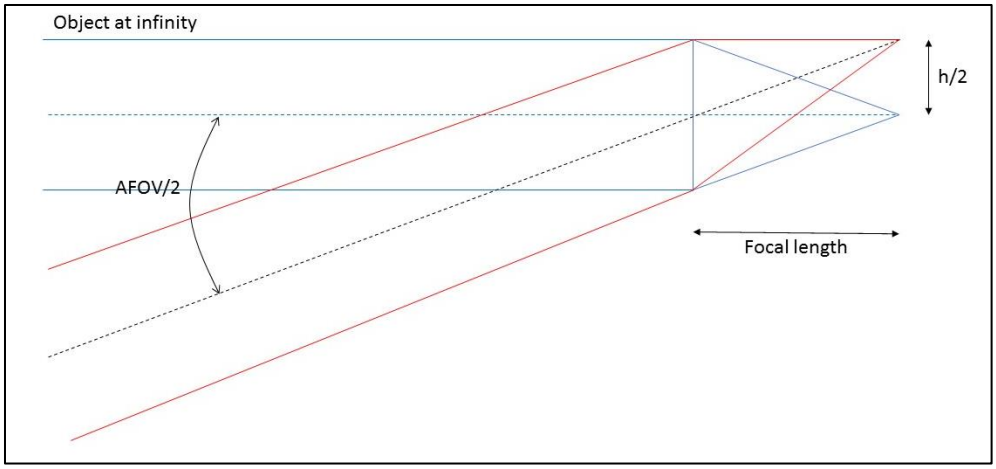

Figure 41: Angular field of view.

The 762 nm channel has an AFOV of about 2.43 X 10^{-2} degrees and 1600 nm of about 2.38 X 10^{-2} degrees.

From a stratospheric balloon at an altitude of 36 km, 762 nm channel of York IFTS has a spatial resolution of about 10.8 X 10.8 m^2 with a swath of about 3456 X 2765 m^2 using all 320 X 256 detector pixels. For the 1600 nm channel, it has a spatial resolution of about 10.6 X 10.6 m^2 with a swath of about 3392 X 2714 m^2 using all 320 X 256 detector pixels. The difference in the sizes of spatial resolution in channels is from the refractive index effect on the focal length of the focusing lens.

From a satellite at an altitude of 36,000 km, the 762 nm has a spatial resolution of about 10.8 X 10.8 km^2 with a swath of about 3456 X 2765 km^2 using all 320 X 256 detector pixels. For the 1600 nm channel, the spatial resolution is about 10.6 X 10.6 km^2 with a swath of about 3392 X 2714 km^2 using all 320 X 256 detector pixels.

3.7.2. The time required for each scan

The minimum number of images required (complying with the Nyquist frequency phenomenon) for channel 762 nm and 1600 nm are 52493 and 25000 respectively. The number of images

acquired in using the metrology laser of wavelength 632 nm is 63291. Therefore, the number of acquired images in both channels is more than the minimum Nyquist requirement of 63291. At a speed of 100 Hz, a complete scan to acquire a double-sided interferogram would take about 633 seconds.

CHAPTER 4

4.0. CONTROL AND ACQUISITION SOFTWARE

This chapter provides an overview of the entire control and data acquisition system for York IFTS. The system is explained to show how the Control and Acquisition software (CAS) interacts with the components of the York IFTS and to introduce the basic functionality. It also describes functionality available for various types of stakeholders. Finally, the constraints and assumptions underlying system are presented.

From a global viewpoint, CAS requires an input stimulus and responds by changing the state of the system. It is mathematically intensive and requires high accuracy and strict timelines. CAS also manages the entire IFTS by performing fault detection and correction. It oversees flow control and is therefore logic intensive. It manages computer resources and controls their allocation to accomplish the project's tasks. A user can input various parameters such as spectral resolution, detector window, temperature, etc. to command the operation of the system. CAS samples the metrology signal and generates triggers to control and record appropriate events. It acquires data in the form of images recorded by individual channel cameras. In post-processing, this data is plotted as a function of Optical Path Difference (OPD) to provide the interferogram and is then further Fourier transformed to produce spectra.

4.1. Control and acquisition software requirements

This section provides a detailed description of the high-level requirements for CAS, necessary to achieve science goals as described in Chapter 1. The justification of the requirements is also

provided where the rationale for the requirement is not clearly inferred from the project's needs. This section illustrates the purpose and provides complete definition for the development of the IFTS system. It also describes system constraints, interface and interactions with other external applications.

Requirements in this chapter are classified according to the following three categories:

i. "Shall" Requirements noted **R**- are mandatory, shall be verified with an accepted verification method and shall be complied with.

ii. "Should" Requirements (or Goals) noted **G**- are desirable requirements with the objective to increase the scientific return or performance of the mission. Goals may be fulfilled under limited favourable conditions.

iii. "Will" Requirements noted **W**- are the facts or declaration of the purpose.

Each requirement is identified as one of the categories mentioned in Table 5, prefaced by the R, G or W description.

Table 5: Requirement ID categories.

PRF	Performance
FUN	Functionality
USY	Usability
LGL	Logical

The third component of the ID of a requirement followed by the category is the serial number.

For example, a requirement identified as R-FUN-###, "R" signifies that it is a "shall" requirement which the system must achieve to satisfy the primary goals; "FUN" indicates it is a

functional requirement, and the last three digits "###" are serial numbers in continuation which usually proceed in increments of 10.

4.1.1. Functional requirements

This section defines the key jobs that CAS is supposed to perform to meet the project objectives. It discusses the operational parameters of the IFTS controlled by the user, scanning procedures and the method of saving and archiving the scanned data.

4.1.1.1. Allow user inputs

An important purpose of CAS is to allow the user to input various possible parameters and then run the system accordingly. Combinations of these input parameters result in different modes and behaviours of the IFTS.

Table 6 below summarizes the functional requirements. The requirements are serial numbered as explained in section 4.1.

Table 6: Performance requirements for York IFTS.

ID	Description	Rationale
R-FUN-010	CAS shall have an operational mode and a diagnostic mode.	*To use the operational mode to acquire data and the diagnostic mode to run each subsystem individually and isolate the source of an anomaly.*
R-FUN-020	Camera saturation shall be detected.	*To adjust camera properties accordingly.*
R-FUN-030	Saturated frame number shall be registered.	*To raise a flag for bad data (scattering from clouds)*
R-FUN-040	The ZPD shall always be the median of the interferogram acquisition window.	*To produce a symmetric double-sided interferogram.*
W-FUN-050	The signal from the ACU will be used to infer the arm speed.	*To derive the direct behaviour of the metrology laser's interaction with the modulator.*
R-FUN-060	CAS shall register both coarse and fine ZPD positions in the final data file.	*To adjust for discrepancies in the voice coil motor's nominal operation in post-processing.*

R-FUN-070	The number of triggers sent to each camera shall be registered in the final data file.	*To identify discrepancies in the number of images acquired.*
R-FUN-080	Length of acquisition window shall be registered.	*To derive the discrepancy behaviour of the microcontroller. If triggers generated and images acquired do not match the length of acquisition window, this implies that the microcontroller did not generate the required number of triggers.*
G-FUN-090	CAS should be robust against any noise peaks in the input signals to the microcontroller.	*To prevent the production of fake triggers to the camera.*
G-FUN-100	CAS should be robust against back paddling of the arm.	*To prevent the production of fake triggers to the camera and out of phase data points.*
G-FUN-110	CAS should be robust against the unstable motion of arm due to ground vibrations.	*The modulator arm is susceptible to ground vibrations. Refer section 3.2.3.*
G-FUN-120	The user shall be able to abort from the current scan at any time.	
G-FUN-130	The user shall be able to input the total number of required scans.	*User input is not required at the start of every scan unless a change in setup parameters is required.*
G-FUN-140	The user shall be able to adjust pixel window in camera 762	*To adjust for the object plane. Also, the maximum frame of the camera is a function of the pixel window.*
G-FUN-150	The user shall be able to adjust pixel window on camera 1600	*To adjust for the object plane. Also, the maximum frame of the camera is a function of the pixel window.*
G-FUN-160	The user shall be able to set the temperature on camera 762	*To develop an understanding of the performance (signal to noise) of an InGaAs camera which is highly dependent on the operational temperature.*
G-FUN-170	The user shall be able to set the temperature on camera 1600	*To develop an understanding of the performance (signal to noise) of an InGaAs camera which is highly dependent on the operational temperature.*
G-FUN-180	The user shall be able to adjust integration time on camera 762	*To understand the performance of IFTS at various integration times which defines the length of each frame in the time domain.* *Photon count on the camera for a certain frame is a function of integration time.* *The maximum frame rate of the camera is a function of integration time.* *Different arm speeds have variable frame lengths in the time domain.*
G-FUN-190	The user shall be able to adjust integration time on camera 1600	*To understand the performance of IFTS at various integration times which defines the length of each frame in the time domain.* *Photon count on the camera for a certain frame is a function of integration time.* *The maximum frame rate of the camera is a*

		function of integration time. *Different arm speeds have variable frame lengths in the time domain.*
G-FUN-200	The user shall be able to adjust the modulator's arm speed	*To control the photon count and the SNR.* *The speed of the modulator's arm defines the length of each frame in the time domain.*
G-FUN-210	The user shall be able to adjust the extent of arm motion.	*To control the spectral resolution which is a function of maximum path difference. Movement of arm generates the path difference in the interferometer.*

4.1.1.2. Produce sampling clock signal

A major function of the CAS is to sample the ACU signals after they are conditioned to produce the sampling clock signal. This clock signal is used to make a precisely equal and stable interval sampling for the science signal. The metrology laser beam is used as a source in the modulator to sense the relative position of the moving mirrors by counting the sinusoidal pulses of modulated signal, as explained in section 3.2.2. The laser beam passes through the same beam splitter and retro-reflectors as the science beam and is sensed by a detector mounted on the main assembly of the interferometer. This metrology laser signal is fed into the ACU, where it is electronically tuned and is output in both analog and digital forms. A line conditioner is used to filter for any noise and to adjust the amplitude of these ACU signals. These are then input to the microcontroller.

4.1.1.3. Detect zero position

When power is recycled to the ACU, the modulator performs a few scans as a function of an inbuilt routine. During these scans, the white light source is turned on and the Zero position of the arm is registered in the routine. Consequently, during scanning when the actuator reaches

this position the ZPD signal output of the ACU is increased to high voltage. The width of the ZPD signal depends on the current speed of the arm and the extent of its motion. To construct double sided interferograms and to perform post-processing on the data, the precise Zero position of the arm is required. Therefore, an essential function of the CAS is to record the zero position in the final data file.

The actuator used to move the arm is a voice coil motor, which is a coil in a magnetic housing as described in section 3.2.1. As the current to the coil is varied, the actuator moves in a linear fashion. Its function can be interrupted by interference from any other magnetic fields around the housing and by micro-vibrations disturbing its motion. Therefore, the ZPD signal produced by the ACU may not remain as the median of the acquisition window. A large shift in ZPD position can lead to degradation of spectral resolution [179]. Thus, another method is developed under CAS to record a finer Zero position. At the same time, the relative shift in Zero position between consecutive scans are saved and a feedback loop is developed to adjust the acquisition window to ensure the ZPD signal in the middle.

4.1.1.4. Develop and follow data file structure

The data saved in the final data files will be used by stakeholders for post-processing. Under CAS a set of well-defined protocols have been developed to save each entry to the file. These protocols play a role in determining a number of features, for example the name of the files and byte number to the entity to be saved.

4.1.1.5. Detect anomalies and modify operations

The nominal operation of the IFTS can be interrupted by various actions, for example unstable arm motion, zero position shift, electronics faults, and computer misbehaviour. An important function of the CAS is to detect the anomalies, record them and modify operations to avoid performance degradation. These quality flags help the user to identify the health degradation of the system, and to discover causes and patterns behind it.

4.1.1.6. Operational and health status

A health file is built on the Control PC to keep a record of operational parameters and health status of IFTS. In this file, different components should register their working conditions after a set time. For example, the mean width of the FR signal for the scan is saved here along with its standard deviation from the mean. CAS also provides a set of commands to the user to inquire about various health parameters and quality flags of subsystems. For the flight instrument, this health file would be linked with a ground computer.

4.1.2. Usability requirements

This section discusses the requirements to mitigate the complexity of CAS usage. Table 7 defines the major usability requirements for CAS. The requirements are serial numbered as described in section 4.1 where R represents mandatory, G is desirable, and W is declared statements.

Table 7: Usability requirements for York IFTS.

ID	Description	Rationale
R-USY-010	All the data from each channel corresponding to a single scan shall be registered in the single data file.	*To make post-processing easier.*
R-USY-020	The software on the microcontroller shall be transferable to another microcontroller with the same part number.	*To replace broken parts.*
R-USY-030	The CAS shall work with single or both channels operable.	*To make it workable in case data from only one channel is required.*
W-USY-050	The English language will be used to interact with the user.	
G-USY-60	Coordinated Universal Time (UTC) should be used for relative time reference.	*The instrument will be used at different geolocations. To remove the need for inculcating geotagged and seasonal clocks.*
W-USY-70	The user will input the Global Positioning System (GPS) coordinates.	*To derive the position of the Sun* *To geotag the column amounts of CO_2 and CH_4.*
R-USY-80	The user shall be prompted to an error message for an invalid input	*Most of the user inputs are interwoven. Their domains and ranges overlap with each other.*
R-USY-90	The user shall be able to ask for system health during operation.	

4.1.3. Performance requirements

This section provides an explanation of data gathering variables of CAS and its performance. Table 8 defines static and dynamic numerical requirements engaged in CAS. The requirements are serial numbered as described in section 4.1.

Table 8: Performance requirements.

ID	Description	Rationale
G-PRF-010	Metrology laser signal should be used as a unit to control and record events.	*To maintain consistency for data relatability in terms of OPD.* *To perform space sampling of the interferometer.*

R-PRF-020	Data from microcontroller shall be transferred after the end of the acquisition window.	*To reduce the burden on camera PC during acquisition.*
R-PRF-030	Data transfer time between the microcontroller and camera PCs shall be shorter than the turnaround time.	*To reduce the burden on the microcontroller to transmit data during the scan.*
R-PRF-040	CAS shall be able to run the IFTS for period of days without real-time human interference.	*To acquire a substantial quantity of data for analysis.*
R-PRF-050	Any inquiry by the user regarding current operational parameters of the system shall be completed within the turnaround time.	*To avoid interfering in the subsequent Acquisition Window.*
R-PRF-060	The responsivity of the system shall be fast enough to inculcate user commands for the consecutive scan within the turnaround time.	*To avoid interfering in the subsequent Acquisition Window.*
R-PRF-070	Data produced by any entity should have a stamp printed in the memory.	

4.1.4. Logical database requirements

This section mainly deals with the file naming and formatting protocols and other database requirements. Table 9 summarizes logical database requirements along with rationales. They are serial numbered as described in section 4.1.

Table 9: Logical database requirements.

ID	Description	Rationale
R-LGL-010	The microcontroller shall be able to distinguish among commands for PC1, PC2, and microcontroller	*User inputs command through the control PC and microcontroller acts as a data bridge between control PC and Camera PCs.*
G-LGL-020	Only the control PC should be used to upload commands to the system in IFTS operational mode.	*For the next TRL a flight instrument, the control PC will act as TT&C with the ground station.*
R-LGL-030	The acquisition window shall be shorter than the scan window (SW from ACU).	*Outside of scan window, the arm is at the extremes of its motion extent and is turning around.* *To control the number of images acquired.*

R-LGL-040	Length of acquisition window shall be controllable.	*To keep the coarse ZPD in the middle.*
R-LGL-050	All components carrying fractions of CAS shall be able to interact with each other.	*Components dictate to each other to perform tasks and control local states of each other. Any broken link hinders the nominal operation of the system.*
G-LGL-060	A set naming protocol should be used to create and save the data files.	*Each data file corresponds to a specific scan. The name should signify the date and time of scan and level in data processing hierarchy.*
R-LGL-060	Mean and standard deviation of FR cycle width shall be recorded in the data file for each scan.	

4.1.5. Design constraints

This section defines requirements and limitations imposed on CAS by other IFTS components and systems.

4.1.5.1. The interface between the camera and PC.

The CAS is constrained by the data rate transfer of USB 2.0 i.e., the interface between the camera and PC. This dictates the rate of image transfer from the camera to the PC and hence translates into deciding the arm speed and integration time for each camera. Theoretical data transfer rate of USB 2.0 is 480 megabits per second or 60 megabytes per second.

4.1.5.2. The interface between microcontroller and camera PC

Data transfer rate between the micro-controller and the Camera PC is also a constraint for the software. For each scan, some of the data is acquired and is saved in the microcontroller's memory. Since the data corresponding to each scan is required to be saved in the same data file, this data needs to be transferred to the Camera PC where images and other operational

parameters are saved. Henceforth, the microcontroller's available memory and data rate are needed to be logically traded off to find an optimized way to transfer the data.

4.1.5.3. Motion of the arm

CAS is also constrained by the specifications of the motion of the arm. The modulator arm travels in one direction for the time decided by the user's input of arm speed and resolution. The turnaround time is hence variable and relatively short for faster speeds and lower resolutions. Any processes which are needed to be done during the non-scan motion of the arm should be done during the turn-around time. Figure 42 shows the typical motion of arm from the turn around to next turn around. The widths of windows mentioned in the figure are a function of arm speed and resolution.

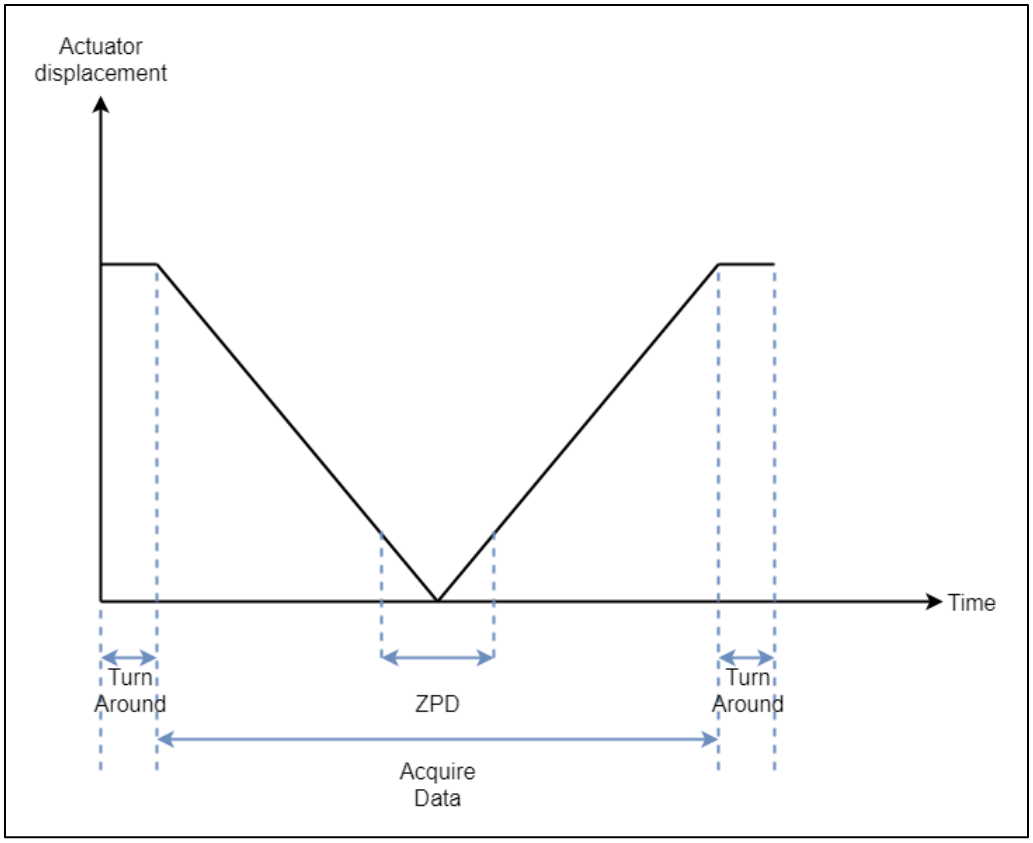

Figure 42: Typical scan windows.

4.1.5.4. Coarse ZPD width

The width of the ZPD signal produced by the ACU is also variable and depends on the arm speed. Thus, a logical method is needed to sample it at an appropriate speed and to detect its position in the acquisition window.

Table 10 illustrates the ZPD signal width in the time domain from ACU.

Table 10: Speed of modulator arm v/s width of ZPD and turn around signals.

The speed of arm (Hz)	**ZPD signal width (approx.)**	**Turn around time (approx.)**
6000	97 microseconds	76 milliseconds
3001	167 microseconds	148 milliseconds

500	900 microseconds	550 milliseconds
300	1.6 milliseconds	1.32 seconds
200	2.4 milliseconds	2 seconds
150	3.4 milliseconds	2.92 seconds
100	4.6 milliseconds	3.96 seconds

4.1.6. Software system attributes

This section specifies the required attributes of the software product. It discusses reliability, availability, security, maintainability, and portability of CAS.

4.1.6.1. Reliability

CAS has an operations mode and a diagnostic mode.

- In diagnostic mode, the developer can access each component separately that carries a fraction of CAS. This way, the faults or failures can be identified and isolated. A different set of diagnostic commands are developed to simulate the inputs from other sub-systems to control the autonomy. Therefore, the diagnostic mode provides initial, periodic and continuous testing for computer elements and other components of the IFTS system.

- In operations mode, IFTS runs its nominal behaviour. During every power recycle, CAS performs a health check of various components and reports them in the health file on the control PC. After reporting good health, the IFTS starts it processes. Any anomalies in the system during operation are recorded in the final data file. For a set of abnormal behaviours, CAS is programmed to restart the system and recover from last saved operational parameters. The symptoms are sent to the CPC and are saved as a health file.

4.1.6.2. Availability

- Minimum availability is more than 14 hours to cover an entire stratospheric balloon mission [180].

- During the 14-hour window, absolutely no downtime is tolerated.

4.1.6.3. Security

- The CAS uses the computers' default operating system security. It does not use any of its own security features since the software is not web-based and does not run over a network.

- The software is contained on four components namely: CPC, microcontroller, CAM762PC, and CAM1600PC. The data files are encrypted since the data stored in these files should be easily modifiable and readable.

4.1.6.4. Maintainability

- A developer can easily maintain CAS. A new version of the code on the microcontroller can be uploaded via the control PC over the USB 2.0 interface.

- The camera PCs can be accessed directly via the inbuilt USB 2.0 interfaces and new software versions can be uploaded. The CAS programs are built using components/subroutines that are as independent as possible to make the system easily modifiable.

4.1.6.5. Portability

The portability of CAS is not a major objective of the IFTS development. The codes are written in a platform dependent programming language; therefore, CAS is a platform-specific software. Individual hardware components must be replaced with similar parts containing the same operating system.

4.2. Control and acquisition software architecture

This section provides an overview of the Software Architecture (SA) used for the York IFTS. SA is a key component that summarizes the "solution" for CAS. Major software components of the

IFTS and the interfaces (internal and external) between them are defined. It transforms all the software requirements described in the Software Requirements Section 4.1 into definitions of software components and their interfaces. *A physical model* is built using software engineering methods [181] to achieve consistency. The physical model describes the design in implementation terminology - for example computer, file, record, software components, and hierarchy of control.

This section also provides an architectural overview of the system, using several different views to depict different aspects of the system. It is intended to convey significant architectural decisions which have been made in the design of the system. It describes the high-level design and technology decisions of the CAS package for the IFTS.

4.2.1. Viewing platforms

This section outlines three core viewpoints for the CAS architecture Components, Deployment, and Process view.

4.2.1.1. Components View

The main components view includes the system and user interface specifications i.e. the different software and hardware components that make up the system. Figure 43 shows the component diagram of the IFTS with the following colour coding scheme.

- Components with a blue background are the one accessible by the user. These include the User Interface - allowing to input Setup Data Files (SDF), Health Data File (HDF), Instrument Data Files (IDF) for channel762 and channel1600. Section 4.2.4 discusses these data files in detail.

- Components with a grey background i.e., Control PC (CPC), ABB Control Unit (ACU), Microcontroller, CAM762PC, and CAM1600PC have a computing role in the IFTS operations.

- Subsystems with a yellow background i.e., White light lamp, metrology laser, voice-coil motor, line conditioner, trigger drivers, CAM762 and CAM1600 are electronics components.

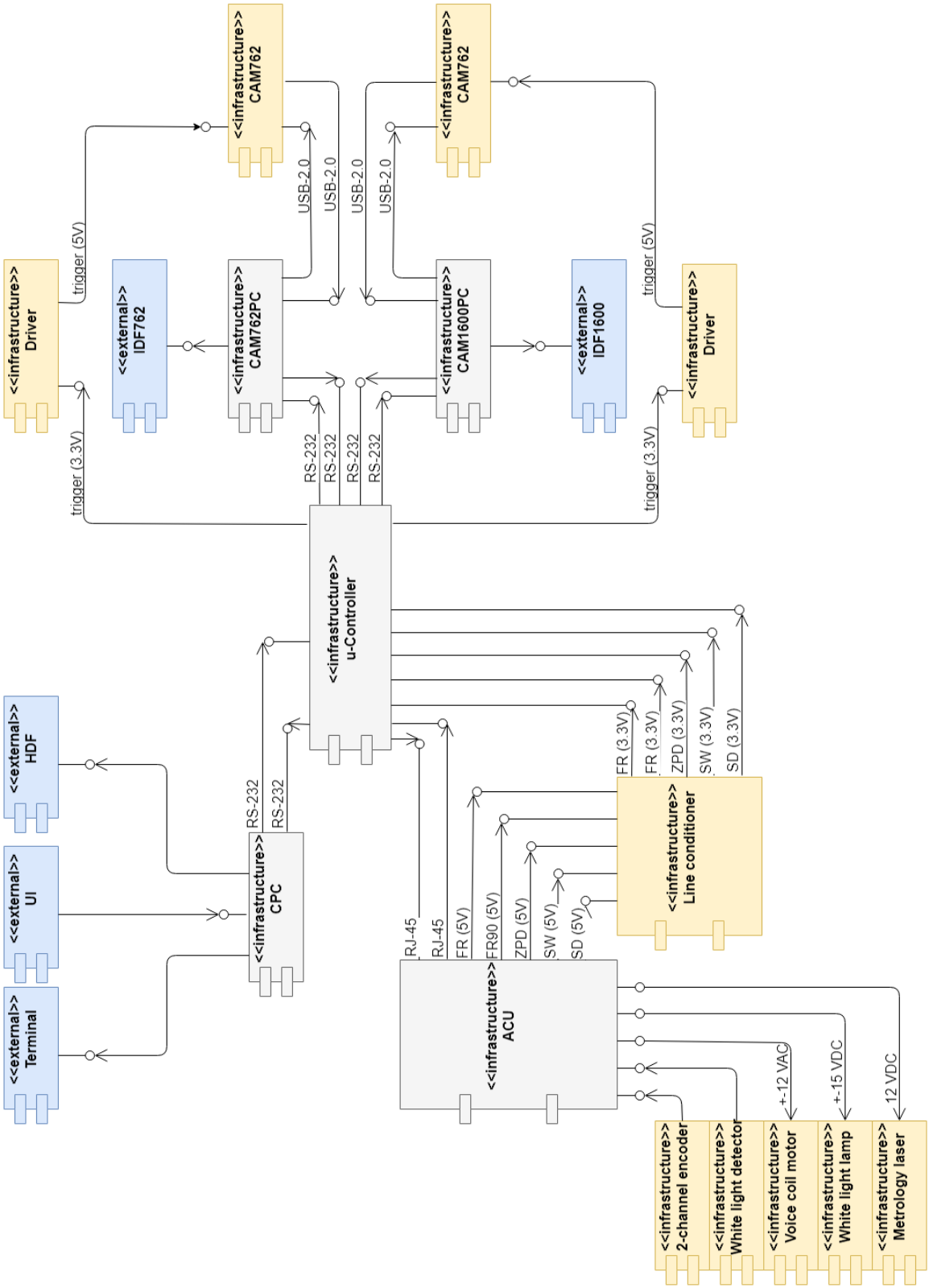

Figure 43: Components diagram for York IFTS.

4.2.1.2. Deployment view

Figure 44 shows the UML deployment diagrams to document the runtime platform model.

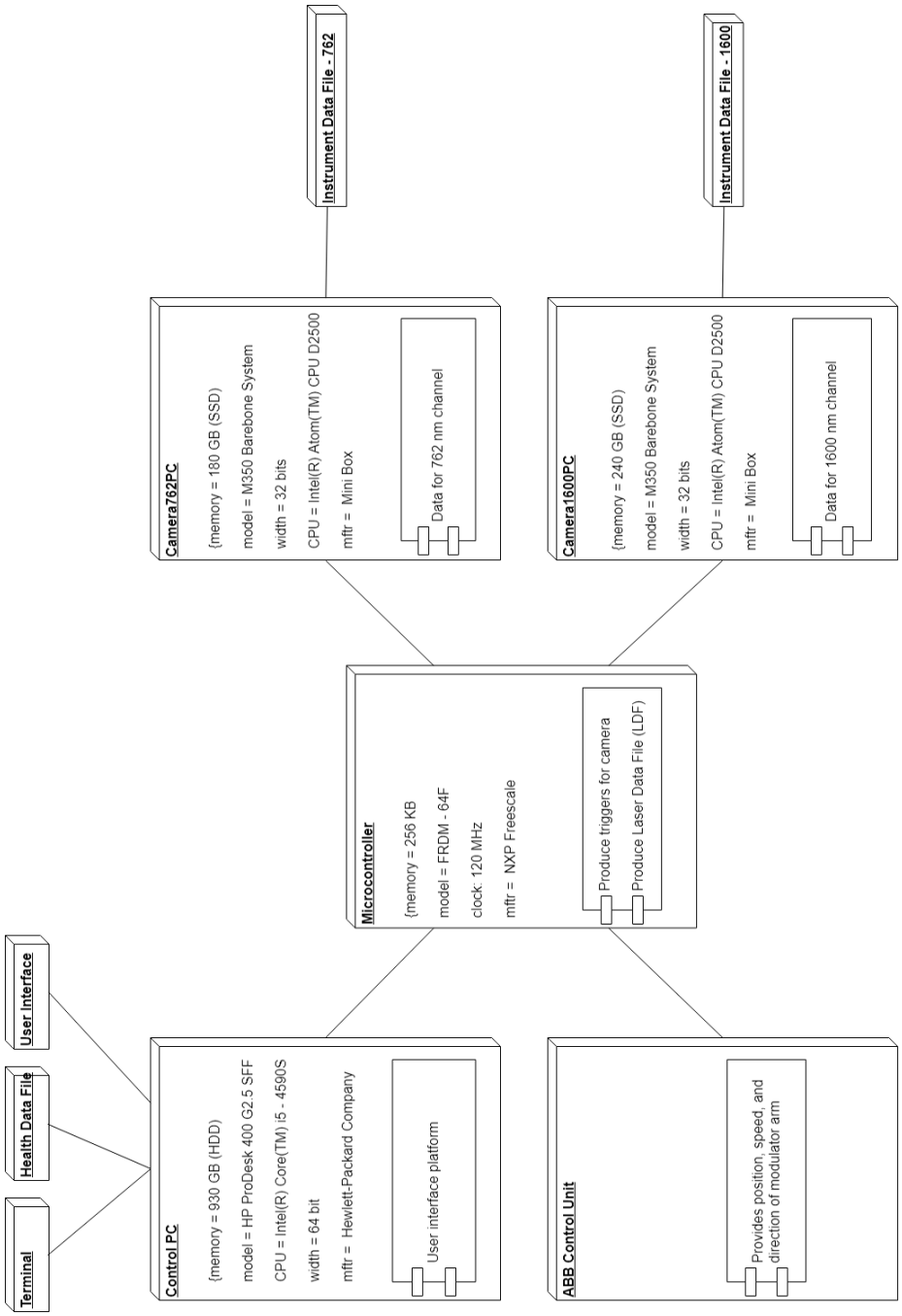

Figure 44: Deployment diagram for York IFTS.

The deployment view depicts how the different systems' nodes come to life together as well as how each of the software nodes are installed and deployed. The deployment view of CAS shows the physical nodes on which it executes. CAS consists of five major physical nodes which are interconnected with software modules: CPC, u-Controller, ACU, CAM762PC, and CAM1600PC. All the instrumental data files of camera PCs are acting as a system database. It shows computing nodes with software elements inside them and associations between the nodes representing the required communication links [182].

4.2.1.3. Process view

The dynamic view displays the processes that form the systems' mechanism. These are represented as sequence and state diagrams. The process view also describes the systems' decomposition as well as the forms of communication between processes i.e. messaging passing, activity between components, and messaging sequencing. The description of process view functionality can be explained by sequence flow diagram and state diagram.

4.2.1.3.1. Sequence diagrams

Figure 45 below describes the full model implementation details of the entire scenario from "Idle state" to "Turn Around state" of the IFTS system.

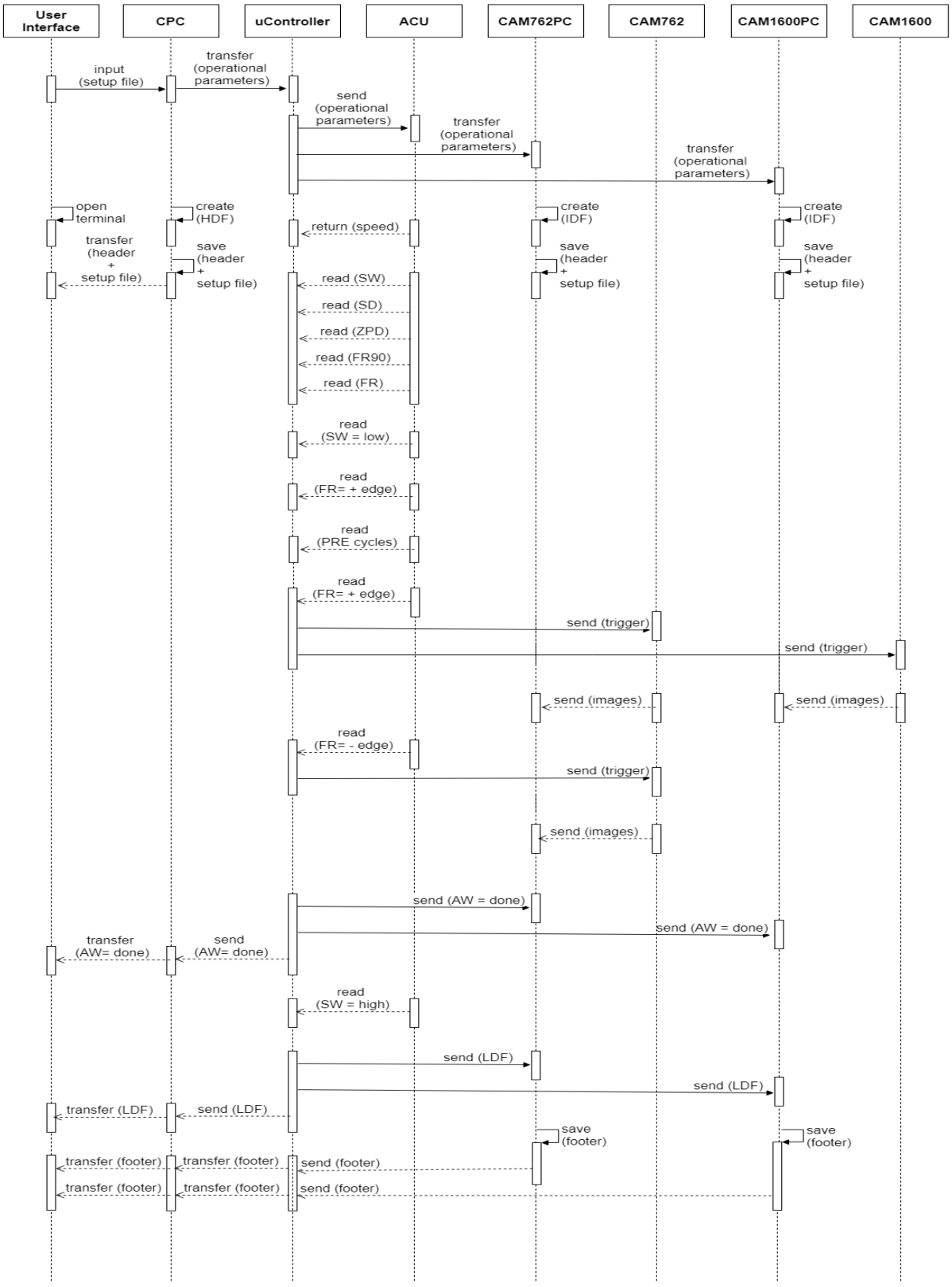

Figure 45: Sequence diagram for York IFTS.

The description of the process view of the flow of sequence diagrams is as follows:

- The operational parameters are sent by the user from the CPC in the form of a .csv file named the Setup Data File (SDF) to the microcontroller and both Camera PCs. This logic of SDF transfer complies with G-LGL-020 mentioned in section 4.1.4 and the input parameters comply with requirements G-FUN-130, G-FUN-140, G-FUN-150, G-FUN-160, G-FUN-170, G-FUN-180, G-FUN-190, G-FUN-200, G-FUN-210 as discussed in section 4.1.1.1 and W-USY-180 in section 4.1.2. The format of SDF is detailed in Appendix VIII, IX, and X.

- The microcontroller decides the component to which the setup parameter belongs depending on the prefix of the command line and transfers them accordingly. This business unit complies with the requirement R-LGL-010 mentioned in section 4.1.4.

- The microcontroller and both cameras send an acknowledgement back to the CPC which confirms the accepted and rejected setup parameters. This business unit complies with requirements R-USY-190, as discussed in section 4.1.2.

- The Control PC shows all the data coming in and going out on the Terminal window. It also makes a Health Data File which saves all these transactions. This business unit complies with the section 4.1.1.6 and the requirement R-USY-200 in section 4.1.2.

- The Microcontroller saves auxiliary data in its volatile memory in the Laser Data File (LDF) which refreshes with every scan.

- Camera PCs create an individual IDF for each scan to populate the observational (Camera Data File or CDF) and auxiliary data (LDF). This complies with requirements R-USY-010, as discussed in section 4.1.2.

- The microcontroller reads and uses the signal coming from the ACU to run interrupts for its own program and to produce external triggers for external cameras. This complies with the requirement G-PRF-010 from section 4.1.3.

- The CAM762 is triggered to acquire the data at both edges (positive and negative) of the metrology laser's FR signal.

- The CAM1600 is triggered to acquire the data at only positive edges of the metrology laser's FR signal.

- Camera PCs take 1000 images in its RAM memory which acts as a buffer and then flushes them to the disk memory.

- While taking the images, the camera PCs are always looking for traffic to come from the serial as a parallel process. If the camera PC sees any data coming from the serial, they stop acquiring images and process the serial data.
- Following the last trigger to the cameras, Freescale sends a “Done” command to both the camera PCs to acknowledge the end of the acquisition window.
- Freescale sends the Laser Data File to both the camera PCs which gets saved in the same Instrument Data File. This complies with the requirement R-USY-010 from section 4.1.2 and R-PRF-020 from section 4.1.3.
- Camera PCs lay down footers in the IDF and transfer them to the Control PC to be saved in HDF and displayed on the Terminal window.

4.2.1.3.2. State diagram

Figure 46 describes the state diagram functionality for the IFTS system over time.

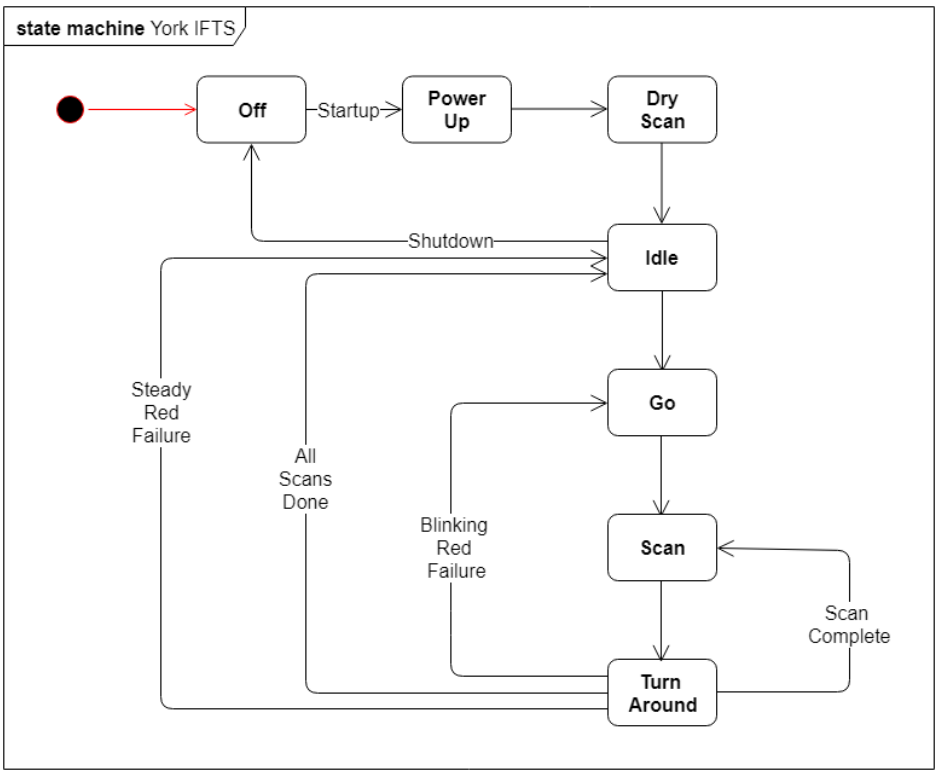

Figure 46: State machine diagram for York IFTS.

Description of each state is given below in Table 11.

Table 11: States machine description for York IFTS.

Sr. #	State name	User interference	Description
1.	Power-off	No	No power is being supplied to the system.
2.	Power-on	Yes	The switch is turned on and power is supplied to the entire system.
3.	Dry scan	No	Power and communication status checks for all the hardware components of the IFTS system.
4.	Idle	Yes	The system waits for the user to input operational parameters in the setup file.
5.	Go	No	Operational parameters from setup files on Control PC are transferred to respective hardware components. The modulator is brought to user-decided speed and resolution. Creates IDF on Camera PCs, Health Data Files (HDF) and System status on the Control PC.
6.	Scanning	No	The system performs the nominal operation. Acquires images for both channels and populates IDFs. This state achieves the requirement R-PRF-040 from section 4.1.3.
7.	Turn Around	No	Laser Data File (LDF) is sent by the Freescale to populate IDF on camera PCs and Health Data File (HDF) and Terminal on Control PC.

4.2.2. Quality

This section defines clear system-wide error handling strategy to provide enough information for availability needs. All errors are logged and reported to the user.

4.2.2.1. Dry Scans

This section outlines the health checks that the system does autonomously after it is powered up. During these tests, the system is in the “Dry Scan” state. The system runs the dry scans and

outputs the Dry Scan-data File (DSF) on the control PC. The dry scan tasks are described in Figure 47 using boxes–and–lines diagram where each rectangular box shows the occurrence of an event and with subsystems shown in colour blue. Arrows between the subsystems show the type of test (power or communication) and arrows going vertically down signify the temporal sequence of the events.

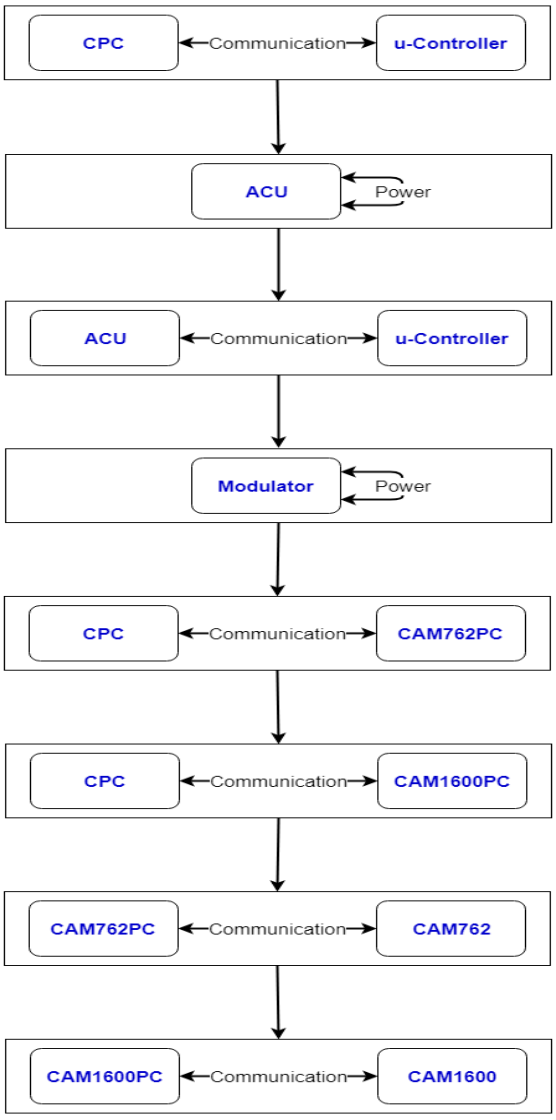

Figure 47: Dry scan tasks for York IFTS.

4.2.2.2. Noisy signal

Figure 48 and Figure 49 show the SD signal from ACU with frequent and random noise peaks of significant amplitudes during high and low outputs. This abnormal behaviour of the hardware platform is corrected using CAS's capability to comply with requirement G-FUN-090 from section 4.1.1.

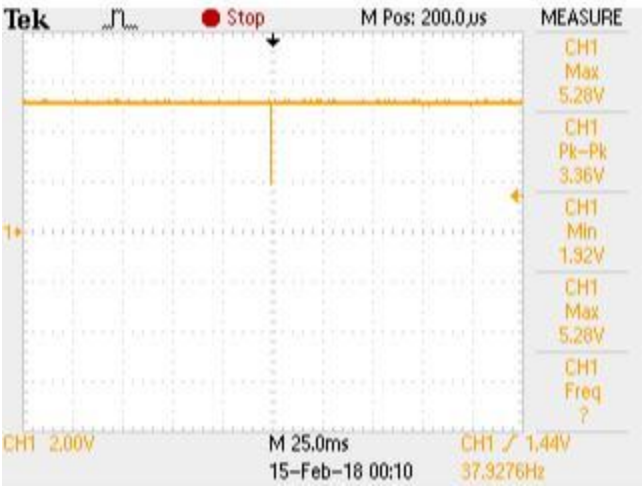

Figure 48: High SD signal with noise at speed = 500 Hz

Figure 49: Low SD signal with noise at speed = 500 Hz

The fault tolerance of CAS is achieved by using a multiplexing technique in the following way:

- The microcontroller independently writes the status of SD 10 times and employs a real-time "voting" system to compare these SD statuses corresponding to consecutive FR cycles which identifies any inconsistencies between them.
- For this set of status record, only the status corresponding to the majority is recorded in the non-volatile memory of the microcontroller which later gets saved in the Laser Data File (LDF).

4.2.2.3. Acquisition window

Images captured by a channel camera are acquired when the system is in the "Scan" state. This time interval is called the acquisition window. Figure 50 shows the acquisition window between two "Turn Arounds", the ZPD in the middle of it.

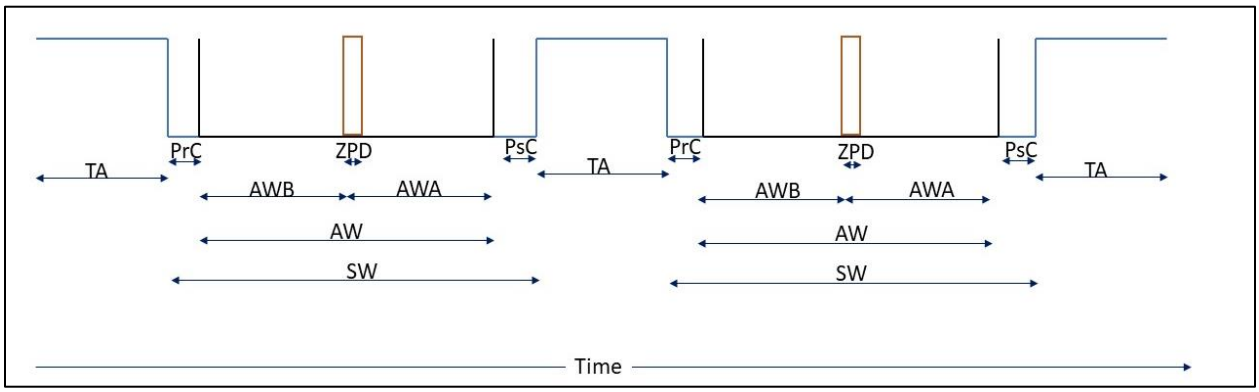

Figure 50: Acquisition windows for York IFTS

The mathematical constraints (for n = number of FR cycles) are listed below in Table 12:

Table 12: Mathematical constraints to adjust Acquisition Window.

1.	$n_{SW} > n_{AW}$	Number of FR cycles of Scan Window is greater than that of Acquisition window)
2.	$n_{SW} = n_{PrC} + n_{AW} + n_{PsC}$	Number of FR cycles of PreCount, Acquisition Window and PostCount add up to equal time interval of Scan Window)
3.	$n_{PrC} + n_{PsC} = n_{SW} - n_{AW}$	Number of FR cycles between scan window and acquisition window is equal to the time sum of PreCount and PostCount.
4.	$n_{AWB} = n_{AWA}$	In the ideal acquisition window, Number of FR cycles before the positive edge of the Zero Path Difference signal is equal to the number of FR cycles after the positive edge of Zero Path Difference.

To comply with the requirements R-FUN-040 from section 4.1.1.1 and R-LGL-030, R-LGL-040 from section 4.1.4 for keeping the ZPD signal from ACU in the middle of the acquisition window, the pre-count and post count values are adjusted autonomously by CAS. For the first scan, Acquisition Window is of the same width as the width of SW signal from ACU with PrC = 0. The microcontroller records the number of FR cycles and camera triggers on both sides of ZPD.

If the number of FR cycles before the ZPD (AWB) < number of FR cycles after the ZPD (AWA), then set PrC = 0 and continue sampling as before with the same number of FR cycles before ZPD but reduce the number of cycles after ZPD to make AWB = AWA, resulting in PsC > 0.

If AWB > AWA, then set pre = AWB – AWA and the system continues sampling. This makes AWB = AWA with PsC = 0. The PrC is re-adjusted this way for each new scan after completion of the old scan.

4.2.2.4. Failure detection, mitigation and recovery

This section outlines the system failure scenarios and feedback actions during the IFTS operation. The responses are designed to comply with requirements G-FUN-100, G-FUN-110 from section 4.1.1.1. Failures can be classified into the following three different categories:

- The scan mechanism failure which is related to the modulator, ACU and microcontroller with interaction amongst them.
- Channel – 762 failures are related to the CAM762 and CAM762PC.
- Channel – 1600 failure is related to the CAM1600 and CAM1600PC.

Figure 51 illustrates the fault detection tree related to the respective categories with their background colour signifying various flags.

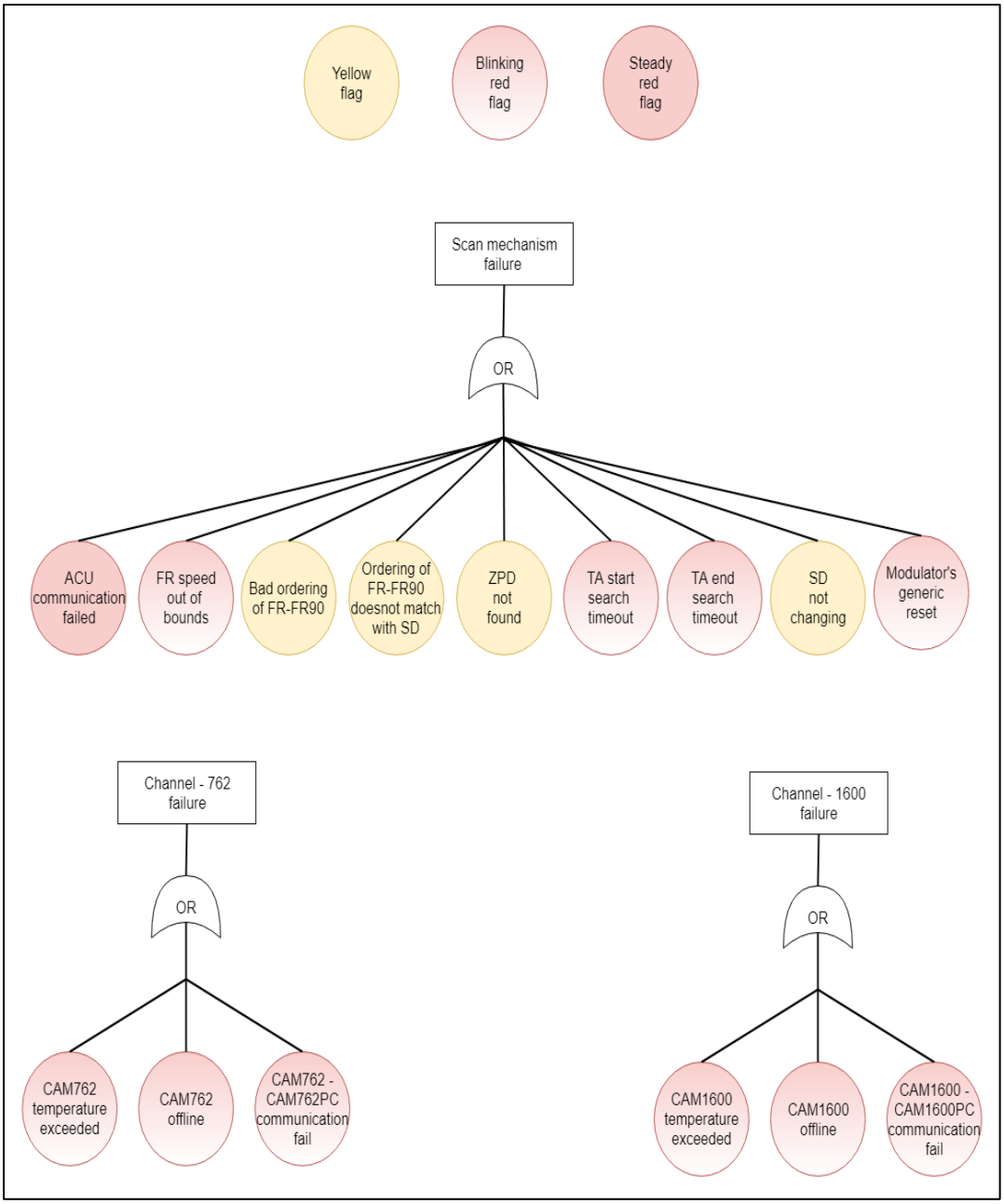

Figure 51: Fault tree analysis for York IFTS

Appendix XI provides the complete lists of the failures scenarios and their detailed description along with the problems they generate. The detection procedure and respective action are also discussed. The problem intensity of each failure scenario dictates the action which directly

implies the recovery action. Each failure can be characterized as yellow (least dangerous), blinking red, and steady red (most dangerous). They can be described as follows:

- Yellow flag: Flag raised in the data file. The system continues with its operations.
- Steady Red: Flag raised in the data file. The system stops its ongoing operations and goes into an idle state.
- Blinking Red: Flag raised in the data file. The system stops its ongoing operations and goes in to reset state.

4.2.3. Performance tactics

This section discusses the ability of the CAS to predictably execute within its mandated performance profile [section 4.1.1]. Architectural tactics to optimize repeated processing and to reduce contention via replication are also outlined. Other strategies which include prioritizing processing, consolidating related workloads, distributing processing over time and minimizing the use of shared resources are also debated in this section.

4.2.3.1. Timing related contention for microcontroller

The Microcontroller performs several concurrent processes especially during the “Scan” state during the IFTS operations. This causes potential for contention between threads of execution. To eliminate this from becoming a significant bottleneck the tasks are performed during ‘GO’, ‘Scan’ and ‘Turn around’ states are shown in Appendix XII with the order of priority levels. A major drawback of this challenge is the inability to read the FR90 signal from the ACU in addition to other signals as mentioned in section 3.6.1. This is caused due to the speed constraint of the modulator arm.

4.2.3.2. Baud rate of microcontroller

The microcontroller has a 48 MHz clock on-board, but the maximum baud rate allowed is 57600 bits per second. The maximum allowed standard transmission rate parameters between the CPC and microcontroller are shown in Table 13:

Table 13: Microcontroller connection settings.

Sr. #	Parameter	Value
1.	Baud rate	57600
2.	Data Bits	8
3.	Parity	None
4.	Stop bit	1
5.	Flow control	No

In the case of the York IFTS, the information unit is one baud (one bit). To minimize the transfer time and to maximize the performance, the highest available baud rate i.e. 57600 bits per second is chosen.

4.2.3.3. Transferring LDF during turnaround

The size and formatting of LDF are discussed in section 4.2.4.4. With the transfer rate of 57600 bits per second, it takes about 77 milliseconds to transfer the entire LDF from the microcontroller to CPC and both camera PCs. These LDFs are transferred during the Turn Around state. This algorithm complies with requirement R-PRF-030 from section 4.1.3.

4.2.3.4. User input during turnaround (buffer)

The CAS allows the user to input operational parameters in the form of a Setup Data File (SDF) during the "Go" state which is used to run the entire operations until the completion of all scans. The user is also allowed to enter the new operational parameters which are implemented in the next scans. This is achieved in accordance with requirement R-PRF-050 from section 4.1.3.

4.2.4. Data formats

Data structures that interface components are defined in this section. Data structure definitions include a description of each element for example name, type and dimension; relationships between elements, for example, the structure; range of possible values of each element, and initial values of each element. The data files saved on the Camera PCs (CAM762PC, and CAM1600PC) are referred to as Instrument Data Files (IDFs). Each IDF contains data from all scans and the total number of scans is dictated by the user. Along with header and footer, it contains data from the microcontroller called Laser Data File (LDF), Camera Data File (CDF) from camera PCs, and Setup Data File (SDF) from Control PC. The files from channel 762 (O_2) and channel 1600 (CO_2 and CH_4) are saved on the CAM762PC and CAM1600PC respectively. This format is designed and followed in accordance with requirements discussed in section 4.1.1.4.

4.2.4.1. Header of IDF

The header is saved at the beginning of the IDF. The Header contains the information related to scan ID, header size, channel name (762 or 1600), date and time when the file is created, the

number of frames in the file number of pixels used in each frame and size of each frame. Appendix XIV discusses the format and example of a header.

4.2.4.2. Setup Data File (SDF)

Setup Data File (SDF) refers to the information derived from the user interface used to set up the parameters of the cameras. This user interface interacts through control PC and is sent to the camera PC through the microcontroller bridge. Each channel has an independent SDF hence when both channels are operational, two SDFs are created and saved. The information from SDF is saved right after the header section of IDF. Following are the SDF components:

A typical User Input has three sets of information.

- The first set is a two-letter command (C7 or C1) which implies the hardware to which the command belongs.
- The second set is the parameter to be controlled.
- The third set is the value of the parameter.

Appendix VIII, IX, and X show the summary of the structure of SDFs stating controllable parameters by the user along with their domain, units and typical values.

Following are the constraints on selecting the pixel window size as implemented by the manufacturer.

- Start X pixel needs to be a multiple of 64.
- End X pixel needs to be a multiple of 64 minus 1.
- Start Y pixel needs to be a multiple of 4.

- End Y pixel needs to be a multiple of 4 minus 1.

4.2.4.3. Camera Data File (CDF)

Camera Data File (CDF) refers to the images acquired by the camera that are saved in the camera PCs. The images are essentially the pixel values corresponding to pixel numbers and time stamped to a microsecond precision (R-PRF-070). Triggers to both cameras to take images are sent independently by the microcontroller. Each image is taken within the pixel window as set by the user in the setup file on the control computer and subsequently transferred to the camera PC via the microcontroller data bridge. Pixel values are saved as digital numbers from 0 to 2^{16} for 16-bit or 2 bytes camera operation. The images are saved as binary and each image is separated by a known divider or synch word.

4.2.4.4. Laser Data File (LDF)

Laser Data File (LDF) refers to the data acquired by the microcontroller by sampling the ACU signals in accordance with the requirement W-FUN-050. It is in ASCII format and contains information derived from the behaviour of the metrology laser signal such as the scan number since the start of scan state, status of SD, length of SW signal, length of AW (R-FUN-080), values corresponding to PrC and PsC, FR cycle corresponding to the ZPD signal (R-FUN-060), triggers sent to each channel (R-FUN-070), mean width and standard deviation of FR cycle (R-LGL-060). Refer to Appendix XIII for detailed formatting of LDF entities.

4.2.4.5. Footer

The Footer is the last part of the IDF and HDF. It is laid down after the Microcontroller sends an acknowledgement of the end of the acquisition window. It contains information regarding the saturated frame numbers, fine ZPD, actual temperature reading of the camera and the total number of frames recorded by counting the synch bytes between consecutive frames.

The structure and semantics of the footer data are listed in Appendix XV.

4.2.4.6. Final structure

The most important components of IDF are as stated in Table 14 below:

Table 14: Final structure of Instrument Data File.

Header: Scan ID, Header size, Channel number, date and time stamp
Setup Data File (SDF): Arm speed, Resolution, Integration time, Pixel Window, Camera Data File (CDF) extension, GPS position, Set temperature,
Camera Data File (CDF): Frames, sync byte
Laser Data File (LDF): Pre-Counts, Post-Counts, triggers762, triggers 1600, Coarse ZPD, ZPD width, SD bit, Interrupt stats, Noise spikes/disturbance
Footer: Time stamp of “done command”, Saturated frame numbers, Fine ZPD, Low light frames, Actual temperature reading of the camera

4.2.4.7. File naming protocol

The instrument data files IDF762 and IDF1600 are saved on CAM762PC and CAM1600PC respectively. The naming protocol is defined in accordance with G-LGL-020 such that the name of each IDF created contains the name of the channel, followed by an underscore sign (_) and

then every two digits for the year, month, day, hour, minute, and second. Parametrically it looks like as follows:

I	D	F	X	X	X	_	Y	Y	M	M	D	D	h	h	m	m	s	s

For example, name of a data file created for 762 nm channel on 4th August 2018 at 3:30 pm and 9th second looks as follows:

I	D	F	7	6	2	_	1	8	0	8	0	4	1	5	3	0	0	9

4.2.5. Technology

From a technological viewpoint, there are five subsystems which have a computing role as described below:

- The control PC (CPC), CAM762PC and CAM1600PC have Linux Ubuntu 12.04X86 operating systems.
- The program written on the CPC to perform the respective tasks as discussed in the sequence diagram (Figure 45) uses C++ libraries.
- The program written on the microcontroller also uses C++ libraries.
- To command and integrate the cameras, CAM762PC and CAM1600PC use the Systems Development Kit (SDK) library provided by the camera manufacturer with part number: Xeneth2.6-Linux-x86_64-2.6.0-1399. SDK libraries are also based on C++ platforms.
- The ABB Control Unit (ACU) contains a “Main Harness” computer board which is trans-receives commands over RJ45 from the microcontroller. No other information is explicitly provided by the manufacturer.

4.2.6. Open issues

This section discusses the causes which can limit the resilience of the CAS in terms of total failure or bad performances. Since the work mentioned in this document is relatively novel and the hardware used does not carry enough confidence to be referred to as “fault-tolerant”, the development of CAS is an ever-evolving process.

4.2.6.1. Single point failure

The microcontroller being the payload master is the central subsystem which controls all other subsystems onboard. It is loaded with tasks to perform during the entire operation of the system. It can be easily identified as the “single point” whose failure can compromise the entire architecture.

4.2.6.2. Ineffective error detection

The error-handling has a wide impact on the operation and performance of the system. A lengthy portion of code is devoted to flag and deal with errors along with implementing core functionality. Even with all the errors listed, there could be more errors which will only be discovered when the system is fully operational. More insight can be gained as more data is analyzed. At this point, the CAS can be edited even further to implement the learnt behaviour.

CHAPTER 5

5.0. MEASUREMENTS AND RESULTS

This chapter discusses various experiments undertaken to understand the behaviour of the instrument. The image plane of the FTS is the stigmatic replica of the object plane, a detector array placed at the output of the FTS that enables imaging spectroscopy, thus exploiting both spatial and spectral multiplexing. A variety of input light sources, optical elements, operational parameters were used to develop a performance model of the instrument which can be used to develop a future version for a satellite platform. All the experiments in this chapter are conducted at a temperature of 23^{o}C to imitate TANSO-FTS [151] and an integration time of 500 µs unless stated otherwise.

5.1. Closed shutter noise

Detectors record same signal independent of light falling on them. This signal is created due to thermally generated electrons and is known as the dark count. It is a statistically varying signal which exhibits a Poisson distribution and is directly proportional to the square root of the integration time for a constant dark count rate. Figure 52 shows the plot of dark noise count on the pixel (208,64) from the 1600 nm channel detector.

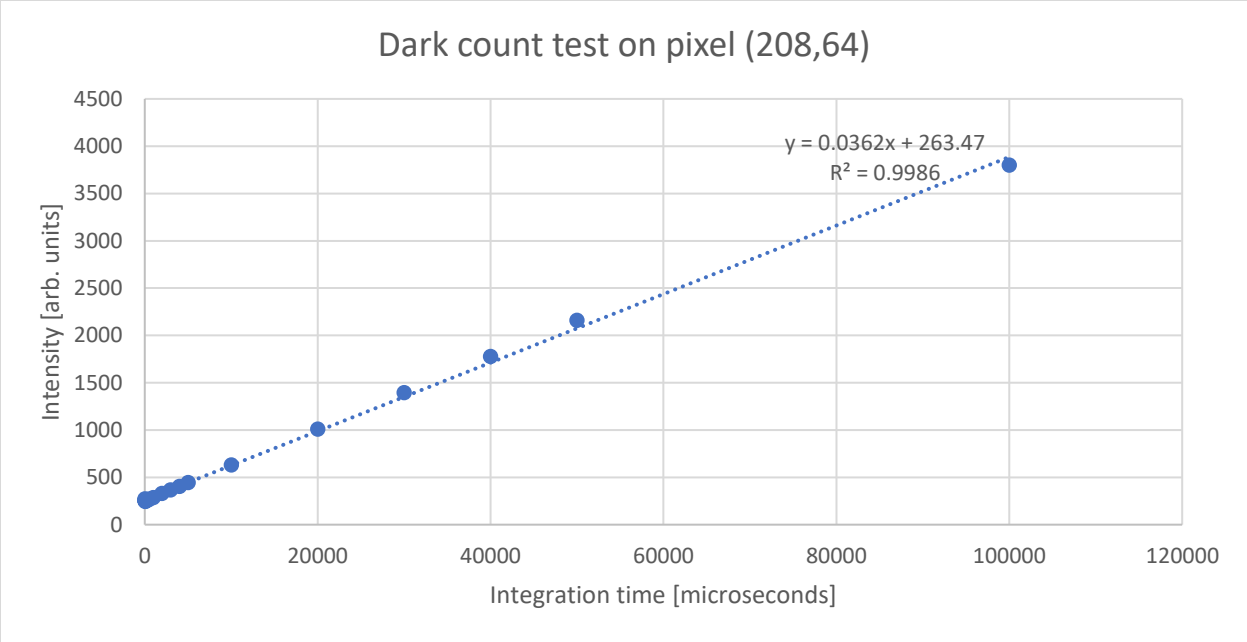

Figure 52: Dark count test on the pixel (208,64). The slope of fitted straight line is 0.0362 with an y-intercept of 263.47 units.

A set of 22 integration times varying from 5 microseconds to 100,000 microseconds are plotted along with the intensity recorded while the detector is kept in dark. The data points are fitted to a straight line with an R-squared value (goodness of fit) of 0.9986. The y-intercept of the fitted line is 263.47 units which is the value of read out at zero integration time. At typical integration time of 500 µs, this dark noise value is found to be 269 units. A similar value is seen at all pixels in both detectors.

Since this dark count adds up to all data points in an interferogram, subtracting the cumulative mean from each value takes away its contribution. Also, subtracting the mean value calculated away from Zero Path Difference (ZPD) is so that the zero-filling to get to 2^N points does not cause a jump in the interferogram. It may slightly improve the numerical precision as well.

5.2. HeNe laser

The spectral response of the York IFTS is calibrated using a Helium-Neon (HeNe) laser. An external laser is mounted on the optical bench and is injected into the aperture of the interferometer. A variation of single pixels is used to collect the data. The modulator is operated at a speed of 500 Hz and external triggers from the microcontroller are sent using the control and acquisition software (CAS). Each data point is sampled at an equidistant space which is the half wavelength of the metrology laser 632.8/2 = 316.4 nm (space sampling) and corresponds to a single frame. An integration time of 500 µs was used on the detector. The collective mean of recorded data was subtracted from each data point to get the AC values. A MATLAB routine (Appendix XVI) was used to perform the Fast Fourier transformation (FFT) on the AC values of the data to get the spectrum. Since the wavelength of the HeNe laser used is known before-hand, any discrepancies from the given value provide an insight into the instrument behaviour for the set of operational parameters chosen for example the pixel number, temperature, integration time, etc. Figure 53 shows the interferogram produced by using a HeNe laser at the centre pixel of the detector and Figure 54 shows the zoomed-in version of the same figure.

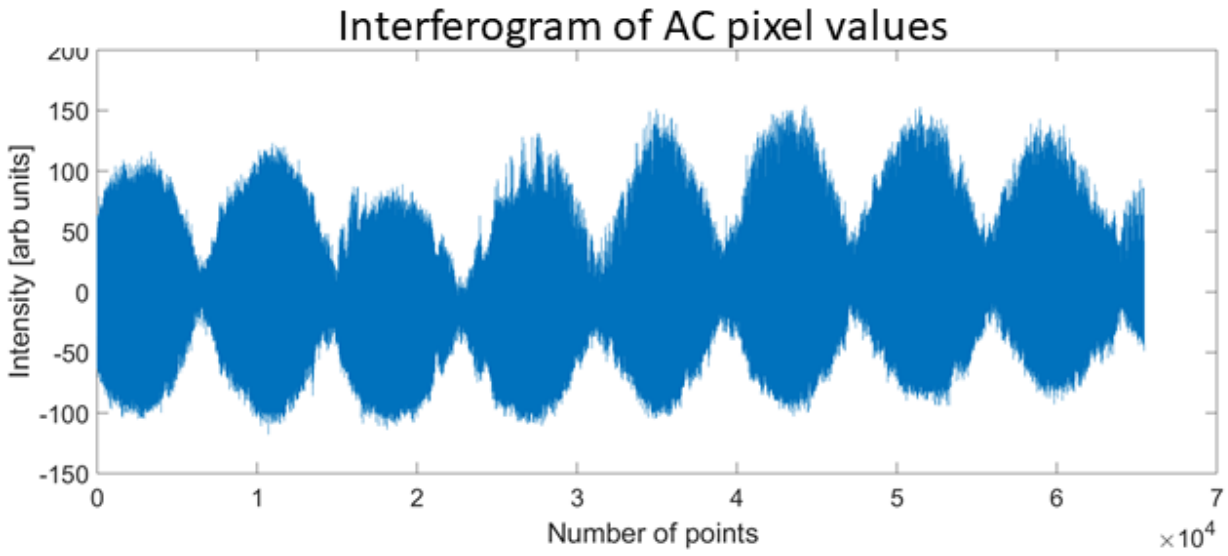

Figure 53: Interferogram of a HeNe laser

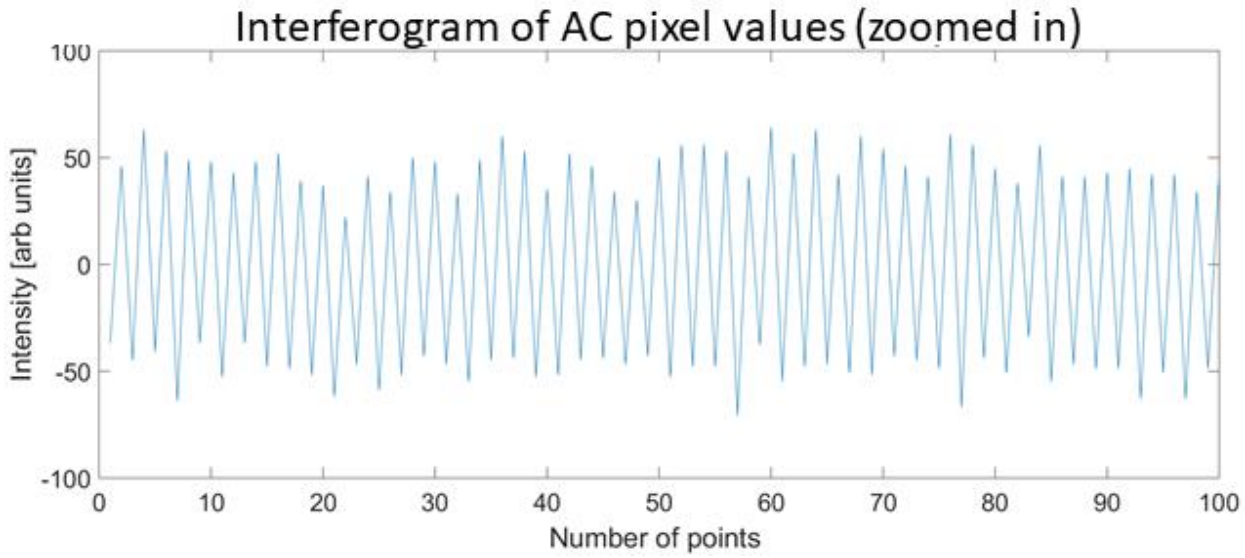

Figure 54: Interferogram of a HeNe laser (zoomed-in)

The interferogram has 65462 points with coarse ZPD corresponding to the 32731st point. The fine ZPD corresponds to the 44265th point which is the point of maximum intensity. The interferogram shows a sinusoidal behaviour due to the monochromatic nature of the laser but

shows an overlapped oscillatory behaviour of ~0.06 Hz due to the resonance of the vibration isolator.

Figure 55 illustrates the raw spectrum produced by performing the FFT on the interferogram shown in Figure 53 and Figure 56 shows the zoomed-in version of Figure 55.

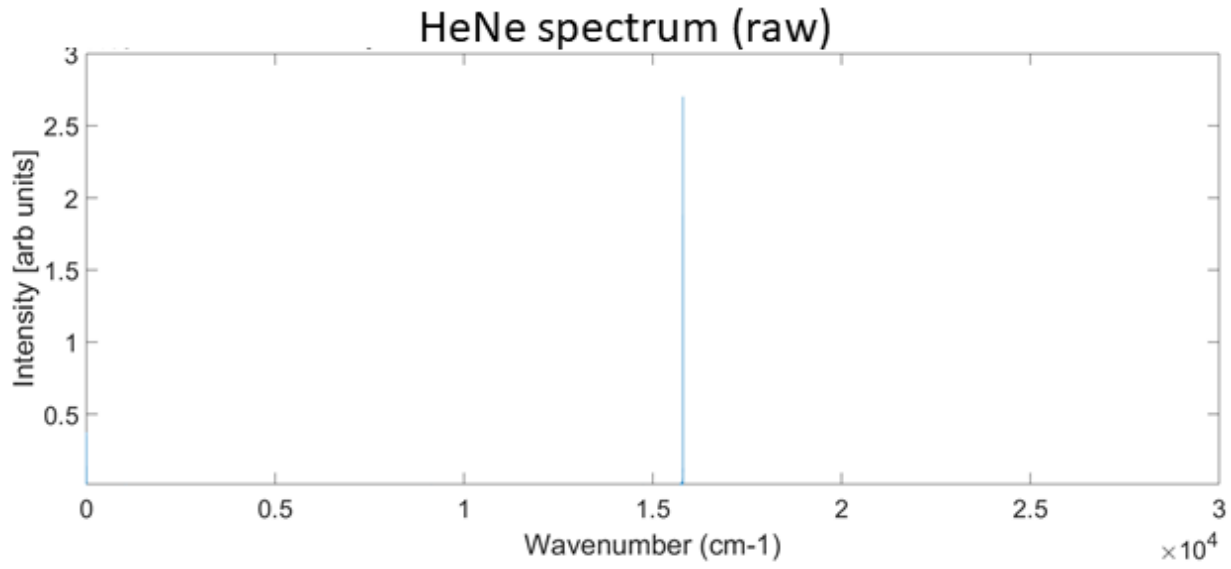

Figure 55: Spectrum of HeNe laser centred at 15801.0 cm-1 (632.87 nm) with FWHM of 0.6 cm-1

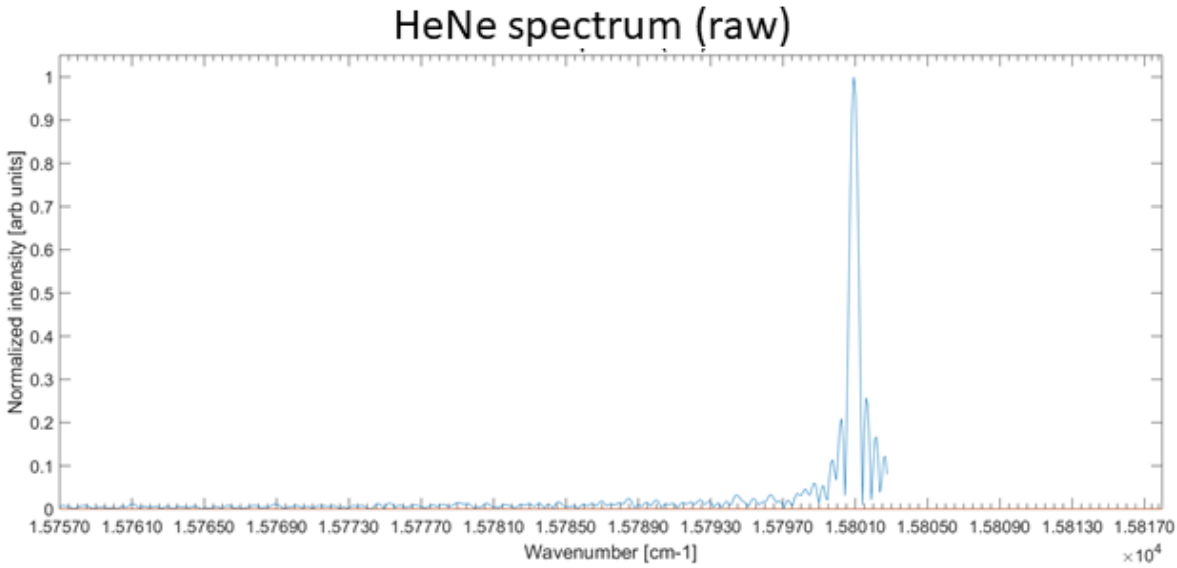

Figure 56: Spectrum of HeNe laser (zoomed-in) centred at 15801.0 cm-1 (632.87 nm) with FWHM of 0.6 cm-1

The x-axis shows wavenumbers and normalized intensity is shown on the y-axis. The peak is centred at around 15801.0 cm^{-1} (632.87 nm), with FWHM spanning from 15800.7 cm^{-1} to 15801.3 cm^{-1}. The measure value (632.87 nm) complies well with the wavelength data provided by the manufacturer (632.8 nm). The spectral resolution of 0.6 cm^{-1} as opposed to 0.5 cm^{-1}, is due to the sinc envelope of the points. Along with the main peak, the side lobes due to the finite and abrupt interferogram limits can also be seen. The metrology laser used to sample the interferogram is also a HeNe laser. This results in barely/minimum Nyquist requirement compliance (refer to section 3.7.2). Therefore, the produced spectrum abruptly ends after around 632.8 nm (wavelength of HeNe laser).

Figure 57 illustrates the same spectrum produced by the same spectrum but using the triangular apodization window.

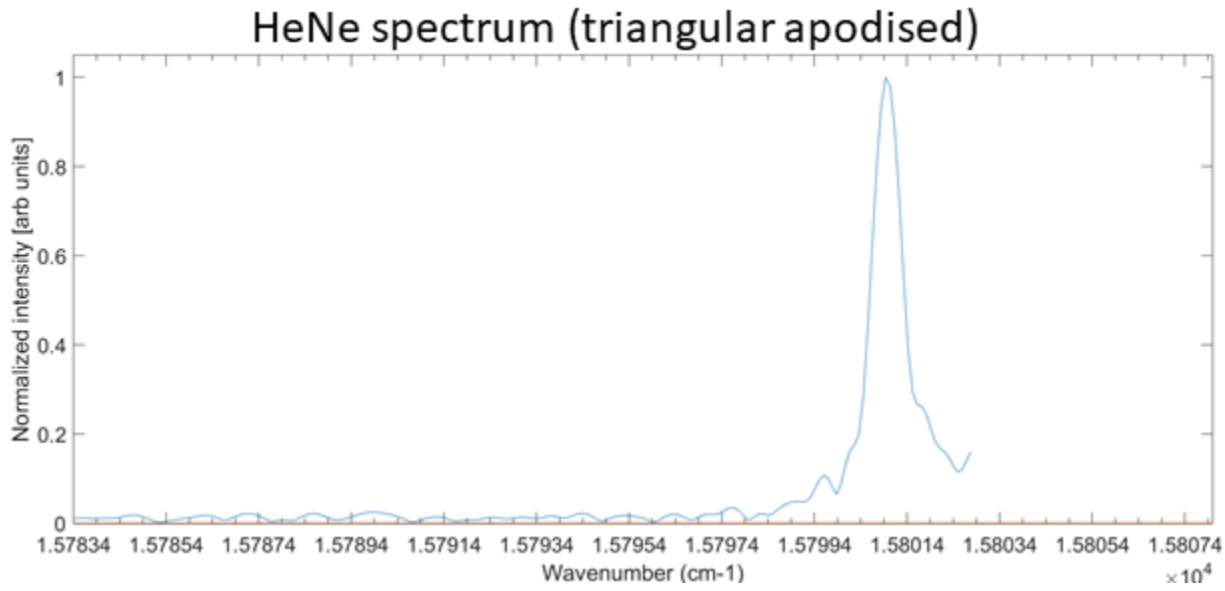

Figure 57: Triangular apodised spectrum of HeNe laser

The peak is centred at 15801.0 cm^{-1} with the FWHM spanning from 15800.6 cm^{-1} to 15801.1 cm^{-1}. This implies a width of about 0.8 cm^{-1}. As compared to un-apodised spectrum in Figure 57,

there are no side lobes, however, the peak is wider. This implies the expected trade-off between the main peak resolution and presence of side lobes.

5.3. White light source

In this experiment, a white light source is used along with a current controlled power supply. It is supplied with 200 W of power at a constant 8 A. It has a tungsten filament which operates at around 3100 K and outputs broadband light. Figure 58 shows the blackbody curve plotted using Planck's function at 3100 K.

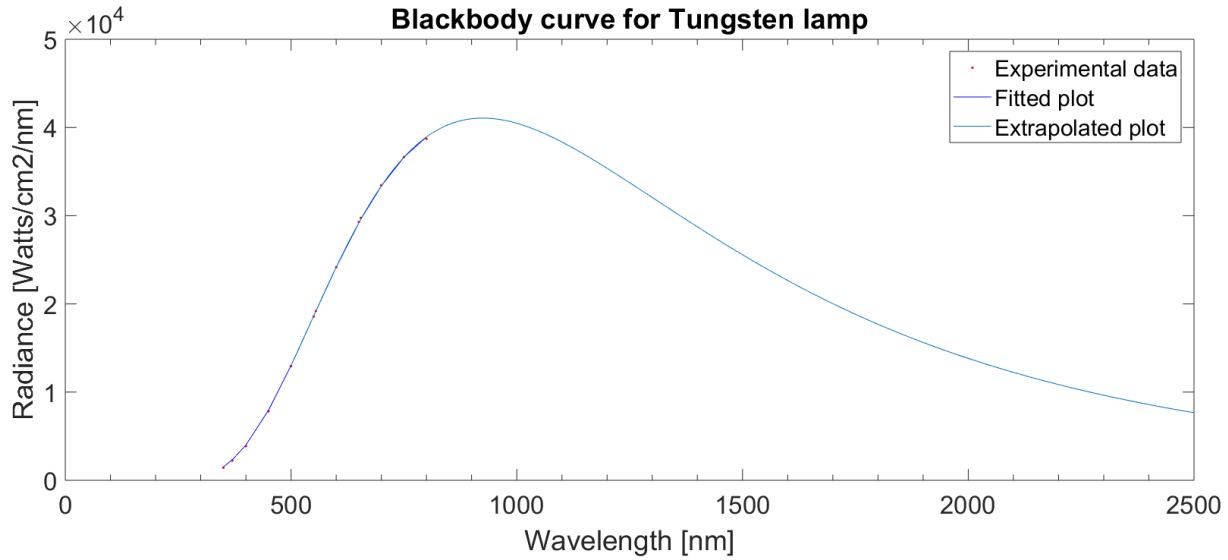

Figure 58: Blackbody curve for a blackbody at a temperature of 3000 K

This broadband light is fed into the aperture of the IFTS and the interferogram is acquired using the detector. Since the input radiation contains a wide range of frequencies, all of them interfere constructively at ZPD and then decay quickly to a mean value as the mirror moves. The interferogram has a large signal at ZPD called the centre burst. The interferogram acquired is Fourier transformed to produce the spectrum. The detectors use bandpass (interference) filters as discussed in section 3.4 to limit the spectral width of the light input to the detectors.

Section 2.5 outlines attributes of the spectrum obtained by using the broadband light source and its behaviour when an interference filter is used.

5.3.1. No bandpass filter

As discussed in section 3.1, a dichroic filter is used to select and guide the light in the spectral range from 700 nm to 800 nm into the visible channel detector. Figure 59 and Figure 60 shows the interferogram and spectrum respectively produced by the detector used in the visible channel.

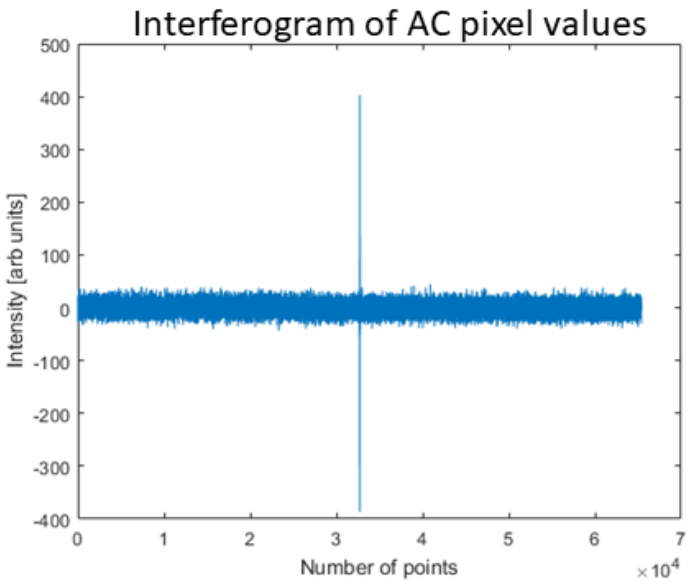

Figure 59: Interferogram of broadband light produced by the tungsten lamp at 762 nm channel detector

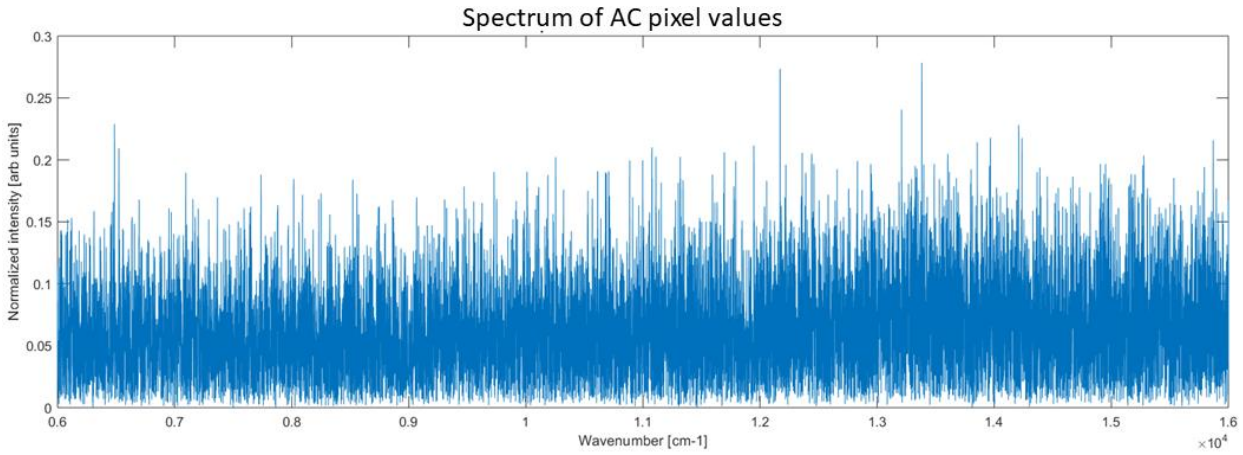

Figure 60: Spectrum of broadband light produced by the tungsten lamp at 762 nm channel detector

The interferogram shows a peak at the ZPD position with a rapid decay as the mirrors move away. The centre burst is caused due by constructive interference of all the wavelength components present in the broadband light. The spectrum does not show any useful information since the data acquired is uniformly distributed with respect to wavenumber and may include aliased wavelengths.

5.3.2. 1600 nm channel

The near-infrared channel (NIR) will be used to measure the mixing ratio of methane and carbon dioxide in Earth's atmosphere. TANSO-FTS also measures these atmospheric constituents in the 1.56 – 1.72 µm [151] spectral region and AIM-North also proposes the similar but narrow spectral range from 1.570 – 1.587 µm [151].

5.3.2.1. Using bandpass filter

The spectral properties of the channel are defined by the attributes of the bandpass filter used. This section discusses the spectra obtained by use of bandpass filters against the input broadband light. The modulator ran at 500 Hz speed and a maximum resolution of 0.5 cm^{-1}. The

instrument was placed on a vibration isolator on the optical bench and was covered entirely with a black cardboard box except for the input aperture. All other light sources in the lab were turned off during the measurements. The source was white light from a 200W tungsten-iodine lamp, scattered off a nearly Lambertian surface. The light passes through a dichroic beam splitter, a bandpass filter centred around 1575 nm and 75 nm FWHM and a focusing lens. The detector was windowed, and data were saved only from a single pixel with an integration time of 500 µs. The input light was sampled once per fringe of the on-board HeNe metrology laser. The DC level was subtracted from the acquired interferogram. Figure 36 shows the bandpass plot of the filter used. Figure 61 shows a typical acquired interferogram.

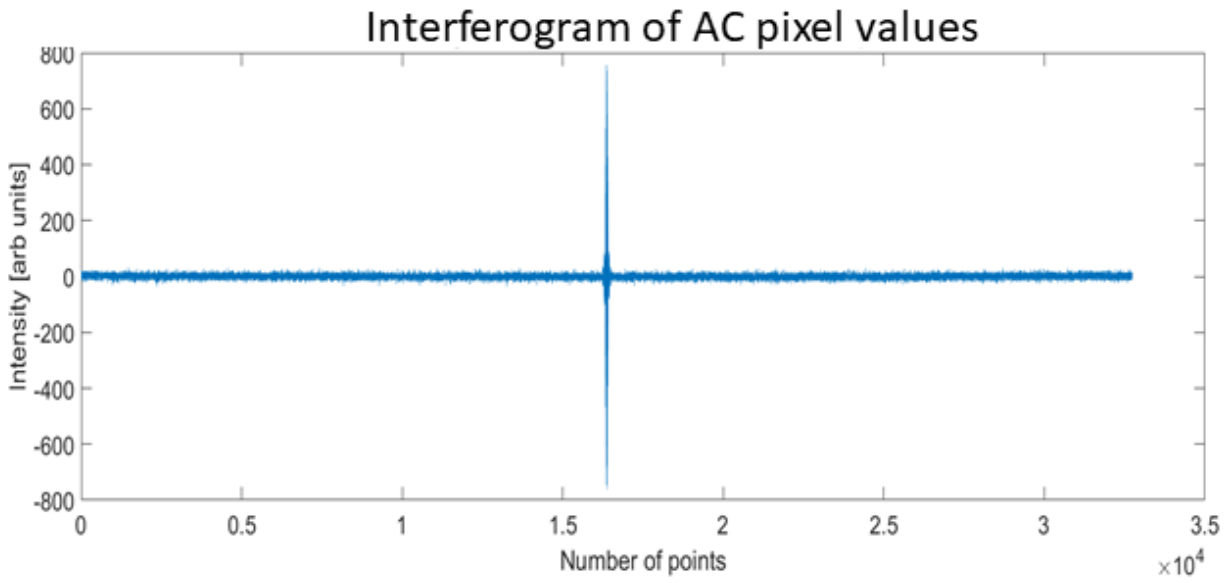

Figure 61: Interferogram of broadband light produced by the tungsten lamp at 1600 nm channel detector against a bandpass filter centred at 6269.59 cm^{-1}.

The interferogram shows 32739 points with the 16362nd point being the point of maximum intensity or fine ZPD with an intensity of 754.4 units above zero value. The mean value of the absolute values of the interferogram is 7.3916.

The interferograms acquired are apodised and transformed to a spectrum using a MATLAB routine. Blue curve in Figure 62 shows the Fourier-transformed spectrum obtained using the mean of 10 data sets.

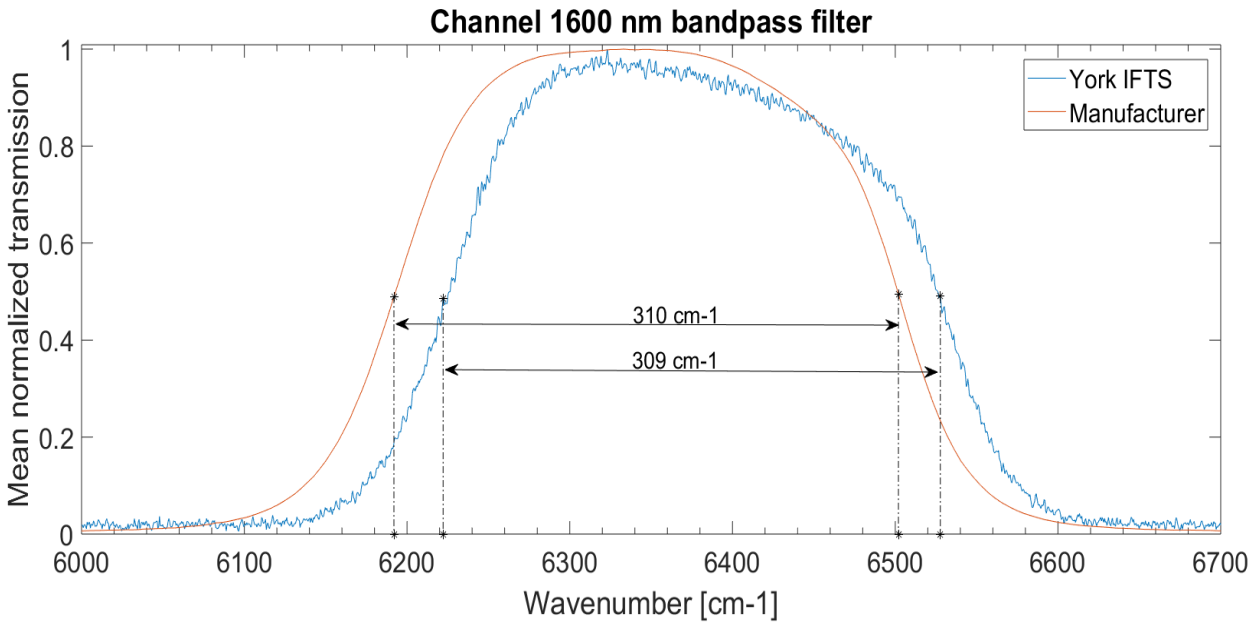

Figure 62: Spectrum of broadband light produced by the tungsten-iodine lamp at 1600 nm channel detector against a bandpass filter centred at 6269.59 cm^{-1}.

The transmission data in red colour, with a precision of 1 nm provided by the manufacturer of the bandpass filter, are also plotted on the same figure for comparison. Both data sets are normalized to 1.0. The results clearly show a very close similarity between the data sets. The manufacturer's data peaks at around 6333 cm^{-1} whereas the York IFTS data has the maximum at around 6323 cm^{-1}, which is a difference of 10 cm^{-1}. The FWHM of manufacturer's data is about 310 cm^{-1} and York IFTS has a FWHM of 309 cm^{-1}, which is a difference of just 1 cm^{-1}. 1 cm^{-1} may well be the resolution of the spectrometer used to test the filter.

Figure 63 shows the line of best fit through the spectrum shown in Figure 62. The fit is a polynomial with magnitude of mean error as 3.8×10^{-4} and standard deviation of 9.6×10^{-3}.

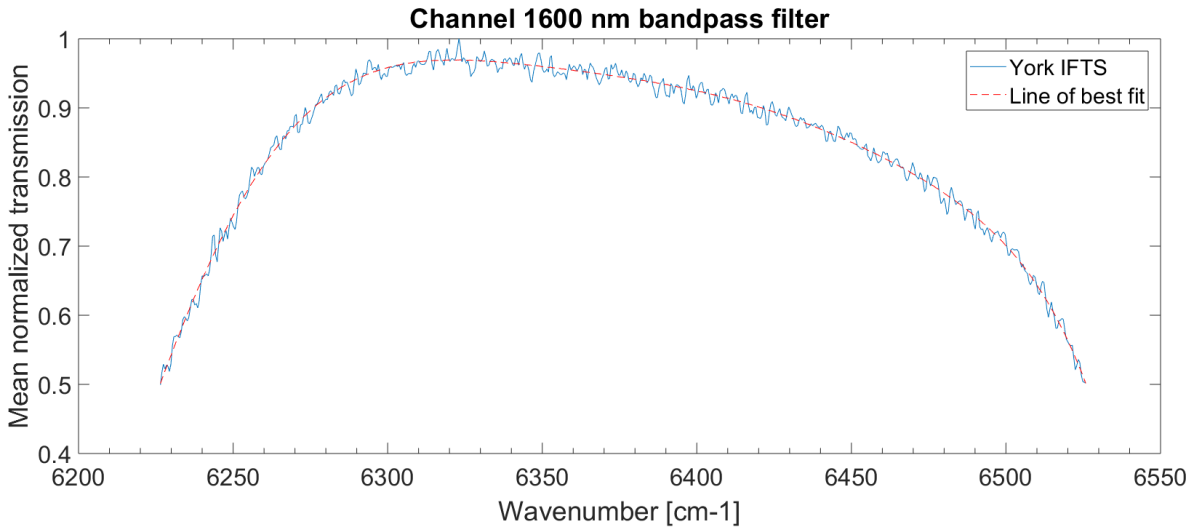

Figure 63: The line of best fit through the mean spectrum of 10 apodised interferograms.

The signal-to-noise ratio is the ratio of the signal to the noise. The line of best fit can be considered as the reference signal and the spread around it from the experimental data as noise. In the plot shown in Figure 63 the mean of summed squared magnitude of signal to that of the noise is 38.9.

CHAPTER 6

6.0. CONCLUSION

The York IFTS was designed and developed to work in the laboratory environment but with a goal to easily turn it into a flight instrument to make measurements of the mixing ratios of methane and carbon dioxide in Earth's atmosphere from a balloon platform. Both scientific and engineering aspects of a Michelson interferometer-based Fourier transform spectrometer were studied and applied. Instead of treating the instrument as a perfect "black box", various components, both hardware and software, were designed and developed in-house at York University. The COTS modulator bought from ABB Inc. was also characterized in-house. Author's contributions particularly involve characterizing the ABB modulator and validating it for imaging spectroscopy, defining requirements and architecture for control and data acquisition software (CAS), testing and verification of CAS, testing the IFTS with a He-Ne laser, and a white light source.

The knowledge, hardware, and software will be used in synergy with other Canadian groups such as Canadian Space Agency (CSA), Environment and Climate Change Canada (ECCC), and ABB Inc., to develop a similar satellite instrument for the AIM-North mission.

It was realized that the modulator was quite susceptible to ground vibrations and no experiments could be conducted using only a heavy optical table. Consequently, a passive isolator was procured to isolate the interferometer and thereafter negligible effects of noise from ground vibrations were experienced. In addition, since the isolator is passive which using a set of springs, it can be flown as a part of a stratospheric balloon payload along with the IFTS.

While working with the detectors and using all the pixels on the entire detector array, it was understood that the arm needs to be run well below the speed of 100 Hz of the metrology laser. This would make the scan longer than 600 seconds which would mean keeping the entire system and the object plain essentially undisturbed for a single scan. This makes the operations more challenging. Therefore, an array of 32x32 pixels was chosen which would be good enough to make scattered solar radiation measurements and the modulator arm can be run at a speed of 500 Hz to complete a single scan in about 67 seconds.

In addition to using all the pixels in the imaging detector, the size of the image formed is also crucial. The pixel pitch as stated by the manufacturer is 30 μm, which implies that the focussed image needs to be contained within that size. Therefore, several lenses were analyzed using optical simulation software, Zemax optic studio 16.5 to study the size of the image formed at both 762 nm and 1600 nm. Finally, a commercially-off-the-shelf (COTS) aspheric lens was used in the final design which was simulated successfully to form a smaller image than the pixel pitch.

Designing the system architecture and interfaces was given thought to keep it open and feasible to be easily developed into a flight instrument. A three-layer control and acquisition software was developed. The first layer consists of a control computer which intakes setup commands from the user and implements them to alter the operations. This control computer can be replaced and used for telemetry and commanding in the flight version of the instrument. The middle layer is a logical layer which consists of some electronics including a microcontroller and software to run it. The third and final layer consists of the cameras, the camera PCs and software to operate the cameras and save images in a pre-defined file format in the PCs. These

data files contain images, auxiliary data regarding the scan report and any bad flags raised during the scan. They can be used as stand-alone entities to post-process the data for a single scan.

An external HeNe laser with known spectral properties was used to calibrate and understand the basic behaviour of the instrument. Similarly, a broadband light from a white light source was used to study the "centre burst" in the interferogram and the noise on it. Several bandpass filters were used to control the spectral widths of the input light into the detector and to define the channels' spectral bandwidths.

6.1. Future recommendations

This dissertation focuses mainly on the design and development of the York IFTS instrument. The recommendations for future work include:

- York IFTS uses Xenics Xeva cameras with USB 2.0 interface. It is not possible to use all the pixels on the detector window and capture images at a frame rate more than 100 Hz. It is therefore recommended to use a camera link interface to use all the pixels by reducing the net scan time.

- Xenics Xeva camera has an InGaAs wafer which has low responsivity for the O_2-A band channel. It is recommended to replace the detector with a silicone camera to achieve higher SNR for this channel. Si also has a larger band gap which produces lower noise levels.

- As shown by the ACE-FTS, the power output of the laser goes down with increasing operational time and can cause hindrance to the overall health of the system [130] [143]. Hence, to keep a continuous check on the health of the IFTS system, it is recommended to read and store the analog signal from the ACU.

- For better lifetime and performance, it is recommended that the Helium-Neon laser be replaced by a diode laser. ACE-FTS uses a Distributed Feedback Laser (DFL) diode [130] [143]. A similar kind of diode centred close to a He-Ne laser can be used to work under vacuum conditions.

- More studies are required to replace the white light lamp on the modulator with similar spectral and mechanical characteristics, but a longer lifetime is recommended to increase the overall operational lifetime of the complete system.

- A more powerful microcontroller is recommended for future development with a faster clock which can read the FR90 signals' both edges, in addition, to performing all the tasks as mentioned in Table 24 to detect any back peddling of the modulator arm. Also, this can replace the CPC to store the data on an SD card and connect directly with a downlink module to talk to the ground base station directly for user interference for the flight configuration.

- It is also recommended to develop a variable gain setting algorithm to allow the user to change the detector's gain, according to a formula as a function of time or to change autonomously depending upon the scene.

- More studies are required to develop a redundancy routine both in hardware and software components to achieve better fault tolerance.

REFERENCES

[1]. Collins, M., Knutti, R., Arblaster, J., Dufresne, J.L., Fichefet, T., Friedlingstein, P., Gao, X., Gutowski, W.J., Johns, T., Krinner, G., and Shongwe, M., 2013. Long-term climate change: projections, commitments and irreversibility.

[2]. Schuur, E.A.G., McGuire, A.D., Schädel, C., Grosse, G., Harden, J.W., Hayes, D.J., Hugelius, G., Koven, C.D., Kuhry, P., Lawrence, D.M., and Natali, S.M., 2015. Climate change and the permafrost carbon feedback. *Nature*, *520*(7546), p.171

[3]. McGuire, A.D., Chapin Iii, F.S., Walsh, J.E., and Wirth, C., 2006. Integrated regional changes in arctic climate feedbacks: implications for the global climate system. *Annu. Rev. Environ. Resour.*, *31*, pp.61-91.

[4]. Bommareddi, R.R., 2014. Applications of optical interferometer techniques for precision measurements of changes in temperature, growth and refractive index of materials. *Technologies*, *2*(2), pp.54-75.

[5]. G. Singh, and C.T. McElroy. An Imaging Fourier Transform Spectrometer for Nadir Atmospheric Measurement. Earth and Space Science Colloquium, York University, Toronto, ON, presented on Jan 29, 2017.

[6]. G. Singh, Z. Vaziri, C.T. McElroy, D. Barton, G. Blair, and F.J. Grandmont. Optical Breadboard of An Imaging Fourier Transform Spectrometer (IFTS). Research Evaluation Course Conference, Department of Earth and Space Science, Lassonde School of Engineering, Toronto, ON, presented on May 15, 2017.

[7]. Mankins, J.C., 1995. Technology readiness levels. *White Paper, April*, *6*.

[8]. G. Singh, Z. Vaziri, C.T. McElroy, D. Barton, G. Blair, R. Siddiqui, and F.J. Grandmont. An Imaging Fourier Transform Spectrometer (IFTS). *CANDAC/PAHA workshop, Toronto, ON, (Talk, MSc. work),* May 8, 2017.

[9]. Aim-North mission homepage: http://aim-north.ca/.

[10]. Mariani, Z.H., 2014. *Infrared emission measurements of radiation and trace gas variability in the High Arctic* (Doctoral dissertation).

[11]. Walsh, R., and Wilber, K., 2010. *Integral theory in action: Applied, theoretical, and constructive perspectives on the AQAL model*. SUNY Press.

[12]. Key, J.R., Wang, X., and Liu, Y., 2013. Monitoring change in the Arctic. In *Satellite-based Applications on Climate Change* (pp. 127-149). Springer, Dordrecht.

[13]. Wolfe, W.L., 1997. *Introduction to imaging spectrometers* (Vol. 25). SPIE Press.

[14]. Schneider, F., and Berenbach, B., 2013. A literature survey on international standards for systems requirements engineering. *Procedia Computer Science*, *16*, pp.796-805.

[15]. Ma, Q., 1998. Greenhouse Gases: Refining the Role of Carbon Dioxide. *NASA Goddard Institute for Space Studies. http://www. giss. nasa. gov/research/intro/ma*, *1*.

[16]. Change, I.P.O.C., 2007. Climate change 2007: The physical science basis. *Agenda*, *6*(07), p.333.

[17]. Change, C., 2013. The Physical Science Basis. Intergovernmental Panel on Climate Change.

[18]. Lacis, A.A., Schmidt, G.A., Rind, D., and Ruedy, R.A., 2010. Atmospheric CO2: Principal control knob governing Earth's temperature. *Science*, *330*(6002), pp.356-359.

[19]. Li, H., Sheffield, J., and Wood, E.F., 2010. Bias correction of monthly precipitation and temperature fields from Intergovernmental Panel on Climate Change AR4 models using equidistant quantile matching. *Journal of Geophysical Research: Atmospheres*, *115*(D10).

[20]. *Vaclav Smil, 2003. The Earth's Biosphere: Evolution, Dynamics, and Change. MIT Press. p. 107. ISBN 978-0-262-69298-4.*

[21]. Wiedmann, T., and Minx, J., 2008. A definition of 'carbon footprint'. *Ecological economics research trends*, *1*, pp.1-11.

[22]. Petit, J.R., Jouzel, J., Raynaud, D., Barkov, N.I., Barnola, J.M., Basile, I., Bender, M., Chappellaz, J., Davis, M., Delaygue, G., and Delmotte, M., 1999. Climate and atmospheric history of the past 420,000 years from the Vostok ice core, Antarctica. *Nature*, *399*(6735), p.429.

[23]. Intergovernmental Panel on Climate Change, 2015. *Climate change 2014: Mitigation of climate change* (Vol. 3). Cambridge University Press.

[24]. Kunzig, R., 2013. Climate Milestone: Earth's CO2 level passes 400 ppm. *National Geographic News*.

[25]. Kahn, B., 2017. We just breached the 410 ppm threshold for CO2. *Scientific American*.

[26]. https://www.esrl.noaa.gov/gmd/ccgg/trends/full.html.

[27]. https://ourworldindata.org/co2-and-other-greenhouse-gas-emissions#note-2.

[28]. http://cdiac.ornl.gov/.

[29]. Lüthi, D., Le Floch, M., Bereiter, B., Blunier, T., Barnola, J.M., Siegenthaler, U., Raynaud, D., Jouzel, J., Fischer, H., Kawamura, K., and Stocker, T.F., 2008. High-resolution carbon dioxide concentration record 650,000–800,000 years before present. *Nature*, *453*(7193), p.379.

[30]. Boden, T.A., Andres, R.J., and Marland, G., 2013. *Global, Regional, and National Fossil-Fuel CO2 Emissions (1751-2010)(V. 2013)*. Carbon Dioxide Information Analysis Center (CDIAC), Oak Ridge National Laboratory (ORNL), Oak Ridge, TN (United States).

[31]. Change, I.P.O.C., 2014. IPCC. *Climate change*

[32]. Stern, N., and Taylor, C., 2010. *What do the Appendices to the Copenhagen Accord tell us about global greenhouse gas emissions and the prospects for avoiding a rise in global average temperature of more than 2 C?*. Centre for Climate Change Economics and Policy.

[33]. https://ourworldindata.org/co2-and-other-greenhouse-gas-emissions#note-2.

[34]. https://www.metoffice.gov.uk/hadobs/hadcrut4/index.html.

[35]. Cicerone, R.J., and Oremland, R.S., 1988. Biogeochemical aspects of atmospheric methane. *Global biogeochemical cycles*, *2*(4), pp.299-327.

[36]. Migeotte, M.V., 1948. Spectroscopic evidence of methane in the earth's atmosphere. *Physical Review*, *73*(5), p.519.

[37]. Matthews, E., and Fung, I., 1987. Methane emission from natural wetlands: Global distribution, area, and environmental characteristics of sources. *Global biogeochemical cycles*, *1*(1), pp.61-86.

[38]. Wunch, D., Wennberg, P.O., Toon, G.C., Keppel-Aleks, G., and Yavin, Y.G., 2009. Emissions of greenhouse gases from a North American megacity. *Geophysical Research Letters*, *36*(15).

[39]. Bousquet, P., Ciais, P., Miller, J.B., Dlugokencky, E.J., Hauglustaine, D.A., Prigent, C., Van der Werf, G.R., Peylin, P., Brunke, E.G., Carouge, C., and Langenfelds, R.L., 2006.

Contribution of anthropogenic and natural sources to atmospheric methane variability. *Nature*, *443*(7110), p.439.

[40]. Myhre, G., Highwood, E.J., Shine, K.P., and Stordal, F., 1998. New estimates of radiative forcing due to well mixed greenhouse gases. *Geophysical research letters*, *25*(14), pp.2715-2718.

[41]. Crutzen, P.J., 1995. On the role of CH 4 in atmospheric chemistry: sources, sinks and possible reductions in anthropogenic sources. *Ambio*, *24*(1), pp.52-55.

[42]. Rasmussen, R. A., and Khalil, M.A.K. (1981). Atmospheric methane (CH_4): Trends and seasonal cycles. Journal of Geophysical Research. 86, 9826-9832.

[43]. Blake, D.R., and Rowland, F.S. (1988). Continuing worldwide increase in tropospheric methane, 1978 to 1987. Science. 239, 1129-1131.

[44]. Steele, L., Dlugokencky, E, Lang, P., Tans, P., Martin, R., and Masarie, K. (1992). Slowing down of the global accumulation of atmospheric methane during the 1980s. Nature. 358, 313-316.

[45]. Dlugokencky, E., Masaire, K., Lang, P., Tans, P., Steele, L., and Nisbet, E. (1994b). A dramatic decrease in the growth rate of atmospheric methane in the northern hemisphere during 1992. Geophysical Research Letters. 21, 45-48.

[46]. Dlugokencky, E., Steele, L.P., Lang, P., and Masarie, K. (1995). Atmospheric methane at Mauna Loa and Barrow observatories: Presentation and analysis of in situ measurements. Journal of Geophysical Research. 100, 23103-23113.

[47]. Dlugokencky, E., Masarie, K., Lang, P., and Tans, P. (1998). Continuing decline in the growth rate of the atmospheric methane burden. Nature. 393, 447-450.

[48]. Khalil, M.A.K., and Rasmussen, R.A. (1985). Causes of increasing atmospheric methane: Depletion of hydroxyl radicals and the rise of emissions. Atmospheric Environment. 13, 397-407.

[49]. Lelieveld, J., Crutzen, P., and Bruhl, C. (1993). Climate effects of atmospheric methane. Chemosphere. 26, 739-767.

[50]. Etheridge, D.M., Steele, L., Francey, R.J., and Langenfelds, R.L., 1998. Atmospheric methane between 1000 AD and present: Evidence of anthropogenic emissions and climatic variability. *Journal of Geophysical Research: Atmospheres*, *103*(D13), pp.15979-15993.

[51]. Christensen, T.R., Prentice, I.C., Kaplan, J., Haxeltine, A., and Sitch, S., 1996. Methane flux from northern wetlands and tundra: an ecosystem source modelling approach. *Tellus B*, *48*(5), pp.652-661.

[52]. Potter, C.S., Davidson, E.A., and Verchot, L.V., 1996. Estimation of global biogeochemical controls and seasonality in soil methane consumption. *Chemosphere*, *32*(11), pp.2219-2246.

[53]. Bronson, K.F., and Mosier, A.R., 1993. Nitrous oxide emissions and methane consumption in wheat and corn-cropped systems in northeastern Colorado. *Agricultural ecosystem effects on trace gases and global climate change*, (agriculturaleco), pp.133-144.

[54]. https://wilderness.org/sites/default/files/TWS%20Methane%20Emissions%20Policy%20Report.pdf

[55]. Legrand, M., Feniet-Saigne, C., and Petit, J.R., 1990. Atmospheric Chemistry Changes Over The Last Climatic Cycle (180 000 Years) Inferred From The Vostok (Antarctica) Ice-Core Study. *Annals of Glaciology*, *14*, pp.344-344.

[56]. Etheridge, D.M., Pearman, G.I., and Fraser, P.J., 1992. Changes in tropospheric methane between 1841 and 1978 from a high accumulation-rate Antarctic ice core. *Tellus B*, *44*(4), pp.282-294.

[57]. Etheridge, D.M., Steele, L., Francey, R.J., and Langenfelds, R.L., 1998. Atmospheric methane between 1000 AD and present: Evidence of anthropogenic emissions and climatic variability. *Journal of Geophysical Research: Atmospheres*, *103*(D13), pp.15979-15993.

[58]. Jouzel, J., Barkov, N.I., Barnola, J.M., Bender, M., Chappellaz, J., Genthon, C., Kotlyakov, V.M., Lipenkov, V., Lorius, C.R.P.J., Petit, J.R., and Raynaud, D., 1993. Extending the Vostok ice-core record of palaeoclimate to the penultimate glacial period. *Nature*, *364*(6436), p.407.

[59]. Nakazawa, T., Machida, T., Tanaka, M., Fujii, Y., Aoki, S., and Watanabe, O., 1993. Differences of the atmospheric CH4 concentration between the Arctic and Antarctic regions in pre-industrial/pre-agricultural era. *Geophysical Research Letters*, *20*(10), pp.943-946.

[60]. Raynaud, D., Jouzel, J., Barnola, J.M., Chappellaz, J., Delmas, R.J., and Lorius, C., 1993. The ice record of greenhouse gases. *Science*, pp.926-934.

[61]. Blunier, T., Chappellaz, J., Schwander, J., Stauffer, B., and Raynaud, D., 1995. Variations in atmospheric methane concentration during the Holocene epoch. *Nature*, *374*(6517), p.46.

[62]. Blunier, T., Chappellaz, J., Schwander, J., Dällenbach, A., Stauffer, B., Stocker, T.F., Raynaud, D., Jouzel, J., Clausen, H.L., Hammer, C.U., and Johnsen, S.J., 1998. Asynchrony of Antarctic and Greenland climate change during the last glacial period. *Nature*, *394*(6695), p.739.

[63]. Brook, E.J., Sowers, T. and, Orchardo, J., 1996. Rapid variations in atmospheric methane concentration during the past 110,000 years. *Science*, *273*(5278), pp.1087-1091.

[64]. Petit, J.R., Jouzel, J., Raynaud, D., Barkov, N.I., Barnola, J.M., Basile, I., Bender, M., Chappellaz, J., Davis, M., Delaygue, G., and Delmotte, M., 1999. Climate and atmospheric history of the past 420,000 years from the Vostok ice core, Antarctica. *Nature*, *399*(6735), p.429.

[65]. Petit, J.R., Jouzel, J., Raynaud, D., Barkov, N.I., Barnola, J.M., Basile, I., Bender, M., Chappellaz, J., Davis, M., Delaygue, G., and Delmotte, M., 1999. Climate and atmospheric history of the past 420,000 years from the Vostok ice core, Antarctica. *Nature*, *399*(6735), p.429.

[66]. Brook, E.J., Sowers, T., and Orchardo, J., 1996. Rapid variations in atmospheric methane concentration during the past 110,000 years. *Science*, *273*(5278), pp.1087-1091.

[67]. Chappellaz, J., Bluniert, T., Raynaud, D., Barnola, J.M., Schwander, J., and Stauffert, B., 1993. Synchronous changes in atmospheric CH4 and Greenland climate between 40 and 8 kyr BP. *Nature*, *366*(6454), p.443.

[68]. Petit, J.R., Jouzel, J., Raynaud, D., Barkov, N.I., Barnola, J.M., Basile, I., Bender, M., Chappellaz, J., Davis, M., Delaygue, G., and Delmotte, M., 1999. Climate and atmospheric history of the past 420,000 years from the Vostok ice core, Antarctica. *Nature*, *399*(6735), p.429.

[69]. Blunier, T., Chappellaz, J.A., Schwander, J., Barnola, J.M., Desperts, T., Stauffer, B., and Raynaud, D., 1993. Atmospheric methane, record from a Greenland ice core over the last 1000 year. *Geophysical Research Letters*, *20*(20), pp.2219-2222.

[70]. Chappellaz, J.A., Fung, I.Y., and Thompson, A.M., 1993. The atmospheric CH4 increase since the Last Glacial Maximum. *Tellus B: Chemical and Physical Meteorology*, *45*(3), pp.228-241.

[71]. Raynaud, D., Chappellaz, J., Barnola, J.M., Korotkevich, Y.S., and Lorius, C., 1988. Climatic and CH4 cycle implications of glacial–interglacial CH4 change in the Vostok ice core. *Nature*, *333*(6174), p.655.

[72]. Ramanathan, V., 1988. The radiative and climatic consequences of the changing atmospheric composition of trace gases. *The changing atmosphere*, pp.159-186.

[73]. Key, J.R., Wang, X., and Liu, Y., 2013. Monitoring change in the arctic. In *Satellite-based Applications on Climate Change* (pp. 127-149). Springer, Dordrecht.

[74]. Manabe, S., Spelman, M.J., and Stouffer, R.J., 1992. Transient responses of a coupled ocean-atmosphere model to gradual changes of atmospheric CO2. Part II: Seasonal response. *Journal of Climate*, *5*(2), pp.105-126.

[75]. Manabe, S., and Stouffer, R.J., 1994. Multiple-century response of a coupled ocean-atmosphere model to an increase of atmospheric carbon dioxide. *Journal of climate*, *7*(1), pp.5-23.

[76]. Miller, J.R., and Russell, G.L., 2000. Projected impact of climate change on the freshwater and salt budgets of the Arctic Ocean by a global climate model. *Geophysical Research Letters*, *27*(8), pp.1183-1186.

[77]. Meehl, G.A., and Washington, W.M., 1990. CO 2 climate sensitivity and snow-sea-ice albedo parameterization in an atmospheric GCM coupled to a mixed-layer ocean model. *Climatic Change*, *16*(3), pp.283-306.

[78]. Curry, J.A., Schramm, J.L., Rossow, W.B., and Randall, D., 1996. Overview of Arctic cloud and radiation characteristics. *Journal of Climate*, *9*(8), pp.1731-1764.

[79]. http://blogs.ei.columbia.edu/2018/01/11/thawing-permafrost-matters/

[80]. Zhang, T., Barry, R.G., Knowles, K., Heginbottom, J.A., and Brown, J., 1999. Statistics and characteristics of permafrost and ground-ice distribution in the Northern Hemisphere. *Polar Geography*, *23*(2), pp.132-154.

[81]. Schuur, E.A.G., McGuire, A.D., Schädel, C., Grosse, G., Harden, J.W., Hayes, D.J., Hugelius, G., Koven, C.D., Kuhry, P., Lawrence, D.M. and Natali, S.M., 2015. Climate change and the permafrost carbon feedback. *Nature*, *520*(7546), p.171.

[82]. McGuire, A.D., Chapin Iii, F.S., Walsh, J.E., and Wirth, C., 2006. Integrated regional changes in arctic climate feedbacks: implications for the global climate system. *Annu. Rev. Environ. Resour.*, *31*, pp.61-91.

[83]. Chadburn, S.E., Burke, E.J., Cox, P.M., Friedlingstein, P., Hugelius, G., and Westermann, S., 2017. An observation-based constraint on permafrost loss as a function of global warming. *Nature Climate Change*, *7*(5), p.340.

[84]. Hugelius, G., Strauss, J., Zubrzycki, S., Harden, J.W., Schuur, E.A.G., Ping, C.L., Schirrmeister, L., Grosse, G., Michaelson, G.J., Koven, C.D., and O'Donnell, J.A., 2014. Estimated stocks of circumpolar permafrost carbon with quantified uncertainty ranges and identified data gaps. *Biogeosciences Discussions*, *11*.

[85]. Tarnocai, C., Canadell, J.G., Schuur, E.A.G., Kuhry, P., Mazhitova, G., and Zimov, S., 2009. Soil organic carbon pools in the northern circumpolar permafrost region. *Global biogeochemical cycles*, *23*(2).

[86]. McGuire, A.D., Hayes, D.J., Kicklighter, D.W., Manizza, M., Zhuang, Q., Chen, M., Follows, M.J., Gurney, K.R., McClelland, J.W., Melillo, J.M., and Peterson, B.J., 2010. An analysis of the carbon balance of the Arctic Basin from 1997 to 2006. *Tellus B: Chemical and Physical Meteorology*, *62*(5), pp.455-474.

[87]. Schuur, E.A.G., McGuire, A.D., Schädel, C., Grosse, G., Harden, J.W., Hayes, D.J., Hugelius, G., Koven, C.D., Kuhry, P., Lawrence, D.M., and Natali, S.M., 2015. Climate change and the permafrost carbon feedback. *Nature*, *520*(7546), p.171.

[88]. Stocker, T. ed., 2014. *Climate change 2013: the physical science basis: Working Group I contribution to the Fifth assessment report of the Intergovernmental Panel on Climate Change*. Cambridge University Press.

[89]. Popp, T.J., Chanton, J.P., Whiting, G.J., and Grant, N., 2000. Evaluation of methane oxidation in therhizosphere of a Carex dominated fen in northcentral Alberta, Canada. *Biogeochemistry*, *51*(3), pp.259-281.

[90]. Schuur, E.A., Bockheim, J., Canadell, J.G., Euskirchen, E., Field, C.B., Goryachkin, S.V., Hagemann, S., Kuhry, P., Lafleur, P.M., Lee, H., and Mazhitova, G., 2008. Vulnerability of permafrost carbon to climate change: Implications for the global carbon cycle. *AIBS Bulletin*, *58*(8), pp.701-714.

[91]. Dutrieux, P., Vaughan, D.G., Corr, H.F., Jenkins, A., Holland, P.R., Joughin, I., and Fleming, A.H., 2013. Pine Island glacier ice shelf melt distributed at kilometre scales. *The Cryosphere*, *7*, pp.1543-1555.

[92]. McGuire, A.D., Anderson, L.G., Christensen, T.R., Dallimore, S., Guo, L., Hayes, D.J., Heimann, M., Lorenson, T.D., Macdonald, R.W., and Roulet, N., 2009. Sensitivity of the carbon cycle in the Arctic to climate change. *Ecological Monographs*, *79*(4), pp.523-555.

[93]. O'Connor, F.M., Boucher, O., Gedney, N., Jones, C.D., Folberth, G.A., Coppell, R., Friedlingstein, P., Collins, W.J., Chappellaz, J., Ridley, J., and Johnson, C.E., 2010. Possible role of wetlands, permafrost, and methane hydrates in the methane cycle under future climate change: A review. *Reviews of Geophysics*, *48*(4).

[94]. Tarnocai, C., Canadell, J.G., Schuur, E.A.G., Kuhry, P., Mazhitova, G., and Zimov, S., 2009. Soil organic carbon pools in the northern circumpolar permafrost region. *Global biogeochemical cycles*, *23*(2).

[95]. Schuur, E.A., Bockheim, J., Canadell, J.G., Euskirchen, E., Field, C.B., Goryachkin, S.V., Hagemann, S., Kuhry, P., Lafleur, P.M., Lee, H., and Mazhitova, G., 2008. Vulnerability of permafrost carbon to climate change: Implications for the global carbon cycle. *AIBS Bulletin*, *58*(8), pp.701-714.

[96]. Friborg, T., Soegaard, H., Christensen, T.R., Lloyd, C.R., and Panikov, N.S., 2003. Siberian wetlands: Where a sink is a source. *Geophysical research letters*, *30*(21).

[97]. Wille, C., Kutzbach, L., Sachs, T., Wagner, D., and PFEIFFER, E.M., 2008. Methane emission from Siberian arctic polygonal tundra: eddy covariance measurements and modeling. *Global Change Biology*, *14*(6), pp.1395-1408.

[98]. http://blogs.ei.columbia.edu/2018/01/11/thawing-permafrost-matters

[99]. Robbins, A., 2016. How to understand the results of the climate change summit: Conference of Parties21 (COP21) Paris 2015.

[100]. Xu, X., Wang, J., Wang, Y., Zeng, J., Torres, O., Yang, Y., Marshak, A., Reid, J., and Miller, S., 2017. Passive remote sensing of altitude and optical depth of dust plumes using the oxygen A and B bands: First results from EPIC/DSCOVR at Lagrange-1 point. *Geophysical Research Letters*, *44*(14), pp.7544-7554.

[101]. Geddes, A.G., 2015. *Development of a Fabry-Perot Etalon spectrometer for high-resolution aerosol observations in the oxygen A-band* (Doctoral dissertation, Department of Physics and Astronomy).

[102]. Heidinger, A.K., and Stephens, G.L., 2000. Molecular line absorption in a scattering atmosphere. Part II: Application to remote sensing in the O2 A band. *Journal of the Atmospheric Sciences*, *57*(10), pp.1615-1634.

[103]. Baron, J., Campbell, W.C., DeMille, D., Doyle, J.M., Gabrielse, G., Gurevich, Y.V., Hess, P.W., Hutzler, N.R., Kirilov, E., Kozyryev, I., and O'Leary, B.R., 2013. Order of magnitude smaller limit on the electric dipole moment of the electron. *Science*, p.1248213.

[104]. Banwell, C.N., and McCash, E.M., Fundamentals of molecular spectroscopy, 1994.

[105]. Lambert, J.H., 1760. *Photometria sive de mensura et gradibus luminis, colorum et umbrae*. Klett.

[106]. Beer, A., 1852. Bestimmung der absorption des rothen lichts in farbigen flussigkeiten. *Ann. Physik*, *162*, pp.78-88.

[107]. Dirac, P.A.M., 1927. The quantum theory of the emission and absorption of radiation. *Proc. R. Soc. Lond. A*, *114*(767), pp.243-265.

[108]. Weisskopf, V., and Wigner, E.P., 1930. Calculation of the natural lineshape based on Dirac's quantum theory of light. *Z. Phys.*, *63*, p.54.

[109]. Hippler, M., Miloglyadov, E., Quack, M., and Seyfang, G., 2011. Mass and isotope-selective infrared spectroscopy. *Handbook of High-Resolution Spectroscopy*, pp.1069-1118.

[110]. Albert, S., Albert, K.K., and Quack, M., 2011. High-resolution Fourier transform infrared spectroscopy. *Handbook of High-resolution Spectroscopy*.

[111]. Doppler, J.C., 1842. Versuch einer das Bradley'sche aberrations-theorem als integrirrenden Theil in sich schlissenden allgemeineren Theorie. *Prag: In Commission bei Borrosch and Andre*, pp.465-466.

[112]. Huang, K., 1987. Statistical Mechanics, 2nd. *Edition (New York: John Wiley & Sons)*.

[113]. Albert, S., Albert, K.K., and Quack, M., 2011. High-resolution Fourier transform infrared spectroscopy. *Handbook of High-resolution Spectroscopy*.

[114]. Niederer, J.M., 2012. *The infrared spectrum of methane*. ETH Zurich.

[115]. Frankenberg, C., Warneke, T., Butz, A., Aben, I., Hase, F., Spietz, P., and Brown, L.R., 2008. Pressure broadening in the 2v_3 band of methane and its implication on atmospheric retrievals. *Atmospheric chemistry and physics*, *8*(17), pp.5061-5075.

[116]. Bernath, P.F., 2015. *Spectra of atoms and molecules*. Oxford university press.

[117]. Rothman, L.S., Jacquemart, D., Barbe, A., Benner, D.C., Birk, M., Brown, L.R., Carleer, M.R., Chackerian Jr, C., Chance, K., Coudert, L.E.A., and Dana, V., 2005. The HITRAN 2004 molecular spectroscopic database. *Journal of Quantitative Spectroscopy and Radiative Transfer*, *96*(2), pp.139-204.

[118]. Chartier, G., 2005. *Introduction to optics*. Springer Science & Business Media.

[119]. Saptari, V., 2003. *Fourier transform spectroscopy instrumentation engineering*. Bellingham Washington, DC: SPIE Optical Engineering Press.

[120]. Papoulis, A., and Pillai, S.U., 2002. *Probability, random variables, and stochastic processes*. Tata McGraw-Hill Education.

[121]. Yaglom, A.M., 1987. Introduction. In *Correlation theory of stationary and related random functions* (pp. 1-13). Springer, New York, NY.

[122]. Roy, S.A., 2008. Data processing pipelines tailored for imaging Fourier-transform spectrometers.

[123]. Roy, S.A., Potvin, S., Genest, J., and Desbiens, R., 2007. Fast line-shape correction procedure for imaging Fourier-transform spectrometers. *Applied optics*, *46*(21), pp.4674-4679.

[124]. Kretschmer, E., 2014. Modelling of the instrument spectral response of conventional and imaging Fourier transform spectrometers.

[125]. Kretschmer, E., 2014. Modelling of the instrument spectral response of conventional and imaging Fourier transform spectrometers.

[126]. Genest, J., and Tremblay, P., 2005. Modeling the instrument line shape of Fourier-transform spectrometers within the framework of partial coherence. *Applied optics*, *44*(19), pp.3912-3924.

[127]. Genest, J.E., and Tremplay, P., 2010. Understanding Fourier-transform spectrometers. *Centre d'optique, photonique et laser, Université Laval*, *20017*.

[128]. Bernath, P.F., 2017. The Atmospheric Chemistry Experiment (ACE). *Journal of Quantitative Spectroscopy and Radiative Transfer*, *186*, pp.3-16.

[129]. Bernath, P.F., McElroy, C.T., Abrams, M.C., Boone, C.D., Butler, M., Camy-Peyret, C., Carleer, M., Clerbaux, C., Coheur, P.F., Colin, R., and DeCola, P., 2005. Atmospheric chemistry experiment (ACE): mission overview. *Geophysical Research Letters*, *32*(15).

[130]. Chateauneuf, F., Fortin, S., Frigon, C., and Soucy, M.A.A., 2002, September. ACE-FTS test results and performances. In *Earth Observing Systems VII* (Vol. 4814, pp. 82-91). International Society for Optics and Photonics.

[131]. Drissen, L., Bernier, A.P., Charlebois, M., Alarie, A., Grandmont, F., and Mandar, J., 2011. Imaging Fourier transform spectroscopy for astronomy. In *Fourier Transforms-New Analytical Approaches and FTIR Strategies*. InTech.

[132]. Drissen, L., Bernier, A.P., Charlebois, M., Alarie, A., Grandmont, F., and Mandar, J., 2011. Imaging Fourier transform spectroscopy for astronomy. In *Fourier Transforms-New Analytical Approaches and FTIR Strategies*. InTech.

[133]. Friedl-Vallon, F., Gulde, T., Hase, F., Kleinert, A., Kulessa, T., Maucher, G., Neubert, T., Olschewski, F., Piesch, C., Preusse, P., and Rongen, H., 2014. Instrument concept of the imaging Fourier transform spectrometer GLORIA. *Atmospheric measurement techniques*, *7*(10), pp.3565-3577.

[134]. Flasar, F.M., Kunde, V.G., Abbas, M.M., Achterberg, R.K., Ade, P., Barucci, A., Bézard, B., Bjoraker, G.L., Brasunas, J.C., Calcutt, S., and Carlson, R., 2004. Exploring the Saturn system in the thermal infrared: The composite infrared spectrometer. In *The Cassini-Huygens Mission* (pp. 169-297). Springer, Dordrecht.

[135]. Scoville, N.Z., Hall, D.N.B., Kleinmann, S.G., and Ridgway, S.T., 1979. Detection of CO band emission in the Becklin-Neugebauer object. *The Astrophysical Journal*, *232*, pp.L121-L124.

[136]. Ridgway, S.T., and Brault, J.W., 1984. Astronomical Fourier transform spectroscopy revisited. *Annual review of astronomy and astrophysics*, *22*(1), pp.291-317.

[137]. Chalabaev, A.A. and Maillard, J.P., 1985. Near-infrared spectroscopy of Gamma Cassiopeiae-Constraints on the velocity field in the envelope. *The Astrophysical Journal*, *294*, pp.640-645.

[138]. Maillard, J.P., Crovisier, J., Encrenaz, T., and Combes, M., 1988. The spectrum of comet P/Halley between 0.9 and 2.5 microns. In *Exploration of Halley's Comet* (pp. 398-404). Springer, Berlin, Heidelberg.

[139]. Maillard, J.P., and Simons, D., 1992. ESO Conf. On Progress in Telescope and Instrumentation Technologies.

[140]. Paumard, T., Maillard, J.P., and Morris, M., 2004. Kinematic and structural analysis of the Minispiral in the Galactic Center from BEAR spectro-imagery. *Astronomy & Astrophysics*, *426*(1), pp.81-96.

[141]. Qian, S.E. ed., 2015. *Optical payloads for space missions*. John Wiley & Sons.

[142]. http://www.ace.uwaterloo.ca/instruments_acefts.php.

[143]. https://www.slideserve.com/awena/ace-fts-instrument-after-7-5-years-on-orbit

[144]. http://www.ace.uwaterloo.ca/instruments_acefts.php

[145]. Bernath, P.F., 2006. Atmospheric chemistry experiment (ACE): Analytical chemistry from orbit. *TrAC Trends in Analytical Chemistry*, *25*(7), pp.647-654.

[146]. Qian, S.E. ed., 2015. *Optical payloads for space missions*. John Wiley & Sons.

[147]. Bertaux, J.L., Kyrölä, E., Fussen, D., Hauchecorne, A., Dalaudier, F., Sofieva, V., Tamminen, J., Vanhellemont, F., d'Andon, O.F., Barrot, G., and Mangin, A., 2010. Global ozone monitoring by occultation of stars: an overview of GOMOS measurements on ENVISAT. *Atmospheric Chemistry and Physics*, *10*(24), pp.12091-12148.

[148]. Bernath, P.F., McElroy, C.T., Abrams, M.C., Boone, C.D., Butler, M., Camy-Peyret, C., Carleer, M., Clerbaux, C., Coheur, P.F., Colin, R., and DeCola, P., 2005. Atmospheric chemistry experiment (ACE): mission overview. *Geophysical Research Letters*, *32*(15).

[149]. Bernath, P.F., 2006, July. Atmospheric Chemistry Experiment (ACE): Mission Status. In *Atmospheric Science Conference*(Vol. 628).

[150]. Kuze, A., Suto, H., Nakajima, M., and Hamazaki, T., 2009. Thermal and near infrared sensor for carbon observation Fourier-transform spectrometer on the Greenhouse Gases Observing Satellite for greenhouse gases monitoring. *Applied optics*, *48*(35), pp.6716-6733.

[151]. Saitoh, N., Kimoto, S., Sugimura, R., Imasu, R., Kawakami, S., Shiomi, K., Kuze, A., Machida, T., Sawa, Y., and Matsueda, H., 2016. Algorithm update of the GOSAT/TANSO-FTS thermal infrared CO 2 product (version 1) and validation of the UTLS CO 2 data using CONTRAIL measurements. *Atmospheric Measurement Techniques*, *9*(5), pp.2119-2134.

[152]. Saitoh, N., Imasu, R., Ota, Y., and Niwa, Y., 2009. CO2 retrieval algorithm for the thermal infrared spectra of the Greenhouse Gases Observing Satellite: Potential of retrieving CO2 vertical profile from high-resolution FTS sensor. *Journal of Geophysical Research: Atmospheres*, *114*(D17).

[153]. Tasumi, M. ed., 2014. *Introduction to experimental infrared spectroscopy: Fundamentals and practical methods*. John Wiley & Sons.

[154]. Norton, P., 2002. HgCdTe infrared detectors. *Optoelectronics review*, (3), pp.159-174.

[155]. http://www.eorc.jaxa.jp/GOSAT/instrument_1.html

[156]. https://spie.org/publications/tt61_121_dispersive_spectrometers

[157]. Chapter 1, Vidi Saptari, Fourier transform spectroscopy instrumentation engineering.

[158]. Shepherd, G.G., 2002. *Spectral imaging of the atmosphere* (Vol. 82). Academic press.

[159]. Hanel, R.A., Conrath, B.J., Jennings, D.E., and Samuelson, R.E., 2003. *Exploration of the solar system by infrared remote sensing*. Cambridge University Press.

[160]. Hecht, E., 2002. Optics (Addision Wesley, San Francisco). *Chap*, *10*, p.500.

[161]. Voutsogiannakis, M., 2017. Calibration and Flight of a Balloon-Borne O2 Atmospheric Band Fabry-Perot Spectrometer.

[162]. Johnston, S.F., 2001. In search of space: Fourier spectroscopy 1950–1970. In *Instrumentation between Science, State and Industry* (pp. 121-141). Springer, Dordrecht.

[163]. G. Singh, C.T. McElroy, Z. Vaziri, D. Barton, G. Blair, and F.J. Grandmont. Optical Bench Breadboard Of An Imaging Fourier Transform Spectrometer (IFTS) For Climate Observations.Lassonde *Undergraduate Research Conference. Lassonde School of Engineering, York University, Toronto, ON,* August 11, 2017.

[164]. Saptari, V., 2003. *Fourier transform spectroscopy instrumentation engineering*. Bellingham Washington, DC: SPIE Optical Engineering Press.

[165]. https://www.newport.com/p/RS4000-48-12

[166]. http://www.minusk.com/products/bm10-small-vibration-isolation-platforms.html

[167]. https://www.lasos.com/products/lasos-he-ne-laser-series/

[168]. http://www.gilway.com/

[169]. https://www.edmundoptics.com/resources/application-notes/optics/all-about-aspheric-lenses/

[170]. Bely, P. ed., 2006. *The design and construction of large optical telescopes*. Springer Science & Business Media.

[171]. Qian, S.E. ed., 2015. *Optical payloads for space missions*. John Wiley & Sons.

[172]. Russell, C.T. ed., 2013. *The Cassini-Huygens Mission: Volume 1: Overview, Objectives and Huygens Instrumentarium*. Springer Science & Business Media.

[173]. Kleipool, Q.L., Jongma, R.T., Gloudemans, A.M.S., Schrijver, H., Lichtenberg, G.F., van Hees, R.M., Maurellis, A.N., and Hoogeveen, R.W.M., 2007. In-flight proton-induced radiation damage to SCIAMACHY's extended-wavelength InGaAs near-infrared detectors. *Infrared physics & technology*, *50*(1), pp.30-37.

[174]. Bentell, J., Vermeiren, J., Verbeke, P., de Kerckhove, A., Rodriguez, L., Colin, T., and Grietens, B., 2010, November. 3000-pixel linear InGaAs sensor for the Proba-V satellite. In *Earth Observing Missions and Sensors: Development, Implementation, and Characterization* (Vol. 7862, p. 786206). International Society for Optics and Photonics.

[175]. G Singh, Z. Vaziri, C.T. McElroy, D. Barton, G. Blair, R. Siddiqui, and F.J. Grandmont. *At CANDAC/PAHA workshop, Toronto, ON*, presented on May 1, 2018.

[176]. https://os.mbed.com/platforms/FRDM-K64F/.

[177]. G. Singh, C.T. McElroy, D.V Barton, Z. Vaziri, and C. Zheng. *Payload for Remote Sounding of Atmosphere Using Balloon Limb Experiments*. Lassonde Undergraduate Research Conference. Lassonde School of Engineering, York University, Toronto, ON presented on August 18, 2015.

[178]. Personal communication, 2017, Zahra Vaziri, PhD candidate, Earth and Space Science and Engineering, York University.

[179]. Nakajima, M., Suto, H., Kuze, A., and Shiomi, K., 2015. Optical Payloads onboard Japanese Greenhouse Gases Observing Satellite. *Optical Payloads for Space Missions*, p.459.

[180]. Hibbitts, C.A., Bauer, J., Bernasconi, P., Clarke, J., Domingue, D., Emery, J., Gladstone, R., Greathouse, T., Hansen, G., Harris, W., and Hendrix, A., Stratospheric Balloon Missions for Planetary Science: A Petition for the Formation of.

[181]. ISO, M., 2011. *Systems and software engineering–architecture description* (pp. 1-46). ISO/IEC/IEEE 42010.

[182]. Booch, G., 2005. *The unified modeling language user guide*. Pearson Education India.

[183]. Saptari, V., 2004. *Fourier transform spectroscopy instrumentation engineering* (Vol. 61). SPIE press.

[184]. Wang, Y.-C., Shyu, L.-H., and Chang, C.-P. The Comparison of Environmental Effects on Michelson and Fabry-Perot Interferometers Utilized for the Displacement Measurement. *Sensors* 2010, *10*, 2577-2586.

[185]. Jacquinot, P. Proceedings of the 17th Congress du Gaurs CNRS (Paris),1954

[186]. http://www.xenics.com/sites/default/files/leaflets/xb-003_06_xeva-1.7-320_rd_lowres.pdf

[187]. Bruce C. Kindel, Zheng Qu, and Alexander F. H. Goetz, "Direct solar spectral irradiance and transmittance measurements from 350 to 2500 nm," Appl. Opt. 40, 3483-3494 (2001)

Appendix I: Absorption spectroscopy details

Line shape profiles

Dirac [107] derived the quantum theory of the emission and absorption of radiation while Weisskopf [108] discussed the shapes of spectral lines.

Natural broadening – Lorentzian and Voigt line shape

The classical motion of a driven damped oscillator gives the first approximation of line shape for a transition at $\tilde{\nu}_0$. Alternatively, for a general derivation, for the Einstein coefficient, A = k which corresponds to the exponential rate constant of spontaneous decay in the time domain, its spectral decomposition (Fourier transform) produces an exact Lorentzian line shape. This can be interpreted by the equations 2.2 and 2.3 [108]:

$$\sigma_{\mathrm{n}}(\widetilde{\nu}) = \sigma(\widetilde{\nu}_0)\mathcal{F}\left((k/4)\exp\left(-k|t|/2\right)\right) * \mathcal{F}\left(\exp\left(2\pi i\widetilde{\nu}_0 ct\right)\right) \tag{2.2}$$

$$= \sigma(\widetilde{\nu}_0)\frac{(\Delta\widetilde{\nu}_{\mathrm{n}}/2)^2}{\widetilde{\nu}^2 + (\Delta\widetilde{\nu}_{\mathrm{n}}/2)^2} * \delta(\widetilde{\nu} - \widetilde{\nu}_0) \tag{2.3}$$

where,

- $\sigma_n(\tilde{\nu})$ = natural absorption cross section
- $\tilde{\nu}_0$ = resonance wavenumber
- $\sigma_n(\tilde{\nu}_0)$ = maximum cross section
- $\Delta\tilde{\nu}_n$ = full width at half maximum
- k = 2. π.c. $\Delta\tilde{\nu}_n$ [109]

In equation 2.2, and 2.3 the convolution with the Dirac delta function shifts the Lorentzian to $\tilde{\nu}_0$. The rate constant of the respective physical process defines the natural line width $\Delta\tilde{\nu}_n$ whereas in resonance the wavenumber defines the Doppler width $\Delta\tilde{\nu}_D$.

Doppler broadening – Gaussian line shape

The Doppler effect adjusts the spectral line shape due to the thermal Maxwell-Boltzmann distribution of molecular translational velocities relative to the radiation field. Figure 64 illustrates the thermal distribution of velocities of atoms and molecules on the line shape broadening for an isotropic sample [110].

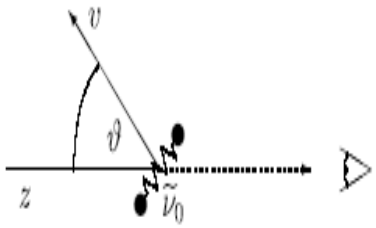

Figure 64: Relative motion of sample gives rise to a relative shift to the resonance wavenumber $\tilde{\nu}_0$ [110]

The observed line shape is independent of the observation direction z due to spatial isotropy. The classical Doppler effect [111] for |v| << c, causing the relativistic wavenumber shift is given by equation (2.4):

$$\tilde{\nu} = \tilde{\nu}_0 \left(1 + \frac{|v| \cos\vartheta}{c}\right), \tag{2.4}$$

where,

c = speed of light in vacuum
$\tilde{\nu}$ = observed resonance wavenumber of the molecule
$\tilde{\nu}_0$ = resonance wavenumber of the molecule at rest

The probability density ρ(ν̃) of the observed molecule can be calculated by using the Maxwell-Boltzmann energy distribution [112]. It is essentially a normalized Gaussian which is centred at $\tilde{\nu}_0$ and has the full width at half maximum $\Delta\tilde{\nu}_D$. The Gaussian line profile is given by 2.5:

$$g_D(\tilde{\nu} - \tilde{\nu}_0) = \frac{1}{\sqrt{a\pi}} \exp\left(-\frac{(\tilde{\nu} - \tilde{\nu}_0)^2}{a^2}\right) \tag{2.5}$$

where,

$$a = \frac{\tilde{\nu}_0}{c}\sqrt{\frac{2k_B T}{m}}$$

T = temperature [K]
m = mass of molecule [atomic mass unit]

Equation 2.5 shows that at lower temperatures the Doppler width is also reduced. As such, for samples at low pressure, Doppler broadening is a dominant contributor to HR-FTIR spectroscopy.

Collisional broadening

The collisions of molecules 'A' with inert gaseous solvent molecules or atoms' result in collisional line widths which are related to a pseudo-first-order rate constant for collisions [114]. The exact calculation of the thermally averaged collision cross section (σ_{AM}) does not have a trivial solution and depending on the collision partners its values can range over several orders of magnitudes. To a first estimate, a collision between inert partners results in pressure proportional line width. Thus, collisional broadening effects are usually negligible for pressures below 1 hPa, except sometimes for larger and dipolar molecules [115]. The Lorentzian line profile is given by equation 2.6:

$$g_L(\tilde{\nu} - \tilde{\nu}_0) = \frac{1}{\pi}\frac{\Delta\tilde{\nu}_L}{(\tilde{\nu} - \tilde{\nu}_0 - \delta_L)^2 + (\Delta\tilde{\nu}_L)^2} \quad (2.6)$$

where,

$\tilde{\nu}_0$ = line centre at zero pressure

δ_L = line position shift parameter

$\Delta\tilde{\nu}_L$ = line width parameter = $\Delta\nu_L(T,p) = \left(\frac{T_0}{T}\right)^{n_{air}} \left[\gamma_{air}(T_0,p_0)(p-p_s) + \gamma_{self}(T_0,p_0)p_s\right]$.

where,

T = temperature

T_0 = reference temperature = 296 K

p = pressure

p_0 = reference pressure = 1 atm

p_s = partial pressure of the gas which absorbs the radiation at wavenumber $\tilde{\nu}$

γ_{air} = air broadening coefficient measured at the reference

γ_{self} = self-broadening coefficient

Combined natural, Doppler, and pressure broadening – Voigt line shape

The convolution of Lorentz broadening line shape and Doppler broadening line shape results in the Voigt line profile. The general form is given by equation 2.7 [116]:

$$g_V(\tilde{\nu}-\tilde{\nu}_0) = \int_{-\infty}^{+\infty} g_D(\tilde{\nu}_0'-\tilde{\nu}_0)\, g_L(\tilde{\nu}-\tilde{\nu}_0')\, d\tilde{\nu}_0' \,. \tag{2.7}$$

Voigt line profile is widely used in many retrieval techniques in atmospheric remote sounding. Line parameter such as $\Delta\tilde{\nu}_0$, γ_{air}, γ_{self}, δ_{air}, and n_{air} measured by many groups are archived in the High-resolution TRANsmission (HITRAN) database [117].

Appendix II: A Quantitative overview of Fourier transform spectroscopy

The Fourier transform spectrometer indirectly measures the spectrum of observed light by measuring its autocorrelation. The measured autocorrelation is called the interferogram and the spectra are obtained through its Fourier transform. The Einstein-Weiner-Khinchin theorem [120] establishes the link between the autocorrelation function and the spectrum. This theorem suggests that for a wide-sense stationary random process whose mean and autocorrelation functions are time-invariant, the power spectral density is given by the Fourier transform of the autocorrelation function [121]. By using this theorem an estimate of the optical source spectrum can be retrieved by applying a Fourier transform with respect to the OPD on the interferogram. For a monochromatic source, the ideal interferogram measured with a photodetector is calculated by equation 2.8:

$$I_0(X) = I_0 \cos(2\pi\sigma_0 X) \tag{2.8}$$

where,

X = OPD [cm]

σ_0 = wave number [cm^{-1}]

For a true polychromatic source with power spectral density of the interferogram is calculated by equation (2.9):

$$I_0(X) = \int_0^\infty S(\sigma) \cos(2\pi\sigma_0 X)\, d\sigma_0 \tag{2.9}$$

Above equation 2.9 also represents the cosine transform of a signal symmetric around zero path difference (ZPD) between the two mirrors.

Since the true spectrum $S_0(\sigma_0)$ is real, the cosine transform and the complex Fourier transform are equivalent. Thus, the true interferogram which represents the physical quantity measured by a perfect instrument can be written as by equation 2.10:

$$I_0(X) = T_{cos}\{(S_0(\sigma_0)\} = T_{TF}\{(S_0(\sigma_0)\} \tag{2.10}$$

The Fourier inverse of the equation 2.9 gives the spectrum. It can be written as the equation 2.11:

$$S(\sigma) = \int_{-\infty}^{\infty} I(X)\, exp(-i2\pi\sigma\, X_0)\, d\sigma_0 \tag{2.11}$$

I is the measured interferogram which includes optical and electronic distortions. The apparent spectrum of the scene is obtained by Fourier transforming the measured interferogram over all OPDs. To bring all the spectral energy into the real part of the spectrum, processes such as phase correction may be performed [122]. Now, considering the finite distance travelled by the mirrors on either side of the ZPD, the spectrum can be written as equation 2.12:

$$\hat{S}(\sigma) = \int_{-MPD}^{+MPD} I(X)\, exp(-i2\pi\sigma\, X_0)\, dX \tag{2.12}$$

Where +/- MPD represents the Maximum Path Difference (MPD) on either side of the ZPD. The interferogram gets truncated by the mirror motion at +/- MPD rather than spanning to +/- ∞. In other words, the infinitely spanning interferogram is multiplied with a rectangular window of width 2MPD. In the spectral domain, it is equivalent to convolving the apparent spectrum with a sinc function (equation 2.13) leads to equation 2.13

$$\mathrm{sinc}(\mathrm{x}) = \frac{\sin(\pi x)}{\pi x}, \tag{2.13}$$

$$S(\sigma) = S(\sigma) * 2MPDsinc(\sigma 2MPD), \tag{2.14}$$

The maximum achievable spectral resolution is limited by interferogram truncation. This can be proved in the following way:

$$\Delta\nu * \Delta t = 1 \tag{2.15}$$

where,

$\Delta\nu$ = frequency resolution and

Δt = time difference between first and last wavefront interacting with the interferometer during a single scan

This implies:

$$\Delta\nu = \frac{1}{\Delta t} = \frac{c}{Xo} \tag{2.16}$$

$$\text{But,} \quad \tilde{\nu} = \frac{1}{\lambda} \quad \Rightarrow \quad |\Delta\tilde{\nu}| = \frac{\Delta\lambda}{\lambda^2} \tag{2.17}$$

$$\text{also,} \quad \lambda = \frac{c}{\nu} \quad \Rightarrow \quad |\Delta\lambda| = \frac{c * \Delta\nu}{\nu^2} \tag{2.18}$$

from (2.16) and (2.18):

$$|\Delta\lambda| = \frac{c * c}{\nu^2 * Xo} = \frac{c^2}{\nu^2 * Xo} \tag{2.19}$$

$$\text{But } \nu = \frac{c}{\lambda} \quad \Rightarrow \quad |\Delta\lambda| = \frac{c^2 * \lambda^2}{c^2 * Xo} = \frac{\lambda^2}{Xo} \tag{2.20}$$

from (2.17) and (2.20)

$$|\Delta\tilde{\nu}| * \lambda^2 = \frac{\lambda^2}{\mathrm{Xo}} \quad \Rightarrow \quad |\Delta\tilde{\nu}| = \frac{1}{Xo} \tag{2.21}$$

Therefore, an interferometer with greater OPD provides a better spectral resolution. As a result, the finite value of OPD distorts the measurements made by the instrument defining the instrument line shape (ILS). The ILS represents the apparent spectrum of a monochromatic source as measured by the FTS and normalizing it by the power received at the true wavenumber [123].

Off-axis effect on wavelength

Equation 2.30 implies that the wavenumber perceived by the interferometer is a factor of cos θ, where θ is the propagation angle of input light through the spectrometer with respect to the principal axis. Figure 65 and Figure 66 represent the cosine behaviour in detected wavenumbers experienced by pixels on the FPA.

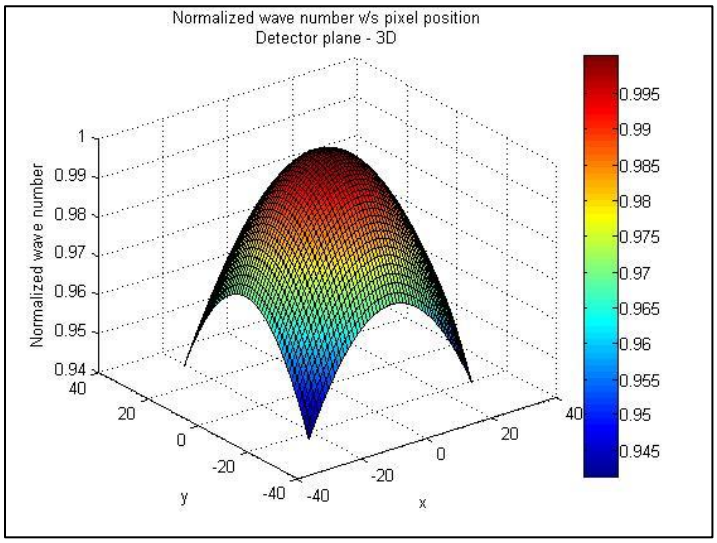

Figure 65: 3D illustration of normalized wavenumber versus pixel position on the detector plane.

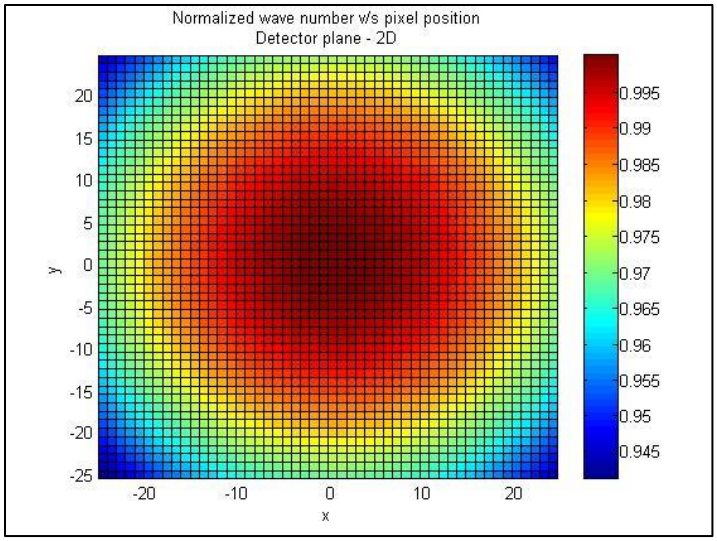

Figure 66: 2D Illustration of normalized wavenumber versus pixel position on the detector plane.

The effective focal length of the focusing lens at a wavelength of 762 nm is 99.9279 mm. If the centre pixel records a wavelength of 762.000 nm, then the last pixel in horizontal dimension records a wavelength of 762.916 nm (or 13107.61 cm^{-1}) with a normalization factor of 0.9988. Similarly, in the vertical direction, the last pixel records a wavelength of 762.534 nm (or 13114.17 cm^{-1}) with a normalization factor of 0.9993

The effective focal length at the wavelength of 1600.000 nm is 102.236 mm. If the centre pixel records a wavelength of 1600.000 nm, then the last pixel in horizontal dimension records a wavelength of 1601.762 nm (or 6243.125 cm^{-1}) with a normalization factor of 0.9989. In the vertical direction, the last pixel records a wavelength of 1601.121 nm (or 6245.625 cm^{-1}) with a normalization factor of 0.9993.

Summary of these effects is given in Table 15:

Table 15: Summary of off-axis effects on detected wavelength.

Centre wavelength	Focal length	Last horizontal pixel	Last vertical pixel

		wavelength	wavelength
762.000 nm (or 13123.36 cm^{-1})	99.9279 mm	762.916 nm (or 13107.61 cm^{-1}) (factor = 0.9988)	762.534 nm or 13114.17 cm^{-1} (factor = 0.9993)
1600.000 nm (or 6250 cm^{-1})	102.236 mm	1601.762 nm or 6243.125 cm^{-1} (factor = 0.9989)	1601.121 nm or 6245.625 cm^{-1} (factor = 0.9993)

Off-axis effects on resolution

From Figure 17 in chapter 2, wavefront at an angle θ has a path difference of $\Delta X_o \cos\theta$, where ΔX_o is the maximum optical path difference. Therefore,

$$X_0(\theta) = \Delta X_o \cos\theta \qquad 3.1$$

From equation (2.21):

$$|\Delta\tilde{\nu}| = \frac{1}{\Delta X_o * \cos\theta} \qquad 3.2$$

Therefore, the resolution of wavenumber perceived by each pixel is also varied as cos θ. Table 16 outlines the values of spectral resolution using the equation:

Table 16: Summary of off-axis effects on spectral resolution.

Centre wavelength	Focal length	Central OPD	Central resolution	Last horizontal pixel OPD	Last horizontal pixel resolution	Last vertical pixel OPD	Last vertical pixel resolution
762.000 nm (or 13123.36 cm^{-1})	99.9279 mm	2.000 cm	0.50 cm^{-1}	1.9976 cm (factor = 0.9988)	0.50 cm^{-1}	1.9986 cm (factor = 0.9993)	0.50 cm^{-1}
1600.000 nm (or 6250 cm^{-1})	102.236 mm	2.000 cm	0.50 cm^{-1}	1.9978 cm (factor = 0.9989)	0.50 cm^{-1}	1.9986 cm (factor = 0.9993)	0.50 cm^{-1}

Therefore, within the scope of the instrument, the resolution does not really change with the off-axis effect.

Appendix III: Longitudinal mode spacing of metrology laser

Calculating the frequency of basic longitudinal mode by using equation (1):

$$v_{1L} = \frac{c}{2nL} \tag{3.1}$$

where,

v_{1L} = Frequency of basic longitudinal mode

L= Length of laser cavity = 231.5 mm

n = Index of refraction = 1

c = speed of light = 3×10^8 m/s

Therefore, using equation (3.1)

$$v_{1L} = \frac{3*10^8}{2*1*0.2315} = 0.648 \text{ GHz} \tag{3.2}$$

Calculating m^{th} mode using equations (2a) and (2b):

$$\lambda_m = \frac{2L}{m} \tag{3.3}$$

$$m = \frac{2L}{\lambda_m} \tag{3.4}$$

where,

λ_m = wavelength at mode at m = 0.6328×10^{-6} m (3.5)

and at $(m+1)^{th}$ mode, the lasing wavelength = $\frac{2L}{m+1}$ = 0.6325 X 10^{-6} m (3.6)

Appendix IV: List of hardware interfaces

Table 17: List of hardware interfaces.

Serial number	Input component	Input connector	Output component	Output connector
IFTS-CAS-HI-10	Microcontroller	RS232 (TBC)	Control PC	RS232 (TBC)
IFTS-CAS-HI-20	Control PC	RS232 (TBC)	Microcontroller	RS232 (TBC)
IFTS-CAS-HI-30	ABB Control Box	RJ45	Control PC	RJ45
IFTS-CAS-HI-40	Control PC	RJ45	ABB Control Box	RJ45
IFTS-CAS-HI-50	Line Conditioner	BNC	ABB Control Box	BNC
IFTS-CAS-HI-60	Driver1	Pin-plug	Microcontroller	Pin-plug
IFTS-CAS-HI-70	Camera 762	Customized	Driver1	BNC
IFTS-CAS-HI-80	Driver2	Pin-plug	Microcontroller	Pin-plug
IFTS-CAS-HI-90	Camera 1600	Customized	Driver2	BNC
IFTS-CAS-HI-100	PC1	RS232 (TBC)	Microcontroller	RS232 (TBC)
IFTS-CAS-HI-110	Microcontroller	RS232 (TBC)	PC1	RS232 (TBC)
IFTS-CAS-HI-120	PC2	RS232 (TBC)	Microcontroller	RS232 (TBC)
IFTS-CAS-HI-130	Microcontroller	RS232 (TBC)	PC2	RS232 (TBC)
IFTS-CAS-HI-140	ABB Control Unit	Pin-plug	White light source-detector	Pin-plug
IFTS-CAS-HI-150	ABB Control Unit	Pin-plug	Metrology laser detector	Pin-plug

Appendix V: Mass budget

Table 18 below is intended as the first cut at weight allocation for York IFTS. The allocation includes the contingencies above the best estimate. For the computers (CPC, CAM762PC, and CAM1600PC), the weight of only Central Processing Unit (CPU) is included since other peripherals such as monitor, mouse, keyboard, etc. will not be a part of the flight package.

Table 18: Itemized weight allocation for York IFTS

Serial number	Component	Weight (kg) (approximate)	% of the total weight (approximate)
1.	Modulator + base plate	20	24
2.	ACU	15	18
3.	Minus-K vibration isolator	32	38
4.	Electronics board	1	1
5.	CAM762	2	2
6.	CAM1600	2	2
7.	Control PC	5	6
8.	CAM762PC	3	4
9.	CAM1600PC	3	4
10.	Cables	2	2
	Total	85	100

Therefore, the instrument weighs about 85 kilograms with the vibration isolator contributes the most, closely followed by the modulator.

Appendix VI: Power budget

Table 19 provides an estimate of the power consumption of the individual components of the instrument during the scan state (section 4.2.1.3.2).

Table 19: Itemized power allocation for York IFTS

Serial number	Component	Power [W] (approximate)	% of total power (approximate)
1.	Modulator + ACU	65	35
2.	Minus-K vibration isolator	0	0
3.	Electronics board	1	0.5
4.	CAM762	30	16
5.	CAM1600	30	16
6.	Control PC	20	10.8
7.	CAM762PC	20	10.8
8.	CAM1600PC	20	10.8
	Total	186	100

Therefore, the instrument needs about 186 W of power for nominal operations with modulator and ACU consuming 35% and all three computers taking up about 32% of the power supplied to the IFTS.

Appendix VII: Optical budget

Angular field of view.

Note: This section assumes the height of a high-altitude stratospheric balloon to be 36 km and height of geostationary satellite to be 36,000 km from Earth's surface for Nadir view.

Therefore, using basic trigonometry, the following relationship can be derived by equations (3.7), (3.8) and equation (3.12):

$$AFOV(degrees) = 2\,arctan\left(\frac{h}{2f}\right) \tag{3.7}$$

for h = width of detector active area (diagonal of the square), and
f = focal length

Case 1.1: (0.762 µm channel):

$$AFOV\ (degrees) = 2\,arctan\left(\frac{30\sqrt{2}\times 10^{-6}}{2 * 99.9279 \times 10^{-3}}\right) \tag{3.8}$$

$$= 2.433 \text{ X } 10^{-2} \text{ (degrees)}$$

where,

f = 99.9279 mm

For direct-Sun:

angular diameter, or AFOV required = 0.545 degrees

this implies

h = 0.95 mm ~ 0.67 mm edge square ~ 23 pixels of 30 µm edge. (3.9)

For high-altitude stratospheric balloon:

height = 36 km

Therefore, diagonal of a spatial element from a height of the stratospheric balloon

$$= 36X10^{3} \text{ X } \tan (2.433 \text{ X } 10^{-2})^{o}$$

= 15.29 m. or a square of edge 10.8 m (3.10)

For geostationary orbit:

Height = 36,000 km = 36 X 10^6 m

Therefore, diagonal of a spatial element from a height of geostationary orbit

= 36X10^6 X tan (2.433 X 10^{-2}) ^{o}

= 1.529 X 10^4 m or a square of edge 1.081 X 10^4 m or

~ 10.8 km (3.11)

Case 1.2: (1.6 µm channel)

$$AFOV\ (degrees) = 2\ arctan\left(\frac{30\sqrt{2}\times 10^{-6}}{2 * 102.236\times 10^{-3}}\right) \quad (3.12)$$

= 2.378 X 10^{-2} (degrees)

where,

f = 102.236 mm

For direct-Sun:

angular diameter, or AFOV required = 0.545 degrees

this implies

h = 0.97 mm ~ 0.69 mm edge square ~ 23 pixels of 30 µm edge. (3.13)

For high-altitude stratospheric balloon:

height = 36 km

Therefore, diagonal of a spatial element from a height of the stratospheric balloon

= 36X10^3 X tan (2.378 X 10^{-2}) ^{o}

= 14.94 m. or a square of edge 10.6 m (3.14)

For geostationary orbit:

height = 36,000 km = 36 X 10^6 m

Therefore, diagonal of a spatial element from a height of geostationary orbit

= 36X10^3 X tan (2.378 X 10^{-2}) ^{o} (3.15)

= 1.494 X 10^4 m or a square of edge 1.057 X 10^4 m or

~ 10.6 km (3.16)

Throughput (Tput):

The York IFTS does not use any collimating foreoptics, therefore the optical system is limited by the (size of) the detector element. Hence for Jaquinot advantage as discussed in section 2.8.2.1,

this section uses a formula (equation 3.17) with the area of detector element and the f-number of the focusing element:

Case 2.1: (0.762 µm channel)

Using Zemax optic studio 16.5 software and simulating only the 0.762 µm as the primary wavelength:

Clear Aperture (Collimation) - Aspheric Side diameter: 47.0 mm

Focal length: 99.9279 mm

F-number (using paraxial approximation) = $\frac{99.9279\ \text{mm}}{47.0\ \text{mm}}$ (3.17)

= 2.13

Hence, throughput can be calculated by using equation (3.17):

$$T_{put} = A_{det} \times \frac{\pi/4}{F_n^2} \tag{3.18}$$

where,

T_{put} = detector throughput

A_{det} = Area of detector

F_n = f-number

T_{put} for a single pixel is calculated by equation (3.18):

$$(30\ \mu m \times 30\ \mu m) \times \left(\frac{\frac{\pi}{4}}{(2.13^2)}\right) \tag{3.19}$$

= 1.56X10^{-4} sr-mm^2

T_{put} for 23X23 pixels (active throughput) is calculated by equation (3.18):

$$(0.69 \times 0.69\ mm^2) \times \left(\frac{\frac{\pi}{4}}{(2.13^2)}\right) \tag{3.20}$$

= 0.082 sr – mm^2

T_{put} for 320X256 pixels is calculated by equation (3.18):

$$(73.7\ mm^2) \times \left(\frac{\frac{\pi}{4}}{(2.13^2)}\right) \tag{3.21}$$

= 12.8 sr – mm^2

Therefore, equations 5a, 5b, and 5c imply that the throughput for single pixel, active pixels, and 320X256 pixels for 762 nm channel is 1.56X10^{-4} sr-mm^2, 0.082 sr-mm^2, and 12.8 sr-mm^2 respectively.

Case 2.2: (1.600 µm channel)

Using Zemax optic studio 16.5 software and simulating only the 1.600 µm wavelength as the primary:

Clear Aperture (Collimation) - Aspheric Side diameter: 47.0 mm

Focal length: 102.236 mm

F-number (using paraxial approximation) = $\frac{102.236\ mm}{47.0\ mm}$ (3.22)

= 2.18

Hence, throughput using the same formula from equation 5 is as follows:

T_{put} for a single pixel is calculated by equation (3.18):

$$(30\ \mu m \times 30 \mu m) \times \left(\frac{\frac{\pi}{4}}{(2.18^2)}\right) \quad (3.23)$$

= 1.49E-4 sr – mm^2

T_{put} for 23X23 pixels (active throughput) is calculated by equation (3.18):

$$(0.69 \times 0.69\ mm^2) \times \left(\frac{\frac{\pi}{4}}{(2.18^2)}\right) \quad (3.24)$$

= 0.079 sr – mm^2

T_{put} for 320X256 pixels is calculated as follows:

$$(73.7\ mm^2) \times \left(\frac{\frac{\pi}{4}}{(2.18^2)}\right) \quad (3.25)$$

12.2 sr–mm^2

Therefore, equations 6a, 6b, and 6c imply that the throughput for single pixel, active pixels, and 320X256 pixels for 1600 nm channel is 1.49X10^{-4} sr-mm^2, 0.079 sr-mm^2, and 12.2 sr-mm^2 respectively.

Quantum Efficiency (QE)

Quantum efficiency is the photon-to-electron conversion efficiency of a photoelectric detector.

Calculating the quantum efficiency of Xenics Xeva detector:

For e = charge per electron

= 1.6E-19 C or

1.6E-19 C/s is current per electron

which implies,

1 C/s = 1 A

$= \left(\frac{1}{1.6E-19}\right)$ = 6.2E18 electrons/s (3.26)

Sensitivity = 1A/W

The formula for energy is given by equation (3.27):

$$\mathrm{E} = \frac{h * c}{\lambda} \quad (3.27)$$

where,

E = Energy

h = Planck's constant = 6.63E-34 J-s

c = speed of light = 3.0E8 m/s

λ = wavelength = 0.762 µm and 1.600 µm

Case 3.1: (0.762 µm channel)

By using Eq. (3.27), the energy for 0.762 µm is 2.6E-19 J/photon

which implies,

1 J = (1/2.6E-19) (3.28)

= 3.8E18 photons or

1 W = 3.8E18 photons/s.

Therefore, (3.29)

the quantum efficiency = 1A/W

$= \left(\frac{6.2E18\ electrons/s}{3.8E18\ photons/s}\right)$

= 1.6 electrons/photon (3.30)

Case 3.2: (1.600 µm channel)

By using Eq. (3.27), the energy for 1.600 µm is 1.2E-19 J/photon

which implies,

1 J = $\left(\frac{1}{1.2E-19}\right)$

= 8.3E18 photons or

1W = 8.3E18 photons/s. (3.31)

Therefore,

the quantum efficiency = 1A/W

$= (\frac{6.2E18\ electrons/s}{8.3E18\ photons/s})$

= 0.75 electrons/photon (3.32)

Henceforth, the results imply that the detector generates 1.6 and 0.75 electrons per photon for wavelengths 762 nm and 1600 nm, respectively.

The rate of Photons Arrival (RPA):

The IFTS registers incoming energy in the counts of photons. These photons stimulate the detector which records this data in the allocated memory in binary units. While observing Sun, this energy varies with different spectral regions. The R_{PA} can be calculated by using equation (3.36)

Solar irradiance at 762 nm = 0.58787 W/m^2/nm [187]
Solar irradiance at 1600 nm = 0.20784 W/m^2/nm [187]

$$\text{The solid angle formed by the lens is: } \left(\frac{\frac{\pi}{4}}{(F-number)^2}\right) \tag{3.33}$$

$$\text{For 0.762 µm channel: } \left(\frac{\frac{\pi}{4}}{(2.13^2)}\right) = 0.17 \text{ sr} \tag{3.34}$$

$$\text{For 1.6 µm channel: } \left(\frac{\frac{\pi}{4}}{(2.18^2)}\right) = 0.17 \text{ sr} \tag{3.35}$$

$$R_{PA} = I_e \times T_{put} \times \lambda \tag{3.36}$$

for
R_{PA} = Rate of Photons Arrival (photons/s)
I_e = Solar irradiance
T_{put} = Throughput
λ = Wavelengths

Case 4.1: (0.762 µm channel):

At 0.762 µm channel in the bandpass of 0.5 cm^{-1}, the rate of photons arrivals is calculated as shown below at three different regions:

For single pixel, using equation 3.36:

$$R_{PA} = (0.58787 \text{ W/m}^2\text{/nm}) \times (1.56\text{E-}4 \text{ sr- mm}^2) \times (2.90\text{E-}2 \text{ nm}) \times (3.8\text{E}18 \text{ photons/s/W}) = 1.01\text{E}7 \text{ photons/s} \tag{3.37}$$

for a rate of 200 Hz sampling implies:

$$(1.01\text{E}7 \text{ photons/s}) \times (200) = 2.02\text{E}9 \text{ photons/s.} \tag{3.38}$$

at Quantum Efficiency of 1.6 electrons/photon implies:

$$(2.02\text{E}9 \text{ photons/s}) \times (1.6 \text{ electrons/photon}) = 3.23\text{E}9 \text{ electrons/s} \tag{3.39}$$

Similarly, for active area (23 X 23 pixels), using equation 3.36:

R_{PA} = (0.58787 W/m^2/nm) × (0.082 sr – mm^2) × (2.90E-2 nm) × (3.8E18 photons/s/W) (3.40)
= 5.31E9 photons/s

for a rate of 200 Hz sampling implies:

(5.31E9 photons/s) × (200) = 1.06E12 photons/s. (3.41)

at Quantum Efficiency of 1.6 electrons/photon implies:

(1.06E12 photons/s) × (1.6 electrons/photon) = 1.70E12 electrons/s. (3.42)

Similarly, for 320 X 256 pixels, using equation 3.36:

R_{PA} = 0.58787 W/m^2/nm) × (73.7 sr – mm^2) × (2.90E-2 nm) × (3.8E18 photons/s/W) (3.43)
= 4.77E12 photons/s

for a rate of 200 Hz sampling implies:

(4.77E12 photons/s) × (200) = 9.54E14 photons/s. (3.44)

at Quantum Efficiency of 1.6 electrons/photon implies:

(9.54E14 photons/s) *(1.6 electrons/photon) = 1.53E15 electrons/s (3.45)

Case 4.2: (1.6 µm channel):

At 1.6 µm channel in the bandpass of 0.5 cm^{-1}, the rate of photons arrivals is calculated as shown below at three different regions:

For single pixel, using equation 3.36:

(0.20784 W/m^2/nm) *(1.49E-4 sr – mm^2) *(1.28E-1 nm) *(8.3E18 photons/s/W) (3.46)
= 3.29E7 photons/s

for a rate of 100 Hz sampling implies:

(3.29E7 photons/s) *(100) = 3.29E9 photons/s (3.47)

at Quantum Efficiency of 0.75 electrons/photon implies:

(3.29E9 photons/s) *(0.75 electrons/photon) = 2.47E9 electrons/s (3.48)

Similarly, for active area (23 X 23 pixels), using equation 3.36:

R_{PA} = (0.20784 W/m^2/nm) *(0.079 sr – mm^2) *(1.28E-1 nm) *(8.3E18 photons/s/W) (3.49)
= 1.74E10 photons/s

for a rate of 100 Hz sampling implies:

(1.74E10 photons/s) *(100) = 1.74E12 photons/s (3.50)

at Quantum Efficiency of 0.75 electrons/photon implies:

(1.74E12 photons/s) *(0.75 electrons/photon) = 1.30E12 electrons/s (3.51)

Similarly, for 320 X 256 pixels, using equation 3.36:

R_{PA} = (0.20784 W/m^2/nm) *(73.7 sr – mm^2) *(1.28E-1 nm) *(8.3E18 photons/s/W) (3.52)
= 1.63E13 photons/s

for a rate of 100 Hz sampling implies:

(1.63E13 photons/s) *(100) = 1.63E15 photons/s (3.53)

at Quantum Efficiency of 0.75 electrons/photon implies:

(1.63E15 photons/s) *(0.75 electrons/photon) = 1.22E15 electrons/s (3.54)

The time required for each scan

Case 5.1: (0.762 µm channel):

To sample a wavelength of 0.762 µm in a 2-cm path at the Nyquist frequency, number of sample points

$$= \left(\frac{2cm}{\left(\frac{0.762\ \mu m}{2} \right)} \right) = 52493 \text{ points.} \quad (3.55)$$

At 200 Hz, this will take $\left(\frac{52493}{200} \right) = 262.5$ s. (3.56)

For a double-sided interferogram, the time would be 262.5 × 2 = 525 seconds. (3.57)

Case 5.2: (1.600 µm channel):

To sample a wavelength of 1.6 µm in a 2-cm path at the Nyquist frequency, number of sample points

$$= \left(\frac{2\ cm}{\left(\frac{1.6\ \mu m}{2} \right)} \right) = 25000 \text{ points.} \quad (3.58)$$

At 100 Hz, this will take $\left(\frac{25000}{100} \right) = 250$ s. (3.59)

For a double-sided interferogram, the time would be 250 × 2 = 500 seconds. (3.60)

Case 5.3: (0.632 µm metrology laser):

To sample a wavelength of 0.632 µm in a 2-cm path at the Nyquist frequency, number of sample points

$$= \left(\frac{2\ cm}{\left(\frac{0.632\ \mu m}{2} \right)} \right) = 63291 \text{ points.} \quad (3.61)$$

At 100 Hz, this will take $\left(\frac{63291}{200} \right) = 316.5$ s. (3.62)

For a double-sided interferogram, the time would be 316.5 × 2 = 633 seconds. (3.63)

Appendix VIII: Setup Data File (SDF), Microcontroller (Freescale)

Table 20: SDF for microcontroller

Subsystem						Domain	Units	Typical Value
Microcontroller (Freescale)	MC	AS		AS	Arm Speed	[1,9999]	Hz	500
	MC	AR		AR	Resolution	{0.5,1,2,4,8, 16,32,64}	cm^{-1}	0.5
	MC	AT		AT	Total scans	[1,99999]		1000
	MC	AG		AG	GPS coordinates	[90.00,90.00], [90.00,90.00]	[N, S], [E, W]	43.65° N, 79.38° W

Appendix IX: Setup Data File (SDF), Channel-762

Table 21: SDF for channel-762

Subsystem				Domain	Units	Typical Value
CAM762PC	C7	IT		IT Integration Time	[0.025, 107374182.375]	us	500
	C7	SX		SX Start X pixel	[0,318]		0
	C7	EX		EX End X pixel	[1,319]		31
	C7	SY		SY Start Y pixel	[0,254]		0
	C7	EY		EY End Y pixel	[1,256]		31
	C7	ST		ST Set temperature	[-173.15, 76.85]	C	25
	C7	IX		IX Image extension	{.bin, .csv}		.bin
	C7	AG		AG GPS coordinates	[90.00,90.00], [90.00,90.00]	[N, S], [E, W]	43.65° N, 79.38° W

Appendix X: Setup Data File (SDF), Channel-1600

Table 22: Setup Data File entities for instrument

Subsystem				Domain	Units	Typical Value
CAM1600PC	C1	IT	IT Integration Time	[0.025, 107374182.375]	us	500
	C1	SX	SX Start X pixel	[0,318]		0
	C1	EX	EX End X pixel	[1,319]		31
	C1	SY	SY Start Y pixel	[0,254]		0
	C1	EY	SY End Y pixel	[1,256]		31
	C1	ST	ST Set temperature	[-173.15, 76.85]	C	25
	C1	IX	IX Image extension	{.bin, .csv}		.bin
	C1	AG	AG GPS coordinates	[90.00,90.00], [90.00,90.00]	[N, S], [E, W]	43.65° N, 79.38° W

Appendix XI: Failure detection, mitigation and recovery for York IFTS

Table 23: Failure detection, mitigation, and recovery for York IFTS

1.	Scenario	The bad ordering of FR/FR90
	Detection	During the perfect arm motion, for when SD=0 FR90 positive edge is followed by FR negative edge then FR90 negative edge. However, for when SD=1, after the FR positive edge, the FR90 negative edge occurs. Then the FR negative edge followed by the FR90 positive edge. Any failure from this perfect motion leads to this scenario.
	Action	Yellow flag
2.	Scenario	The ordering of FR/FR90 does not match SD
	Detection	During the perfect arm motion, for when SD=0 (see graph 2), FR90 positive edge is followed by FR negative edge then FR90 negative edge. However, for when SD=1 (see graph 1), after the FR positive edge, the FR90 negative edge occurs. Then the FR negative edge followed by the FR90 positive edge. Any failure from this perfect motion leads to this scenario.
	Action	Yellow flag
3.	Scenario	Timeout when searching for TA start.
	Detection	Running modulator at 0.5 cm^{-1}, implies that the maximum number of FR cycles in the entire Scan Window (SW) shall be less than 32754 ±1 or 33,000 for a round number. If the width of SW exceeds 38,000 FR cycles, it leads to this scenario.
	Action	Blinking red flag
4.	Scenario	Timeout when searching for SW start (or TA end)
	Detection	Freescale waits for 65 seconds maximum at arm speed of 500 Hz. If the SW does not become low after the turn around (SW = high) then start of SW has timed out.
	Action	Blinking red flag
5.	Scenario	Timeout when searching for SW end. This scenario is the same as failing to find the start of Turn Around.
	Detection	Running modulator at 0.5 cm^{-1}, implies that the maximum number of FR cycles in the entire Scan Window (SW) shall be less than 32754 ±1 or 33,000 for a round number. If the width of SW exceeds 38,000 FR cycles, it leads to this scenario.
	Action	Blinking red flag
6.	Scenario	ZPD not found
	Detection	Freescale is always reading the ZPD signal from ABB control box. ZPD must be detected at least once in each scan.
	Action	Yellow flag
7.	Scenario	SD not changing during TA (or between scans)

	Detection	Before the Turn Around ends, the SD should change its status.
	Action	Yellow flag
8.	Scenario	Min, max values of FR speed exceeded
	Detection	During the Scan, the microcontroller is always recording the mean and standard deviation of the FR cycle width. The flag is raised if the standard deviation is more than the pre-set value
	Action	Blinking red flag
9.	Scenario	Communication with ABB control box failed
	Detection	Freescale is always requesting the arm speed from ABB control box. A disrupted communication will not answer to the request.
	Action	Steady red flag
10.	Scenario	Accidental Keyboard hit
	Detection	The microcontroller is always looking for any information coming from the user through the CPC.
	Action	The microcontroller does not entertain any inputs by the user during the operations until the "Turn Around" state. It also searches for the key words that make up a command as stated in 4.1.3.2, anything other than the command, it ignores everything else. Refer to section 2.2.3. Also, Yellow flag.
11.	Scenario	Generic reset of the modulator
	Detection	The microcontroller is always talking with the ABB control unit to request the arm speed. If the modulator goes into generic reset, the arm speed is not as selected by the user but is 6000 Hz or 8000 Hz.
	Action	Blinking red flag
12.	Scenario	Temperature 1, temperature 2 exceeded
	Detection	The program on the camera PC records the temperature from the camera and is saved in the footer section of the IDF.
	Action	If the actual temperature of the camera exceeds more than ~10% [TBC] of the set temperature: Red flag
13.	Scenario	CAM762 goes offline
	Detection	On the GUI software provided by the camera manufacturer, it shows explicitly if the camera is online or offline. On the custom developed software, this feature can be kept and used organically.
	Action	Blinking red flag
14.	Scenario	CAM1600 goes offline
	Detection	On the GUI software provided by the camera manufacturer, it shows explicitly if the camera is online or offline. On the custom developed software, this feature can be kept and used organically.

	Action	Blinking Red flag
15.	Scenario	Communication between CAM762PC and CAM762
	Detection	If the number of images captured by CAM762 (channel 1) is “0”, this signifies that the communication between CAM762PC and CAM762 is disrupted.
	Action	Blinking Red flag
16.	Scenario	Communication between CAM1600PC and CAM
	Detection	If the number of images captured by CAM1600 (channel 2) is “0”, this signifies that the communication between CAM1600PC and CAM1600 is disrupted.
	Action	Blinking Red flag

Appendix XII: Tasks performed by the microcontroller (Freescale)

Table 24: Tasks performed during "Go" state

Priority level	Task performed
1.	Receive Setup Data File (SDF) from Control PC (CPC).
2.	Transfer operational parameters to CAM762PC and CAM1600PC.
3.	Send “set speed” to ABB Control Unit (ACU)
4.	Send “set resolution” to ABB Control Unit (ACU)
5.	Request “current speed” from ABB Control Unit (ACU)

Table 25: Tasks performed during "Scan" state

Priority level	Task performed
1.	Read FR from ABB Control Unit (ACU)
2.	Read SW from ABB Control Unit (ACU)
3.	Read SD from ABB Control Unit (ACU)
4.	Read ZPD from ABB Control Unit (ACU)
5.	Send trigger to CAM762 at every positive and negative FR edge
6.	Send trigger to CAM1600 at every positive FR edge
7.	Send Laser Data File (LDF) to CAM762
8.	Send Laser Data File (LDF) to CAM1600
9.	Send Laser Data File (LDF) to Control PC (CPC)
10.	Report FR cycle corresponding to the occurrence of ZPD
11.	Adjust PreCount and PostCount automatically to define by the acquisition window by keeping ZPD from ACU always in the middle of the window.
12.	Send “done” command to CPC and both camera PCs when acquisition ends.
13.	Keep checking the communication between the ABB Control Unit (ACU). Report and act accordingly if communication link breaks.
14.	Watch for generic reset of the modulator. Report it and act accordingly.
15.	Calculate and report width of the SW signal. (count number of FR cycles)
16.	Calculate and report mean of FR cycles
17.	Read FR90 from ABB Control Unit (ACU)
18.	Calculate and report the standard deviation of FR cycles
19.	Calculate and report mean of FR90 cycles
20.	Calculate and report the standard deviation of FR90 cycles
21.	Report if the ordering of FR and FR90 edges does not match with SD status

22.	Report synchronization status for FR and FR90 edges. (report number of good and bad cycles)

Table 26: Tasks performed during "Turn Around state"

Priority level	Task performed
1.	Receive the “Reset” command from CAM1600PC
2.	Receive the “Reset” command from CAM762PC
3.	Receive commands (operational parameters) from the user during Turn Around
4.	Receive Footer from CAM762 and transfer to Control PC (CPC)
5.	Receive Footer from CAM1600 and transfer to Control PC
6.	Calculate the width of Turn Around

Appendix XIII: Laser Data File entities

Table 27: Laser data file entities

Sr. #	Entity	Description	Units	Size (bytes)	Example
1.	Start of LDF title	The line stating the start of LDF		10	* * * L D F * * * ,
2.	TA1	Start, end and width of Turn around1	Time (us)	55	T U R N A R O U N D 1 S T A R T S : X X X X X X X X X U S ,
					E N D S :
					X X X X X X
					X X X U S ,
3.	Pre-counts	Counts between the start of Scan Window and the start of Acquisition Window.	FR Cycles and Time (us).	18	P R E C N T : X X C Y C L E S ,
4.	Post-Counts	Counts between the end of Acquisition Window and the end of Scan Window.	FR Cycles and Time (us).	19	P O S T C N T : X X C Y C L E S ,
5.	SW start	Start of the scan window. Scan window starts with the first positive edge of the FR signal when the SW signal is low.	FR cycles and time	48	S W S T A R T S : F R C Y C L E : # X X X X X ,
					T I M E : X
					X X X X X X
					X X U S ,
6.	SW ends	End of Scan window. Characterized by last FR edge when SW signal is still low.	FR cycles and time	46	S W E N D S : F R C Y C L E # X X X X X , T I M
					E : X X X
					X X X X X X U S ,
7.	SW width	Total width of Scan Window	FR Cycles and time	43	S W W I D T H : X X X X X F R C Y C L E
					S , T I M
					E : X X X
					X X X X X X ,
8.	AW	The total length of the Acquisition window.	FR Cycles and Time (us).	21	A W C N T : X X X X X

					CYCLES,
9.	Triggers1 aka triggers762	Total number of triggers sent by Freescale to the camera-762 during the Acquisition Window.	Integer value	26	CAMERA 762 TRIGS: XXXXX,
10.	Triggers2 aka triggers 1600	Total number of triggers sent by Freescale to the camera-1600 during the Acquisition Window.	Integer value	27	CAMERA 160 TRIGS: XXX,
11.	Coarse ZPD	Count corresponding to the high ZPD and its width.	FR Cycles and Time (us).	70	ZPD: FOUND CYCLE# XXX, TIME: XXXXXX TOTAL XXXXXX us) XXXX(XXXX),
12.	SD bit	High or low corresponding to the direction of modulator arm.	1 or 0	12	DIRECTION: X,
13.	Interrupt stats	Outputs mean and standard deviation of the FR and FR90 interrupts.		55	MEAN FRCYCLE: XXX.XXX, XXX STDEV: XXXX(XXXX),
14.	Noise spikes/disturbance	If Freescale sees an abnormality in the ABB signals, it records the corresponding cycle number for this event.	FR cycle	48	SYNC Hroog edge count: XXXXX, bad cycles: XXXXX,

15.	TA2	Start of Turn Around2.	Time (us)	35	T U R N A R O U N D 2 S T A R T S : **X** **X** **X** **X** **X** **X** **X** **X** **X** U S ,
16.	End of LDF	Line stating the ending of LDF		10	* * * D O N E * * *

Appendix XIV: Header entities for Instrument Data File (IDF)

Table 28: Header entities for IDF

	Entity	Description	Units	Size (bytes)	Example
1.	Scan ID	Represents scanth number of total scans		19	S C A N _ X X X X X X O F X X X X X ,
2.	Header size	The total length of the header before the SDF starts		3	X X ,
3.	Channel	Channel name or number for e.g.: channel 1 for 762 nm and channel 2 for 1600 nm		7	I D F X X X ,
4.	Date and Time	Represents date and time of the start of the creation of the file		13	Y Y M M D D h h m m s S ,

Appendix XV: Footer entities for Instrument Data File (IDF)

Table 29: Footer entities for IDF

Sr. #	Entity	Description	Units	Size (bytes)	Example
1.	Time stamp of "done command"			10	X X X X X X X X X ,
2.	Saturated number of frames	Number of frames that record maximum possible pixel value.			X X X X X ,
3.	Fine ZPD	Frame corresponding to ZPD (calculated spectrally)	FR cycles		X X X X X ,
4.	Low light frames	Number of frames that record minimum possible pixel value.			X X X X X ,
5.	Actual temperature reading of camera.				X X X . X X ,

Appendix XVI: MATLAB code for spectrum output

```
% Author: Gurpreet Singh, GurpreetSingh.YorkU@Gmail.com

% Laboratory for Atmospheric Remote Sounding from Space, York University.

% April 3, 2018


%% Sampling signal generation

 samp_period = 1*632.8/4*10^-7; % sampling period in cm. (632.8 nm is the wavelength of HeNe laser). Make 1*10^-7 for channel 2

 scan_dist = 1; % mirror scan distance in cm

 no_elements = floor(scan_dist/samp_period); % total number of elements in whole scan rounded (floored) to a natural number

 x_samp = [0:samp_period:samp_period*no_elements]; %Vector of clock signals in cm

 filename = '209.csv';

 Pixel_Value = xlsread(filename,'A1:A65410');

y = Pixel_Value-mean(Pixel_Value); % Getting AC values by subtracting DC signal

plot(y);

title('Interferogram of AC Pixel Values v/s number of points');

xlabel('Number of points'); ylabel('Intensity [arb units]');

 disp('Total number of points in interferogram is: ');

disp(length(y));

disp('Median of interferogram (should be ZPD point) is at: ');

disp((length(y)*0.5));

[M,I] = max(y); % finding ZPD in interferogram

disp('ZPD (point of maximum intensity)in interferogram is found at point number: ');

disp(I); %printing index of ZPD

disp('AC pixel value of ZPD point is: ');

disp(M); % printing AC pixel value at ZPD

 %y = cos(arg*v1) + cos(arg*v2) + cos(arg*v3); % interferogram


 %% FFT operation
```

```
fft_y = fft(y);
n_fft = length(fft_y);
%fft_y(1) = [];
spec_y = abs(fft_y(1:n_fft/2)); % Spectrum generation
nyquist = 1/(samp_period*2); % make samp_period*1 for channel 2
freq = (1:n_fft/2)/(n_fft/2)*nyquist; %frequency scale generation

figure;
plot(freq,spec_y) % plotting spectrum
title('Spectrum of AC Pixel Values v/s wavenumber');
xlabel('Wavenumber (cm-1)'); ylabel('Intensity [arb units]');
tr_freq = transpose(freq);
```

Appendix XVII: List of commercial softwares used

1. Zemax Optic studio, version 16.5
2. MATLAB 2017
3. UML 2.0
4. Draw.io
5. Microsoft Word
6. Microsoft PowerPoint
7. Microsoft Excel
8. Xeneth2.6-Linux-x86_64-2.6.0-1399
9. C++ libraries
10. Adobe Acrobat reader